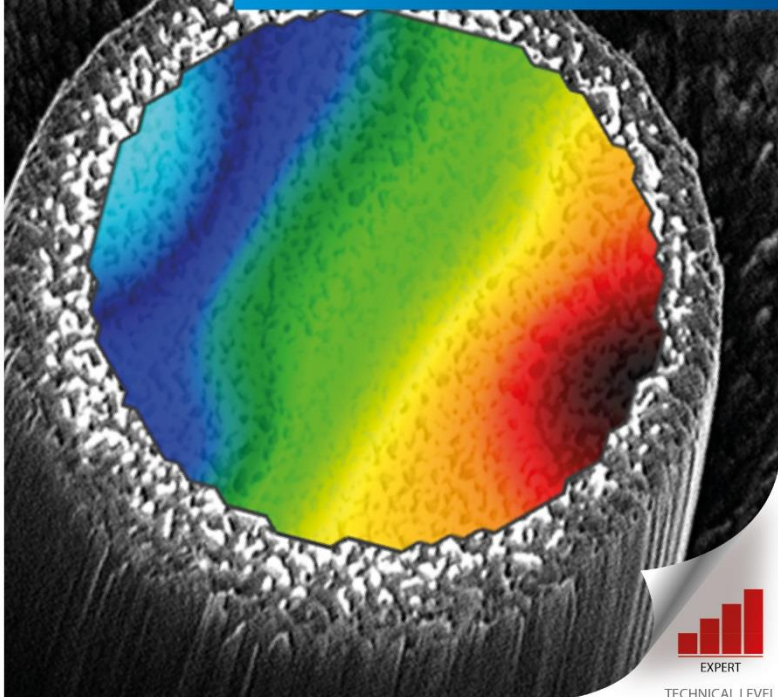




National Physical Laboratory

Good Practice Guide No. 143

A Good Practice Guide for Measuring Residual Stresses using FIB-DIC



EXPERT

TECHNICAL LEVEL



The National Physical Laboratory (NPL)

NPL is the UK's National Measurement Institute, and is a world-leading centre of excellence in developing and applying the most accurate measurement standards, science and technology available.

NPL's mission is to provide the measurement capability that underpins the UK's prosperity and quality of life.

© NPL Management Limited, 2018

Version 1.0

NPL Authors

Jerry Lord (NPL)

David Cox (NPL)

Agnieszka Ratzke (NPL)

Contributors

Marco Sebastiani (Roma Tre University)

Alexander Korsunsky (University of Oxford)

Enrico Salvati (University of Oxford)

Muhammad Zeeshan Mughal (Roma Tre University)

Edoardo Bemporad (Roma Tre University)

Find out more about NPL measurement training at www.npl.co.uk/training or our e-learning Training Programme at www.npl.co.uk/e-learning

National Physical Laboratory
Hampton Road
Teddington
Middlesex
TW11 0LW
United Kingdom

Telephone: +44 (0)20 8977 3222
e-mail: training@npl.co.uk
www.npl.co.uk

Front cover image courtesy of Dr Dietmar Vogel, Fraunhofer ENAS.

Chapter page image courtesy of TESCAN.

Abstract

This focused ion beam-digital image correlation (FIB-DIC) Good Practice Guide (GPG) is one of the key outputs from the iSTRESS project, aimed at providing users with practical advice for making reliable residual stress measurements on their own systems and materials using this technique. It brings together the expertise and experience of the project partners in a single document, and is being used to promote the transfer and uptake of the newly developed methodologies to a wider industry.

Led by NPL and RomaTre and Oxford Universities, it is based largely on input and technical expertise of the project partners involved in Work Packages 2-5, and the results and findings from the various round robin exercises and studies carried out within the project.

The GPG covers all aspects of the measurement process and residual stress analyses for the range of materials and sample geometries examined within the iSTRESS project. It is designed to be a practical guide, with advice, supporting information to illustrate the various process steps, and data analysis required to make reliable and repeatable high resolution residual stress measurements. Examples from the iSTRESS project are included throughout the document to illustrate aspects of the measurement process and highlight good practice.

The GPG is published as a standalone document but is also available on the iSTRESS project website.

It forms an important document for pre-standardisation of the FIB-DIC technique and will continue to be promoted to the Standards community through CEN TC/352 and VAMAS TWA22 and is expected to form the basis of a future International Standard in this field.

Foreword

The aim of this GPG is to provide recommended procedures for measuring residual stresses using the FIB-DIC technique. With this method standard geometries are milled using the focused ion beam (FIB) and the surface displacements resulting from relaxation captured from the scanning electron microscope (SEM) images using digital image correlation (DIC) software; these are then used in combination with finite element (FE) modelling to calculate the residual stresses in the material. The GPG is a key output from the iSTRESS project, and aimed at providing users with a robust methodology and practical advice for making reliable residual stress measurements on their own systems and materials using this technique.

The procedures described in this document have been developed on a wide range of FIB systems and materials. A generic approach has been adopted throughout to ensure that the methodology and recommended good practice is applicable to all commercial FIB systems, and that data can be analysed using different DIC software and the approach is appropriate to a wide range of material systems.

The focus is on measuring residual stresses at the micro-scale, with typical milling geometries and depths of the order 1-10 µm. The approach has been used on a range of metallic coatings and alloys including Au, Pt, Ti, TiW, a nickel-based superalloy (CMSX-6), TiN and Si₃N₄ ceramic coatings, bulk metallic glasses (BMGs) and diamond-like carbon (DLC) coatings, but it is equally applicable to other coatings and bulk materials, both metallic and non-metallic.

The GPG covers all aspects of the measurement process and residual stress analyses for the range of materials and milling geometries examined within the iSTRESS project. It is designed to be a practical guide, with advice, tips and supporting information to illustrate the various process steps and data analysis required to make reliable and repeatable high resolution residual stress measurements using the FIB-DIC approach.

Led by NPL, RomaTre and Oxford Universities, the GPG is based largely on input and technical expertise of the project partners involved in Work Packages 2-5, and the results and findings from the various intercomparison exercises and studies carried out within the project.

It brings together the expertise and experience of the project partners in a single document, and will be used as the principal vehicle to promote the transfer and uptake of the newly developed methodologies within the wider industry context. It also forms the basis of a future International Standard for FIB-DIC residual stress measurement. Individual chapters of the guide cover recommendations for imaging, milling, DIC analysis and interpretation, modelling, data analysis, residual stress calculations, validation and uncertainty. Examples from the iSTRESS project are included throughout the document to illustrate aspects of the measurement process and highlight good practice.

The techniques described assume that the user has some experience in FIB and SEM operation, and access to DIC software for the analysis of the images.

Acknowledgements

This Good Practice Guide has been produced as part of the FP7 iSTRESS project “Pre-standardisation of incremental FIB micro-milling for intrinsic stress evaluation at the sub-micron scale” supported by funding from the European Commission under EU Contract NMP.2013.1.4-2

The editors would like to acknowledge the support and input from all the project partners who have contributed directly to this document, taken part in the various intercomparisons exercises and helped to develop best practice in the technique. The following colleagues in particular are thanked and recognised for their invaluable input.

Dr Ellen Auerswald	Fraunhofer ENAS	Germany
Dr Andre Clausner	Fraunhofer ENAS	Germany
Dr Christian Collet	Thales	France
Dr Diana Court	ETH Zurich	Switzerland
Dr Rostislav Daniel	University of Leoben	Austria
Dr Jiří Dluhoš	Tescan	Czech Republic
Dr Karsten Durst	TU Darmstadt	Germany
Dr Chris Eberl	Fraunhofer IWM	Germany
Dr Mathias Goeken	Erlangen University	Germany
Dr Alexander Lunt	Oxford University	UK
Dr Marco Renzelli	RomaTre University	Italy
Dr Christoph Schmid	TU Darmstadt	Germany
Dr Melanie Senn	Fraunhofer IWM	Germany
Dr Tan Sui	Oxford University	UK
Ms Jeannie Urquhart	NPL	UK
Dr Dietmar Vogel	Fraunhofer ENAS	Germany

Contents

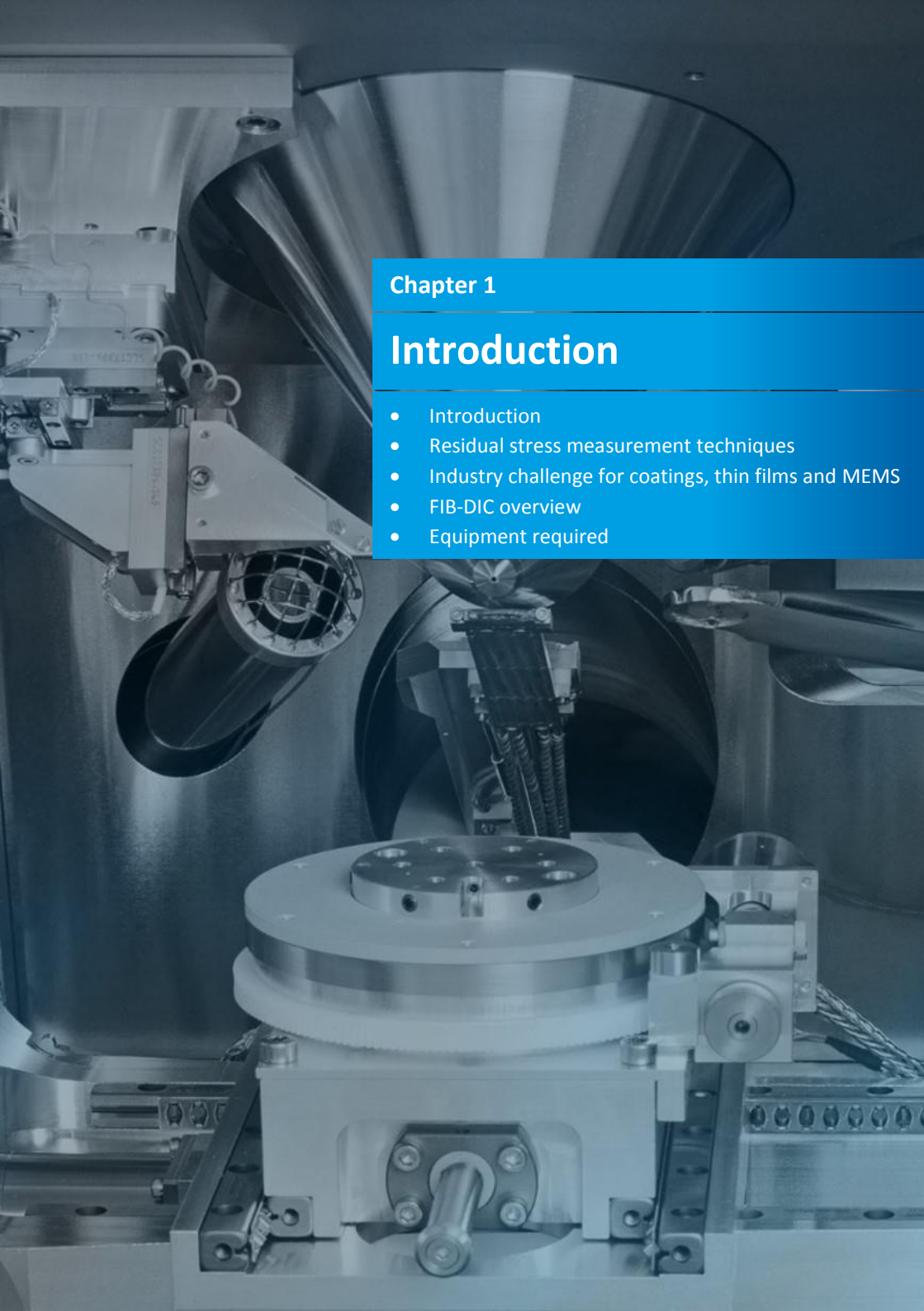
Introduction.....	1
Residual stress measurement techniques	2
Industry challenge for coatings, thin films and microelectromechanical systems.....	3
FIB-DIC overview.....	4
Equipment required.....	7
The SEM	7
The FIB	7
Digital image correlation.....	8
Development of the FIB-DIC approach.....	9
FIB-SEM	13
The FIB-SEM	14
SEM imaging in multi-beam systems	18
Sample positioning and stage movements	20
Setting up the system ready for testing.....	20
Sample issues	23
Sample preparation	24
Requirements on sample properties	25
Surface roughness and texture.....	27
Surface patterning	29
Geometries and dimensions of surface patterns and features.....	31
In-situ FIB-SEM assisted deposition	32
Other surface decoration approaches	33
Milling conditions and issues	37
General milling parameters	38
Establishing the milling rate.....	38
Measuring the milling depth.....	40
Minimising ion beam damage.....	42
Strategies for best depth resolution and deposition reduction.....	45
Recommended FIB milling geometries	49

Surface slots/trenches	50
Ring-core milling	52
Hole drilling.....	53
Selection of the best milling geometry	53
Effect of elastic anisotropy	56
SEM imaging	59
Optimising the image quality for DIC.....	60
SEM imaging artefacts	61
Averaging the images	64
System stability.....	69
Using standard imaging conditions.....	71
Real-time monitoring of image quality	72
Recommended image formats	72
Digital image correlation	73
Introduction and background	74
DIC software packages.....	75
Basic DIC processing steps	76
DIC Analysis Flowchart/Processing Steps.....	77
Calculating displacement and strain	78
Influence of DIC processing parameters.....	81
Effect of DIC window size.....	81
Dealing with rigid body motion and drift.....	83
Using intermediate images as the DIC reference	85
Using the correlation coefficient	85
Strategies for post-processing and cleaning of DIC data	87
Correlation coefficient thresholding	88
Peak position standard deviation thresholding	89
Markers moving relative to neighbours.....	90
Outliers to the expected displacement fields	90
Manual marker removal	91

FE modelling	93
Single slot.....	94
Double slot.....	97
Ring-core.....	100
Data analysis and the calculation of stress	105
Data analysis and the calculation of residual stress	106
Material properties.....	106
Strain relief profiles	108
Residual stress determination from the Double slot/H-bar geometry	112
Four slot milling and the calculation of Poisson's ratio.....	114
Residual stress determination from the Single slot geometry.....	118
Residual stress determination from the Ring-core geometry.....	119
Methods for residual stress depth profiling	120
Regularisation algorithms	122
Tent functions.....	122
Inversion techniques.....	122
Comparison with the piecewise constant technique	123
Alternative milling strategies	124
Validation	125
Reference materials and system checks	126
Tests on standard materials.....	126
TiN coatings	126
In-situ testing	129
Errors and uncertainty	133
Example uncertainty budget.....	137
Reporting of results	141
Links and references	143
Useful websites for FIB manufacturers	144
Useful websites for DIC software and reference images	144
Relevant iSTRESS reports	144

iSTRESS Report Summary.....	144
References	145
Definitions and symbols	153
General procedure for FIB-DIC milling.....	155
Section 1: Basic housekeeping	156
Section 2: Establish milling rate for the material.....	157
Section 3: Does the sample need some surface texture?.....	157
Section 4: FIB milling and image capture	159
An example of creation of dot patterns for stress measurement via Hole drilling	160
Detailed procedure for determining residual stresses from Single slot milling	163
FIB procedures.....	165
DIC analysis	166
Finite element analysis to simulate the stress relief process	166
Stress computation by matching DIC and FEA displacement fields	168

This page was intentionally left blank.



Chapter 1

Introduction

- Introduction
- Residual stress measurement techniques
- Industry challenge for coatings, thin films and MEMS
- FIB-DIC overview
- Equipment required

Introduction

Residual stresses can be defined as those stresses that remain in a body after manufacturing or processing in the absence of external forces or thermal gradients. Virtually all manufacturing and fabricating processes introduce residual stresses into the manufactured article and extreme service loading may also change the state of residual stress in the component. The effects of residual stress may be either beneficial or detrimental, depending upon the sign, magnitude and distribution of the stress, all of which can be critical to performance and have to be considered in the design of a component.

Residual stresses can act over a range of length scales, and a wide range of techniques are available for measuring them. They can be defined as either macro or micro stresses and both may be present in a component at any one time. Macro residual stresses, which are often referred to as *Type I*, vary within the body of the component and act over a range much greater than the grain size. Micro residual stresses, which result from differences in the microstructure, phases or layers in a material or coating can be classified as *Type II* or *III*. They can change sign or magnitude over distances comparable to the grain size. *Type II* residual stresses are micro residual stresses that operate at grain size; *Type III* are generated at the atomic level [1, 2].

Of particular interest in the current work and the focus of this Good Practice Guide (GPG) are residual stresses that act on the micro- and nanoscale and are important to the performance of coatings, thin films and electronic devices – the so-called *Type II* residual stresses defined above. These are important as residual stresses at the nanoscale can cause damage and crack initiation on the local scale, leading to the failure of the whole coating system or device.

Residual stress measurement techniques

The measurement of residual stresses in thin coatings is a particularly difficult challenge, and although a large number of different residual stress methods are available most are not relevant to this particular application. A number of general papers and handbooks have been published in this field [1-4] to aid technique selection, including a series of NPL Good Practice Guides on Residual Stress Measurement [5-7] of which this is the latest addition. The residual stress techniques can be grouped according to different criteria based, for instance, on their physical characteristics – sampling volume, penetration depth, resolution, uncertainty and the stress state they can measure; practical issues – contact versus non-contact, destructive or non-invasive, lab-based, cost and the availability of the equipment and whether they can only be used on certain material types.

For the class of residual stress techniques involving material removal or machining, the methods involve controlled material removal and the subsequent measurement of surface strain relief. When new free surfaces are created within the sample, a redistribution and re-

equilibration of strains and stresses follows. If this strain relief can be measured with suitable accuracy, then the pre-existing residual stress state can be deduced with the help of Hooke's law. This is the general approach used by the conventional macroscopic Hole drilling, Ring-core, slitting and contour methods, and the focused ion beam-digital image correlation (FIB-DIC) procedures covered in this work are essentially downscaling of the principle to the micrometre or nanometre scale, using the focused ion beam (FIB) to remove material and digital image correlation (DIC) to measure the strain relief. The approach has already been established as a method for achieving sub-micron spatial resolution for the residual stress analysis in amorphous materials and thin nanostructured layers, and a large volume of work has been produced to demonstrate its application.

Industry challenge for coatings, thin films and microelectromechanical systems

Residual stresses usually arise from the processing of the materials, caused by, for example, intrinsic growth stresses in thin films or due to combinations of materials with different thermoelastic properties operating under thermal loading. In coatings, thin films, microelectromechanical systems (MEMS) and electronic devices, residual stresses act on the nanoscale but can cause damage and crack initiation on the local scale, their presence leading to the failure of the whole coating system or device.

Despite urgent industry requirements, the assessment of the residual stress in sub-micron volumes is still an extremely challenging task, especially in the case of nano-crystalline, strongly textured, complex multiphase or amorphous materials and thin films.

If it is possible to understand and control the residual stresses developing in these systems, it is possible to increase performance and reliability. The FIB-DIC technique described in this document addresses the needs of many different industrial sectors, including information science and technology (particularly microelectronics and sensors), where thin films are the integral components of the devices, or the automotive sector, where wear and friction are crucial for resource effective transportation systems. An example of an industrial application where the management of micrometre-scale residual stress has played a critical role is in the diesel injection system, where the development of reliable, thin carbon coatings has been crucial, leading to ever increasing high pressures and the resulting fuel efficiencies that would not otherwise be possible.

Other examples can be found in the power industry (bearings for wind generators, Thermal Barrier Coatings, Plasma facing materials), cutting tool industry (wear resistance layers), optics industry and medical sectors (coatings for implant materials). In fact, the reliable measurement of residual stress is a critical issue for the robust design and reliability assessment of a wide range of micro- and nano-systems, as they directly affect:

- The adhesion and fracture toughness of thin films
- The load bearing capacity, elastic properties and ductility of Bulk Metallic Glasses (BMGs)
- The reliability of micro-welds and other metal interconnects, crack propagation and charge carrier mobility in semiconductor Back-end-of-line (BEO-L) systems with ultra-low-k (ULK) nano-porous films
- Thermal stresses in through-silicon vias (TSV)
- The resonant frequency and lifetime of micro/nanoelectromechanical systems (MEMS/NEMS).

The high-resolution methodology that has been developed in the iSTRESS project is based on the combination of incremental FIB micro-milling, with high-resolution in-situ scanning electron microscope (SEM) imaging and full field strain analysis by DIC. The use of analytical and/or numerical models is finally required for residual stress calculation.

A key challenge in developing the FIB-DIC technique was to make the measurements more affordable and accessible to industry and small and medium-sized enterprises. This has been achieved largely through process optimisation and automation of the main FIB-DIC milling and imaging steps to reduce both the time and cost required to make the measurements.

FIB-DIC overview

As noted previously, the FIB-DIC technique can be used to overcome the limitations of the conventional X-ray diffraction (XRD)-based approaches through a combination of FIB milling, SEM imaging, analysis of the surface displacements by DIC, and finite element (FE) modelling to calculate and resolve the residual stresses present [8-33]. In the measurement (Figure 1) the FIB micro-milling induces controlled strain relief at the surface of residually stressed samples. The strain relaxation is then measured at sample surface via DIC analysis of SEM micrographs of a reference surface, and residual stresses then calculated from the relevant analytical and numerical models.

The so-called **FIB-DIC** approach allows for stress measurements to be made in most materials with submicron spatial resolution, generating essential input data for complex FE studies, and making virtual product prototyping more cost effective and practical.

Within the iSTRESS project, it has been possible to develop an accessible, reliable and accurate micro-scale FIB-DIC residual stress methodology, which not only can be applied in research studies to support the development of new materials, processes and systems, but can also be used as a routine tool in industry, particularly within production and quality control.

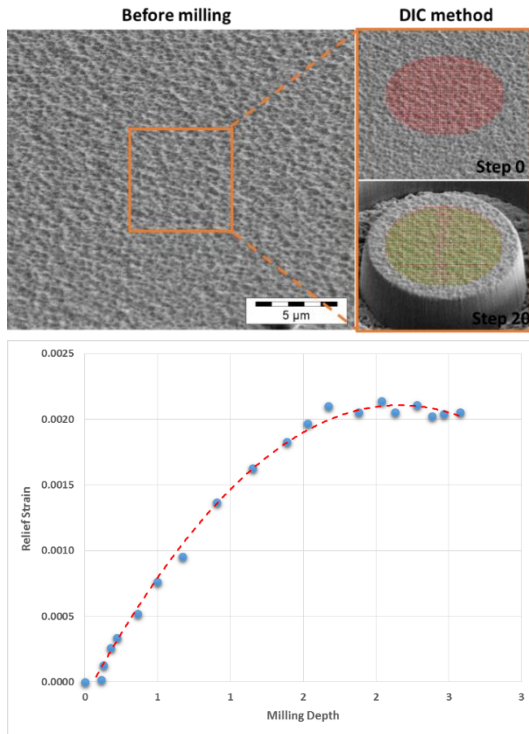


Figure 1. Example of an FIB-DIC procedure for local strain relaxation measurements (Ring-core geometry).

The principles of the FIB-DIC approach for measuring residual stress are given in the schematic in Figure 2 below. There are four main steps to be followed, associated respectively with patterning and imaging, milling, the DIC analysis and finally modelling to convert the surface displacements and strains to residual stress.

Individual chapters within this guide deal with the initial preparatory work to understand the performance and capability of the FIB-SEM system, giving advice on sample preparation and patterning, optimising image quality, together with examples and recommendations for checking the stability, quality, accuracy and repeatability of the measurements, including the use of physical reference samples, in-situ tests and reference image sets that are available for assessing the accuracy of the DIC software.

The section on milling covers recommended geometries and some data on FIB-induced damage and artefacts that users should be aware of. A generic milling protocol is given in Appendix 1 which has been developed to semi-automate the milling and image capture process. This is important for removing operator influence and improving repeatability, and also offering the possibility of using the FIB system outside normal operating hours with

minimal supervision and input – an attractive commercial option for both maximising the use of the equipment and reducing costs.

The sections on DIC analysis include recommendations and examples on the effect of different DIC parameters, how displacements and strains are derived and advice on the processing of the images and data to improve the reliability and accuracy of the measurements.

Finally details of the modelling and data analysis required for converting the relieved strains to residual stresses are included, together with information on uncertainties and the various tests that can be used to validate the measurement set up and results.

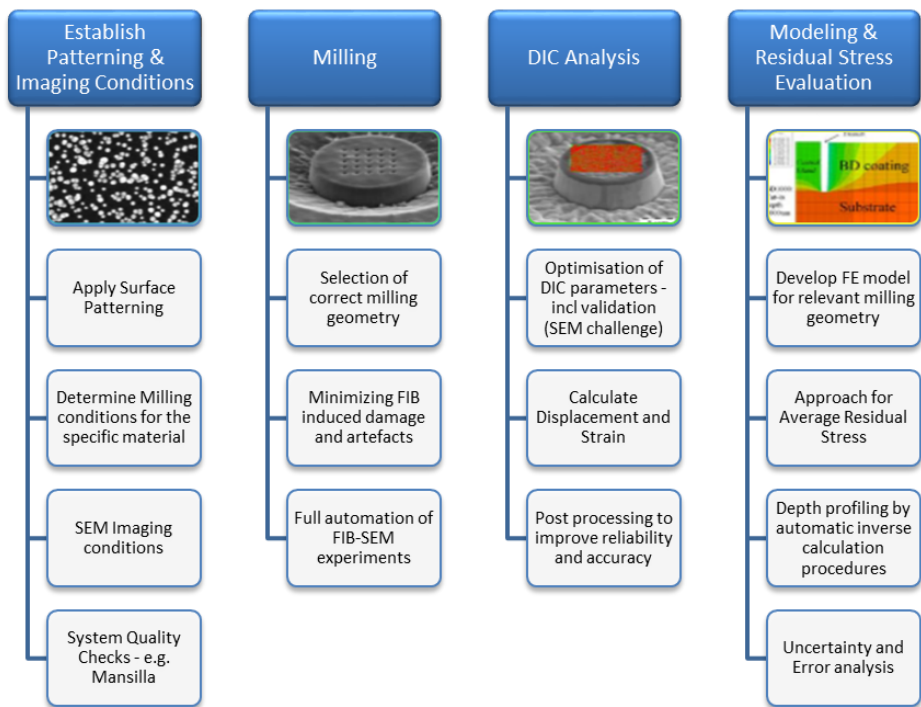


Figure 2. Main experimental and calculation steps for measuring residual stresses with the FIB-DIC approach.

Equipment required

A brief summary of the key equipment needed for the measurements is given below; more detailed information and recommendations to optimise the equipment and different stages in the FIB-DIC approach are covered in more detail in later chapters.

The SEM

In an SEM, a beam of electrons is generated by a source (typically a tungsten filament) and is accelerated through a high voltage (e.g. 30 kV). A combination of electromagnetic lenses and apertures produces a very thin beam which scans the surface of the sample with the help of a scanning coil. Reflected electrons by this scanning action are collected by a suitably positioned detector whose output modulates the brightness of the spot on the screen. Generally bright areas represent the peaks while dark areas represent the valleys.

Based on the interaction of electron beam with the sample surface, two kinds of imaging are possible: secondary electron (SE) imaging, which gives high resolution and is surface sensitive, and back scattered electron (BSE) imaging, which provides low resolution but a higher compositional contrast. The specific use of the SEM within the iSTRESS project is mainly during the FIB-DIC procedure using SE images and will be explained in the following sections.

The FIB

A FIB system looks and operates very much the same as the SEM, but the main difference is that gallium ions (Ga^+) are used as an alternative to electrons. The FIB gun is a liquid metal ion source (LMIS) positioned in contact with a sharp tungsten (W) needle. The liquid streams on the exterior surface and reaches the needle tip facing the extraction terminal. High extraction fields ($> 10^8 \text{ V/cm}$) pull the liquid Ga into a sharp cone with a typical radius around 5-10 nm. Ions are emitted as a result of field ionisation and are accelerated down the ion column. There are two advantages of using Ga as an ion source: it has a low melting point so it remains in liquid state at room temperature, and Ga can also be focused to very small spot size ($< 10 \text{ nm}$ in diameter).

More specific information about the FIB and how the setup and operation can be optimised for the FIB-DIC process is included in Chapter 3. Just like the SEM, the intensity of the secondary electrons produced at each raster position of the beam is displayed to create an image of the sample. Since ions are heavier than electrons and can strike with greater energy, they result in the sputtering of neutral and ionised substrate atoms, and milling of the sample. During this process, chemical interaction also occurs, like breaking of chemical bonds, dissociation of molecules and hence this phenomenon can be exploited during the deposition process.

Most of the main commercial SEM manufacturers also produce FIB-SEM systems. Within the iSTRESS project a wide range of different FIB-SEM systems were used including models supplied by TESCAN, Zeiss, FEI and Jeol. The techniques and good practice that have been developed are not machine specific and can generally be applied to any FIB-SEM system. Links to some of the manufacturer's websites are given at the end of this guide.

Digital image correlation

For DIC, displacements are determined from a set of images of an object surface taken before and after deformation using a digital camera. The images are then compared to detect displacements by searching a matched point from one image to another. Since it is almost impossible to find the matched point using a single pixel, an area with multiple pixel point (such as 20×20 pixels) is used to perform the matching process. These so-called subsets, or windows, have a unique light intensity (grey level) distribution which can be tracked during deformation to produce a full-field displacement map from which the strain fields can be calculated. For DIC to work well the images must be good quality, free of noise, and have a range of contrast and brightness. It is assumed and indeed required that the images remain stable and do not degrade significantly during the test and this is a challenge for some of the FIB-SEM systems as will be discussed later.

Figure 3 shows the basic principle of DIC using images at different stages of deformation. The displacement of the subset in the image before deformation is found in the image after deformation by searching the area of same light intensity distribution with the subset. Once the location of this subset in the deformed image is found, the displacement of this subset can be determined to sub-pixel accuracy, using various correlation criteria and data fitting techniques. To accurately perform this process, the surface of the object must have a feature that allows matching the subset. If no feature is observed on the surface of the object, an artificial random pattern must be applied. More information on patterning, imaging and DIC processing is given in later chapters.

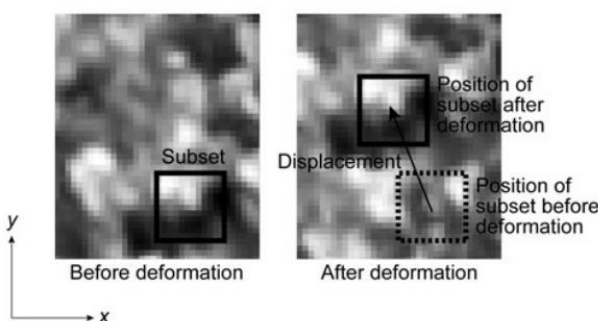
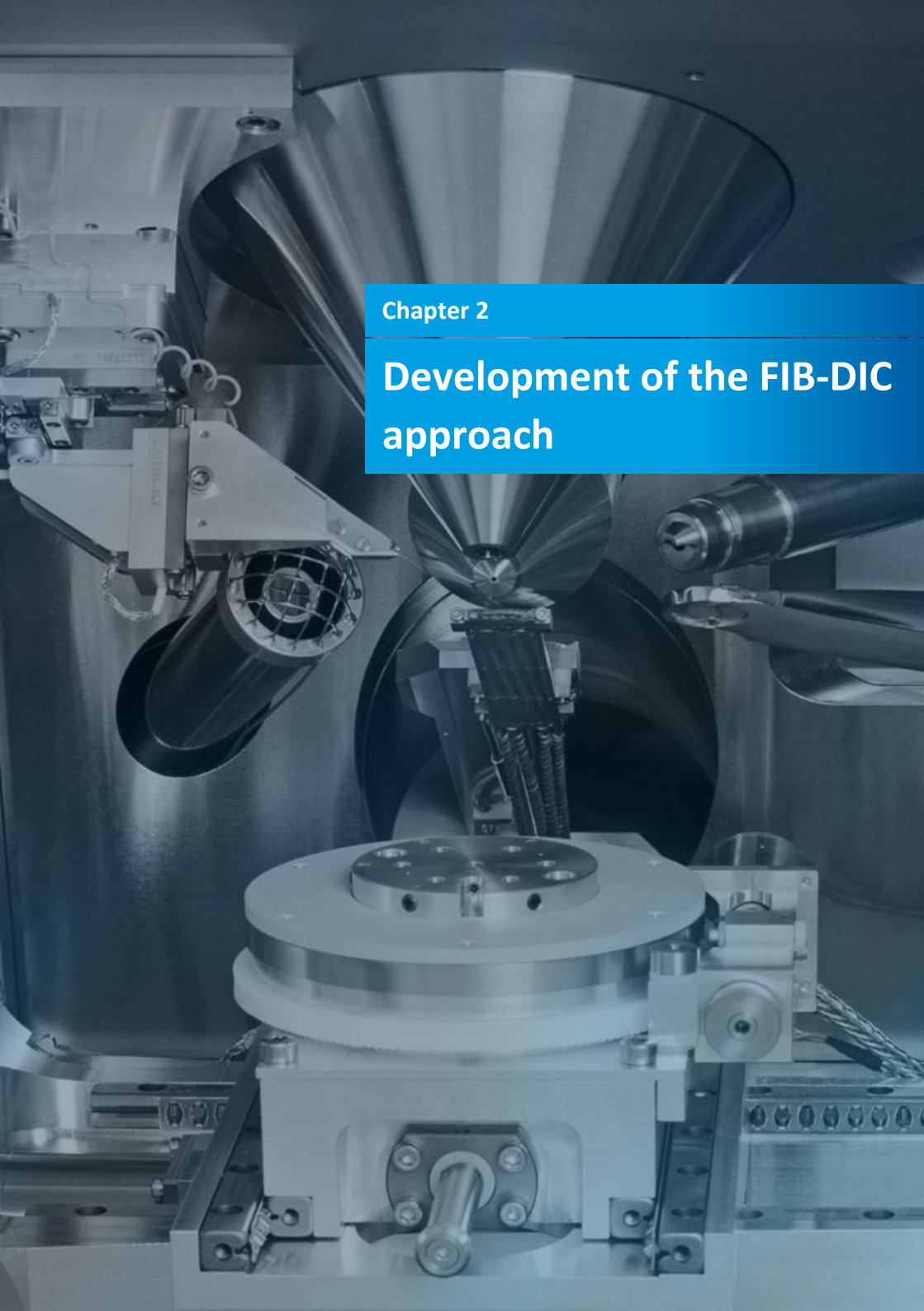


Figure 3. Basic principle of digital image correlation [34].



Chapter 2

Development of the FIB-DIC approach

Development of the FIB-DIC approach

Analysis of the literature shows a growing interest of the scientific community in the development of the FIB-DIC procedures for measuring residual stresses on the micro-scale, as demonstrated by the increasing number of papers that are being published, many of which are from scientific partners involved in the iSTRESS project.

Early developments by Kang et al. [8] successfully proposed the downscaling of the slitting method using the FIB to measure the stress release caused by the milling of a slot on a thin diamond-like-carbon (DLC) film deposited on a glass substrate, example shown in Figure 4a. Sabate et al. [9] also used the FIB tool to machine straight shallow or deep trenches within the sample surface. Analytical solutions for the displacement fields around a crack taken from linear elastic fracture mechanics were used to estimate the residual stress component in the direction perpendicular to the trench extension. For the Hole drilling geometry, some work already exists in the literature for the downscaling of the technique using FIB milling/SEM Image on amorphous materials [25] to evaluate the through-thickness stress gradients. One of the main drawbacks of the FIB-DIC procedures is the additional damage and stress that may be induced by the FIB milling process at the edges of the milled volume; in the case of the slot and Hole drilling geometries, the areas where maximum deformation is expected (close to the edge) are often damaged by the ion gun and cannot be used for stress calculation, with a significant loss of resolution and accuracy.

One group of investigators, including the iSTRESS project coordinators, [11] recently proposed and validated an incremental micro-scale Ring-core method, μ RCM, Figure 4b, based on removal of material by FIB milling on a sub-micron scale. The Ring-core geometry was shown to be very effective in providing complete and substantially uniform surface strain relief over significant areas, and was successfully applied to measure the average stresses in thin coatings and double-clamped suspended membranes [21].

The principle of Ring-core milling was also recently applied for residual stress depth profiling in thin hard coatings and residual stress local analysis in amorphous single-splats obtained by thermal spraying [24]. Recent papers also introduced new optimised milling geometries that maybe extremely interesting for the effective transfer to industry of such methods.

In particular, Sebastiani et al. [28] recently proposed the use of the Double-slot method as an alternative way to analyse residual stress states along a specific direction, example shown in Figure 4c. It demonstrated that the Double slot can give a full uniaxial stress relief, thus giving higher relaxation strains in comparison with the Ring-core (which gives a full biaxial stress relief). This latter aspect may be useful to the strain analysis in samples with low residual stress state. In addition, if two additional perpendicular slots are milled to form a central squared area (Four slot method), the same work demonstrated that a direct measurement of the surface Poisson's ratio can be achieved by the comparison of the relaxation strains that are

measured in the two situations. Durst et al. [33] also introduced a new geometry which simply consists of the combination of two parallel regular FIB cross sections (H-bar geometry), a simple configuration that may be extremely useful in view of the automation and transfer to industry of the method, example shown in Figure 4d.

The unique possibility of obtaining different characteristic stress reliefs by varying the trench geometry is therefore an extremely versatile tool for investigating non-uniform stress residual stress distributions, including stress analysis associated with defects. The investigation of scale effects can also be achieved by varying the characteristic size and shape of the milled trench; a powerful and versatile approach that is not readily achieved by other available techniques.

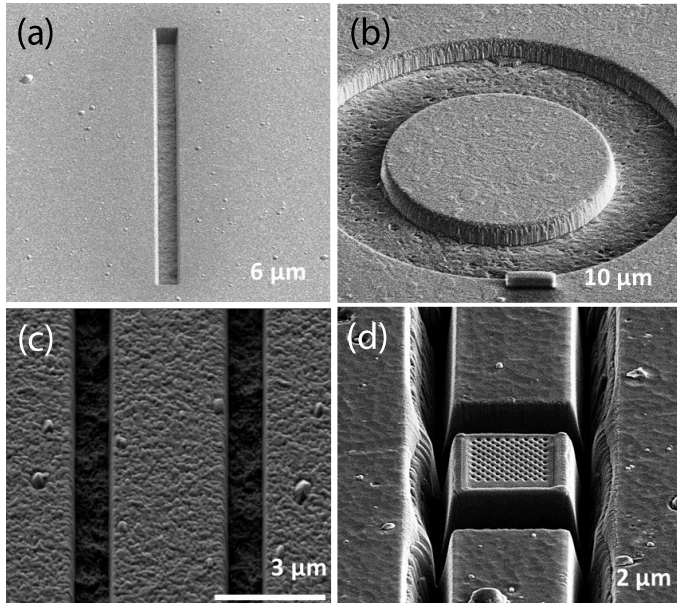
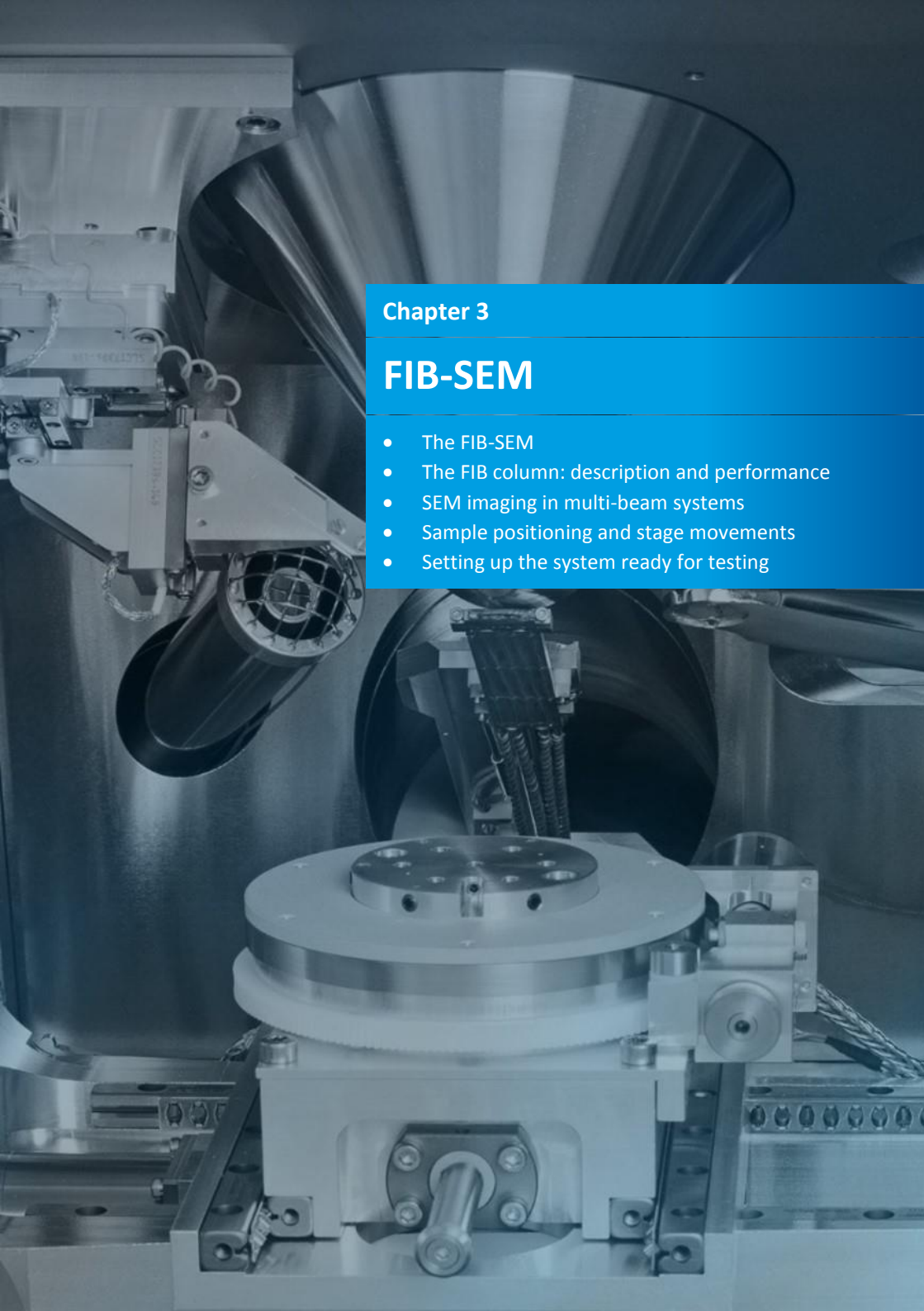


Figure 4. Examples of FIB-DIC geometries.

In addition, the FIB-DIC methods also allows for the measurement of non-uniform and non-equi-biaxial residual stress states, including stress depth profiling. In this latter case, critical issues identified were: (i) the selection of the proper geometrical parameters for optimal depth resolution; (ii) the realisation of accurate experiments allowing for nanometre resolution in strain profiling; and (iii) the implementation of inverse calculation procedures (with regularisation algorithms to reduce noise in stress calculation at the highest depths [25, 26]), to achieve sub-micron resolution of stress profiling.

Recent papers [19, 25, 26] clearly show that the achieved depth resolution for depth profiling by the use of such techniques is of the order of 200 nm. The same papers foresee as a feasible

target a final value of depth resolution is of the order of 50 nm. In case of the Ring-core geometry, recent work also showed that a lateral spatial resolution of the order of 400 nm can be achieved using the currently available FIB sources.



Chapter 3

FIB-SEM

- The FIB-SEM
- The FIB column: description and performance
- SEM imaging in multi-beam systems
- Sample positioning and stage movements
- Setting up the system ready for testing

The FIB-SEM

FIB instruments have become almost standard equipment in device manufacturers over the last twenty years and are becoming increasingly common tools in materials science laboratories. Primarily used to study defect analysis in the former and microstructure in the latter their use has grown to the point where these techniques are beginning to be considered routine.

The basic principle behind these instruments is that a focused beam of high energy high ions is used to physically remove atoms from the sample surface, making it possible to investigate the internal structure of the sample by physically cutting into them in very precise manner in a process known as sputtering (or ion milling). As an example of their use, one of the most common procedures carried out with a FIB is known as cross-sectioning, where a block of material is removed by the beam so that the newly exposed faces of the walls of the hole left behind can be imaged to study the sub-surface structure of the sample. Another common use of FIB is the production of thin lamella samples from precisely targeted regions of a sample that can subsequently be analysed in transmission electron microscopes. More sophisticated semi-automated procedures are also available such as continuing to remove thin slices of material from an exposed face and imaging each new face in turn, with the images being reconstructed with the assistance of dedicated tomography software, enabling creation of a three-dimensional representation of the internal structure of the volume of material. These are just a few of the many procedures and techniques that can be applied in a FIB system [35].

FIB instruments naturally have their limitations, the most significant of which are limits to the volume of material that can be sputtered in a reasonable time. This limit is imposed by the very modest ion beam currents available on these instruments and so their use is usually restricted to investigating areas on the micrometre scale. Recent developments with plasma-based ion sources are however now making instruments available with higher beam currents enabling significantly higher speeds or increases in volumes up to fifty times greater.

Initially FIB systems were single column instruments using ions for both generating images and for carrying out sample sputtering, but very quickly more sophisticated versions emerged that also had SEM columns that could offer the non-destructive imaging unobtainable with ions. While some of these single column instruments are still in service the vast majority of FIB systems in operation worldwide today are two-column (combined FIB and SEM) instruments. An example a current state of the art FIB is shown in Figure 5.

In addition to the two columns modern FIB instruments will have a five-axis sample stage (x , y , z , tilt and rotate) with at least 50 mm sample capacity and up to 300 mm on larger instruments. A number of detectors will be fitted as standard and will as a minimum comprise an SE detector for image generation from both electron and ion columns – both electron and ion beams will liberate secondary electrons that can be used for image generation. In addition,

it is not uncommon for there to also be a BSE detector, a secondary ion (SI) detector and possibly other electron beam derived techniques such as X-ray detectors (energy-dispersive X-ray spectroscopy (EDS), wavelength-dispersive X-ray spectroscopy (WDS)) and electron backscatter diffraction (EBSD) cameras.



Figure 5. A modern FIB system (courtesy of TESCAN).

The secondary electron detector is the primary choice for the methods described in this guide due it offering the highest imaging resolution and being present on all instruments. All the detectors and the sample stage will be contained in a high vacuum system with a typical base pressure around 1×10^{-7} mbar under normal operating conditions with a series of valves connected to the columns to allow the passage of electrons or ions into the sample chamber. A simplified layout of a typical system is shown schematically in Figure 6 below.

In normal operation the sample is mounted flat on the sample stage (usually on a standard SEM pin-stub). The stage is then tilted so that the sample surface is orthogonal to the ion beam, but with the region of interest aligned with both electron and ion beam at the beam coincident point, allowing imaging of the same region with either column without further moving the sample. In the vast majority of systems the electron column being the more massive is mounted in the vertical position and, due to the requirement for coincident beams and the geometry of the two columns, the ion column is offset at an angle to the side of the electron column. In normal operation this arrangement results in the requirement to tilt the sample to between 50 and 55° (dependent on specific manufacturer) to present the sample at normal incidence to the ion beam. In this configuration the SEM column can then image both

the surface and the side wall of the sample (and therefore depth) of any hole the ion beam mills.

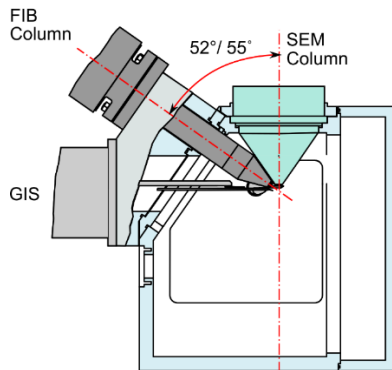


Figure 6. Simplified schematic diagram of typical FIB configuration.

The FIB column: description and performance

Although several manufacturers of FIB instruments exist, the principle of operation of the ion column is the same in all cases. Ionised atoms, usually of Ga, although xenon (Xe) based systems are now becoming available, are emitted from a source in the top of the column and are accelerated in a high electric field to a velocity of almost $250\,000\text{ ms}^{-1}$. This beam of ions is then passed through an electrostatic optical system of lenses, apertures and scan-coils to produce a fine focused beam that is scanned over the chosen sample. Beam current in a Ga-based system will typically range from a 1 pA to a few tens of nA maximum with a higher maximum available in Xe based system of up to 2 μA and accelerating voltages in all types of instrument range from 2 kV to 30 kV.

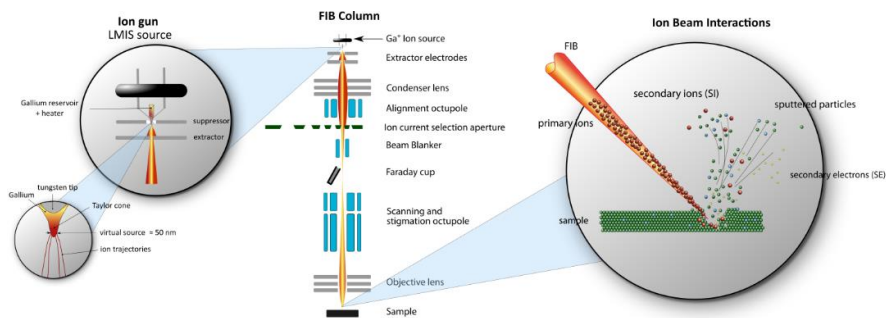


Figure 7. Schematic diagram of FIB column and ion beam interactions.

In normal imaging or simple sputtering operations the ion beam is scanned from point to point as depicted in Figure 8. The beam is focused into a circular spot of a given diameter (dashed circle) that is proportional to the chosen beam current, which in turn is chosen based on the volume needed to be sputtered. The beam will dwell at this fixed point for a predetermined time (ranging from ns to ms) before it steps along a line by a fixed amount (denoted 'x' in Figure 8). The step size the beam takes is in the range of nm at low beam currents and maybe several orders of magnitude larger than this at the highest beam currents and hence largest spot sizes. Each step is usually set so that the beam spots overlap by up to 50 % of the spot diameter from step to step (denoted 'o' in Figure 8) ensuring that the area to be milled is uniformly exposed to the ion beam. Once the beam has reached the end of a line it is blanked electrostatically and then swept back to begin a new line with line spacing (denoted 'y' in Figure 8) and beam spot overlap is usually the same as the point-to-point step size. Once the area to be milled is fully exposed the beam is usually blanked again and then swept back to repeat the same area and this process is repeated many times (typically $> 10^3$ to 10^6) to ensure uniform ion milling to the correct depth.

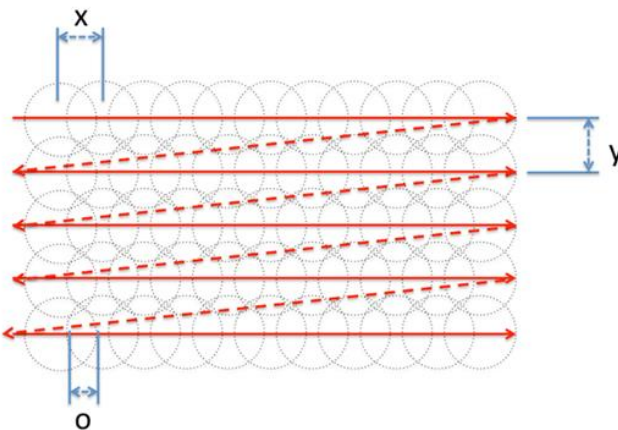


Figure 8. Schematic diagram indicating a typical beam scan methodology [35].

As the high-energy ions impact on the sample surface their energy is given up to it in a series of inelastic scattering events with the sample atoms, which in turn results in some of these atoms at the sample surface being ejected. In low-density materials, the ions can travel significantly deeper into the sample resulting in their energy being exchanged deeper in the sample than in high-density materials. The depth the ion travels has a direct influence on the sputter yield and there is a broad correlation of higher density substrates having higher sputter yield (more atoms ejected per incident ion) as the ion gives up its energy closer to the sample surface. As an example for a 30 kV Ga ion impacting the sample at normal incidence the sputter yield for a silicon sample would be approximately 2.5 atoms per ion, on average,

whereas for a gold sample the sputter yield is over 20 atoms per ion. For all substrates at normal incidence, which is usual, the probability of ion recoil from the surface is very close to zero and the ion will embed itself in the region near the sample surface resulting in significant ion implantation in the near-surface region that can result in changes to the sputter yield and local alloying in rare cases.

Owing to the maximum available beam current in the FIB, the volume of material that can be removed from a sample in a reasonable time is very modest. Typically in an instrument with a Ga ion source the user will be limited to a volume of few thousand μm^3 , depending on the sputter yield of the material in question and how long the user is prepared to wait. In Xe-based systems with their much higher beam current, the maximum volume can be increased by approximately a factor of 50. For imaging internal microstructures of many materials and establishing residual stress via milling these volumes are quite adequate.

SEM imaging in multi-beam systems

In the majority of modern FIB systems imaging of the sample is carried out by an electron column. While the high-energy ions from the FIB column generate secondary electrons and are quite usable for imaging, the ions themselves cause sputtering of all the regions the beam is scanned over, thereby modifying the sample as it is imaged. In particular, when using FIB for residual stress determination it is the changes present in a series of images that are used to determine the stress and any additional modification by the beam while imaging is likely to cause error in this method.

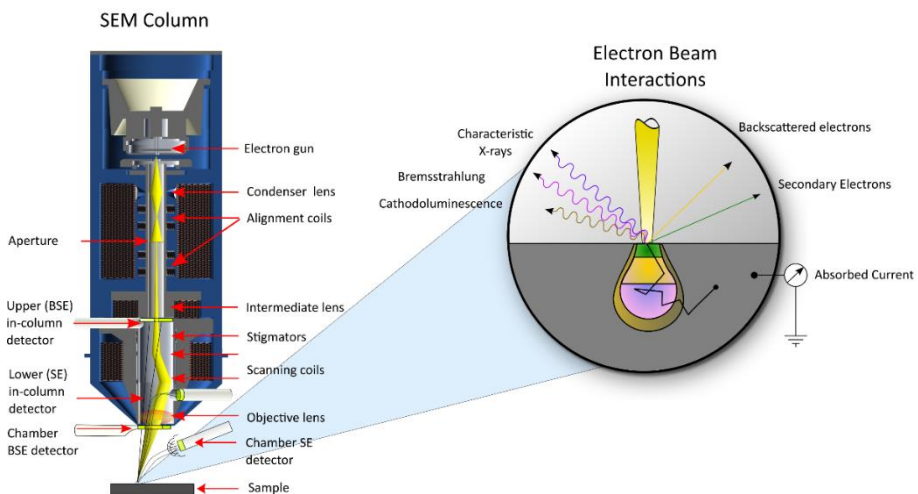


Figure 9. Schematic diagram of a modern SEM column.

Turning to the SEM column, these are exactly the same type of columns as found in modern SEM systems, along with the usual collection of available detectors. For the vast majority of imaging, and the method of choice for residual stress determination, secondary electron imaging is available on all electron column based systems. Offering high resolution and greatest sensitivity to surface detail, secondary electron detectors can be found both chamber mounted, of the Everhart-Thornley type, and/or additionally located in the final lens of the electron column itself, which offers the highest resolution.

During ion milling the sample is tilted so that the surface to be milled is perpendicular to the ion beam and the region of interest is visible to both beams without further movement – the coincident point. Owing to the geometry of the electron and ion columns this means that the SEM views the sample from an angle of around 35 to 40° (depending on the specific instrument) (Figure 10). This geometry allows the electron beam to view the inside of the ion-milled hole as it progresses verifying the depth of the hole (providing it is not too deep to image to the bottom).

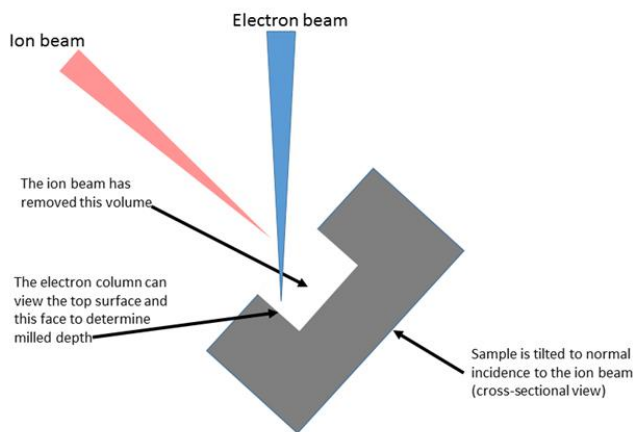


Figure 10. Schematic diagram of the geometry of the beam paths and sample in a typical FIB system.

SEM imaging with the sample tilted of course implies that the sample will appear distorted when imaged, i.e. if the scan is still the same size and shape as if the sample were imaged perpendicular to the beam, with the sample tilted the scan is effectively elongated. This effect is easily corrected however, and all FIB systems can compensate with 'tilt correction' that effectively compresses the observable image back down to the correct aspect ratio. However, it should be remembered that if the image of the surface has been corrected then any measurement of depth will now be in error as its angle to the beam is different to the sample

surface. Again this is something that is easily correctable in the systems software and reliable measurements of depth can be made.

Sample positioning and stage movements

All modern FIB systems will have sample stages with five degrees of freedom, the orthogonal x , y and z axes, along with one tilt and one rotation. This stage will be computer controlled from software and/or a joystick. The range of the x and y orthogonal axes on the vast majority of systems is largely dependent on the size of the vacuum chamber and is usually either ± 25 mm, ± 50 mm, or ± 75 mm with a z range usually around half the x and y range. The range of the stage and chamber size also naturally dictates the maximum size of sample that can be accommodated, but for the vast majority of samples even the smaller stages are more than adequate in this respect. The rotational axis on all systems is 360° of continuous rotation and the tilt will usually be of the order -10° to 70° with the positive direction of tilt pointing the sample towards the optical axis of the ion beam.

Setting up the system ready for testing

Although a key objective of the iSTRESS project was to develop a fully automated approach for carrying out the FIB-DIC procedure there will always be a requirement for some user involvement, particularly in initially setting up the system ready for testing. Only once this has been established it may then be possible to carry out the milling and imaging steps using an automated script without user involvement.

For the FIB-DIC procedure to give the best possible results the instrument should be in good working order and fully calibrated. Of particular importance is the correct alignment and calibration of both the electron and ion columns. Any aberrations in the electromagnetic/electrostatic optical systems of either column can result in poor imaging or poor definition of the milled areas resulting in poor performance of the method. Depending on specific manufacturer the terminology and the method used for the alignment procedure can vary, but at its most basic usually consists of source alignment and tilt correction and alignment of apertures. Some of these procedures can be fully or semi-automatic and it is assumed the user is fully aware of these procedures and able to apply them correctly.

Prior to carrying out the procedure it may be necessary to heat the gas injection system (GIS) if it is to be used for to provide patterning of the substrate. While these systems typically heat and are indicated as ready for use in a few minutes, best performance is often obtained if the system has been heated for at least an hour prior to use. It should be noted on some systems they will turn off the GIS heating on sample loading particularly if the chamber has to be fully vented, rather than using a load-lock rapid entry. If this occurs the GIS heating needs to be re-enabled but the user should not need to wait beyond the ready to use indication if the system has only been in the off-state for a few minutes.



Tip – It is recommended that the system be turned on and left for at least 1 hour before measurements are made to ensure machine and image stability.

With the sample loaded, the chamber vacuum ready and both column sources on it is now possible to move near to the region of interest on the sample. Set the sample at the correct height in the chamber (depending on manufacturer this may be termed eucentric height or coincident point). If any surface decoration is required the pattern should be loaded and the GIS inserted.

Once surface decoration, if required, is carried out the sample should be tilted so that its surface is orthogonal to the ion beam. Final checks should be made to focus and astigmatism and contrast and brightness of both columns at the approximate field of view to be used. If already created, the milled geometry pattern should then be loaded or if not created and positioned on the FIB imaging window in the correct location.

Users should refer to the operation procedures for their own equipment for specific parts of this method, but may also find the description of a generic procedure developed by iSTRESS partners included in Appendix 1 useful for reference.

This page was intentionally left blank.



Chapter 4

Sample issues

- Sample issues
- Sample preparation
- Requirements on sample properties
- Surface roughness and texture

Sample issues

As a general rule, a user who is familiar with SEM good practice and operation should find that these skills are directly transferable to FIB. Basic standard SEM practice such as use of gloves and tweezers to minimise both sample and instrument contamination should be carried out. If at all possible, samples should be mounted on standard sample mounts such as the correct pin stubs for the instrument, along with SEM-approved conductive adhesive pads and/or properly dried and degassed silver or carbon adhesive paints. Correct use of these practices should be employed to maintain the optimum performance of the instrument.

Sample preparation

The sample to be analysed should be clean, dry and free from dust and loose material. In particular, any substance that may be on or in the sample that may outgas in the instrument chamber leading to vacuum degradation and/or contamination problems in the instrument is to be avoided.

Some samples may require polishing in accordance with the usual polishing methodology for that particular sample, e.g. standard metallographic polishing or electro polishing methods. However, it should be remembered that this may not be a suitable method in many cases. For example, polishing may significantly change the stress state of the material in the region to be studied by removing the surface layer. Often the final stage polish with colloidal silica can lightly etch the material which might be of some benefit and give the possibility of carrying out DIC without any additional patterning.

The majority of the samples likely to be studied will be capable of least a minimal clean such as a rinse with a solvent such as isopropanol or a few minutes in an ultrasonic cleaner in solvent and in both cases blowing dry with clean dry air or nitrogen. In some cases a full triple clean in the ultrasonic cleaner with acetone, isopropanol and finally deionised water may be needed. In general acetone should be avoided except in the triple clean process. In particular the FIB residual stress measurement method requires the region of the surface to be studied to be clean enough to be imaged repeatedly without surface contamination build up due to the electron beam polymerising carbon based surface contaminants.

In cases where the sample is showing these effects strongly and significant differences appear between subsequent images it may be necessary to expose the sample to an oxygen plasma to remove the contaminants to enable acceptable repeated imaging. In extremely rare cases it may not be possible to obtain high enough quality data as the sample may not be suitable for the vacuum requirements of the instrument or may be affected by the electron beam – certain polymers are particularly problematic. Further, the chemistry of the sample may not be suitable for cleaning by chemical or plasma methods.



Tip – It is increasingly common to find plasma cleaners installed on FIB systems. If this option exists on the instrument it is there expressly to assist with the problem of beam induced surface contamination and its use should be encouraged.

Requirements on sample properties

For both electron beam imaging and ion beam milling all materials will have different characteristics. Materials can be placed into different categories such as metals, ceramics and polymers, but these categories can have significant overlaps and, in some cases, particular materials in a single category can have significantly different characteristics to other materials in the same category. Also many engineering samples can be constructed from combinations of different classes, for example hard ceramic coatings on metallic substrates.

One of the most important material properties that can have a significant effect on the success of the FIB milling technique is the electrical conductivity of the sample. As the electron beam will tend to induce negative electrical charge in the sample, and the ion beam will induce positive electrical charge, if the sample is not sufficiently conductive the charge build up in the sample can be sufficient to deflect the beams as they approach the sample surface, resulting in distorted images in the case of the electron beam or distorted milling patterns for the ion beam. On some FIB systems positive charge from the ion beam can be offset sufficiently by the use of an electron flood gun or the SEM column if it can produce high enough beam current but this only assists with milling precision and offers no benefit to imaging stability. Insulating samples can be coated with a suitable conductive material such as a thin film of sputtered gold but the film must be kept as thin as possible (<< 50 nm) as the technique relies on establishing the relief strain that occurs when an ion milled volume is removed and the film itself may have some residual stress that could contribute to the measurement.

When ion milling a sample some consideration needs to be given to the microstructure of the material, as substantially different milling characteristics can be exhibited by amorphous and polycrystalline materials. As a general rule amorphous materials tend to be consistent and once a milling rate has been determined it would be expected that the milling rate will not differ substantially in similar samples. However, in the case of polycrystalline materials the underlying crystallography of individual grains in the sample can give rise to large differences in local milling rates. Providing the sample has an equiaxed texture, when the grain size is very small compared to the size of the milled region, these effects can be largely neglected. However, when the grain size is large compared to the region to be milled these effects can be very substantial and present a potential problem for the FIB-DIC method. As an extreme example, Figure 11 shows the effect of milling across a twin boundary in large grain copper. In the image the twin boundary can be seen running vertically in the centre of the pillar with only one grain on either side of the boundary and small number of other grains boundaries visible outside of the milled region. As can be seen the grain on the left hand side of the boundary has

milled at greater than twice the rate of the grain on the right hand side. This effect will not only render depth profiling impossible but also may lead to non-homogenous or incomplete strain relief in the milled pillar. As a further example results from an FIB-DIC experiment on the alloy Udimet 720, which has a grain size broadly comparable to the milled Double slot geometry, is shown in Figure 12. As can be seen the slots extend across at least three different grains and performing full DIC analysis on the images shows very different peak relief strain measurements for the two regions shown due to crystal anisotropy. In this case the measurement has been performed at the level of individual grains.

The effect of milling rate for individual grain orientation should also be borne in mind when milling single crystals and materials with significant texture. While an individual sample may mill uniformly the milling rate will differ from sample to sample if the sample orientation is different on each occasion.

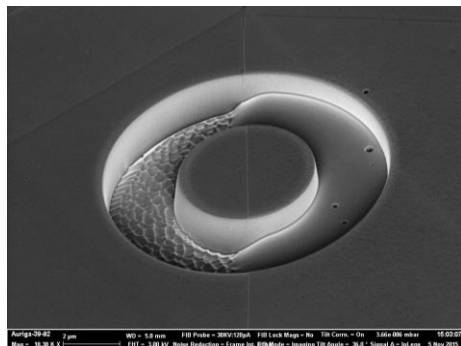


Figure 11. Example of the effect of crystal orientation on the milling rate in large grain copper.

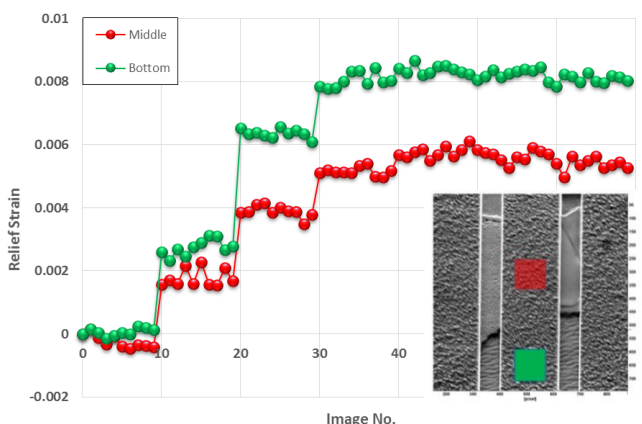


Figure 12. Example of large grain effects in Udimet 720 alloy.

In rare cases, the implantation of Ga ions from the beam can alloy with the substrate material. One of the most problematic instances is with materials containing large amounts of tin (Sn), where a eutectic alloy is formed when 8 % (atomic) Ga is mixed with Sn. Eight percent implanted Ga is easily achieved in an FIB system and the melting point for this alloy is around 18 °C. As this is likely to be lower than the internal temperature of the sample chamber the sample will have the appearance of being partially melted rather than ion milled rendering it useless for SEM imaging. Other elements that alloy strongly with Ga and are likely to be problematic are found in columns 13-15 of the periodic table. In the case of Xe plasma FIBs this problem is alleviated due to the inert Xe as the ion species.

Surface roughness and texture

For the DIC analysis to function correctly the sample surfaces should exhibit some form of random pattern, which might take the form of inherent microstructural features, an applied pattern (see Chapter 5) or a degree of surface roughness or surface features. Minor roughness (on the order of a few tens of nanometres) can be accommodated, but residual stress analyse cannot be performed on fractured surfaces and other highly uneven samples. In cases where the surface is too smooth or does not have enough features to apply the FIB-DIC method, patterning should be used to introduce features on the surface which serve as reference points during the DIC analysis for displacement tracking. Naturally occurring sample roughness and texture on the scale of 10's nm (root mean square, RMS) is ideal as in most cases it will lead to a good range of contrast in the sample and will not require any additional patterning for DIC. However, if the sample roughness is approaching the size of the milled features then there may be insufficient fine detail for the DIC to track and there could also be significant shadowing of regions of the sample for the electron beam leading to incomplete analysis.

Figure 13 shows two cases of chromium nitride (CrN) coatings in which the roughness varies from as low as 20 nm to more than 150 nm. The DIC method was successfully applied to both samples without additional surface preparation or the need to apply a pattern.

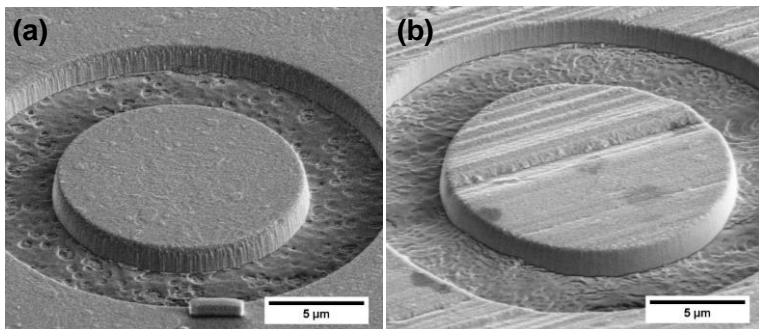


Figure 13. A CrN coating with the surface roughness of < 20 nm (left) and > 150 nm (right). For both cases the FIB-DIC method was carried out without using any filters or additional surface patterning.

Figure 14 shows two examples where surface roughness and texture proved too smooth for the DIC procedure and hence a platinum dot pattern was deposited on the surface to facilitate the DIC analysis. In the first case, a plasma-enhanced chemical vapor deposition (PECVD) dielectric layer proved too smooth and could not be processed without the addition of the external pattern. The second example shows a single crystal nickel alloy sample which does exhibit some surface features from the sub-grains, but there was insufficient detail to carry out the DIC procedure successfully and once again platinum deposition was carried out within the SEM chamber to facilitate the DIC process. More details of surface patterning techniques are discussed in the next chapter.

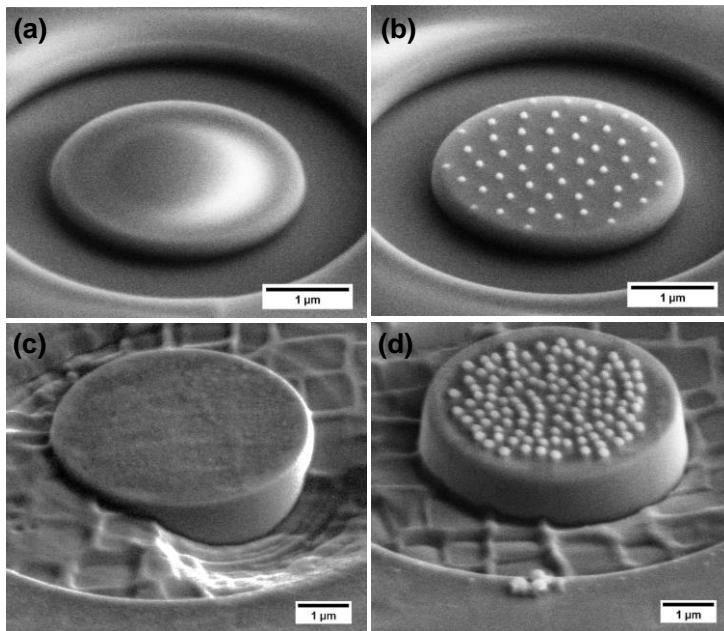
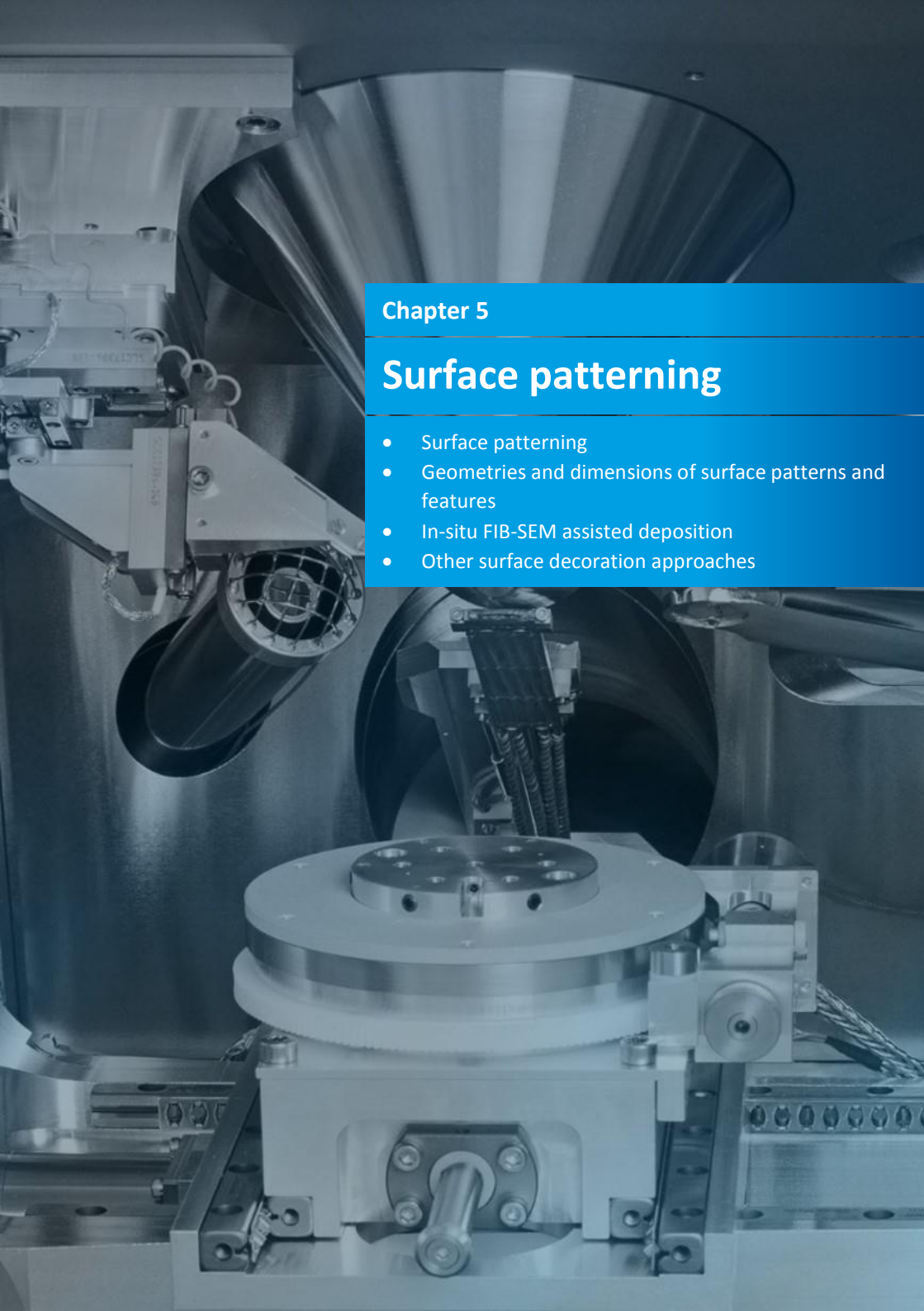


Figure 14. A PECVD dielectric layer of Si_3N_4 on Si substrate; (a) without and (b) with platinum dots; and a single crystal nickel alloy sample without (c) and with (d) platinum dots. In both cases, the dot pattern serves as a marker for the DIC procedure.



Chapter 5

Surface patterning

- Surface patterning
- Geometries and dimensions of surface patterns and features
- In-situ FIB-SEM assisted deposition
- Other surface decoration approaches

Surface patterning

For DIC to function correctly it requires features on the sample surface that can be imaged and tracked during milling. If the sample has some texture or features no additional patterning may be necessary, but if the user is unsure whether the DIC will work, a simple test is to capture an image at the required resolution and magnification and then displace the sample by a small amount (a few pixels or a small % of the image width). Then using the DIC procedure check if the DIC software can track the displacement. If the software is able to track the displacement with a high correlation value then conditions are suitable to progress to the final milling and imaging phase, without additional patterning. If the DIC check fails, then some decoration of the sample surface will be required.

Figure 15 shows images of a titanium nitride (TiN) coating, at different stages of milling. In this case the surface texture and features of the coating were suitable for DIC processing without additional patterning. In most cases, however, it may be necessary to apply a pattern to the region of the sample to be studied. The following sections give examples and procedures for decorating the sample surface with suitable features for this purpose.

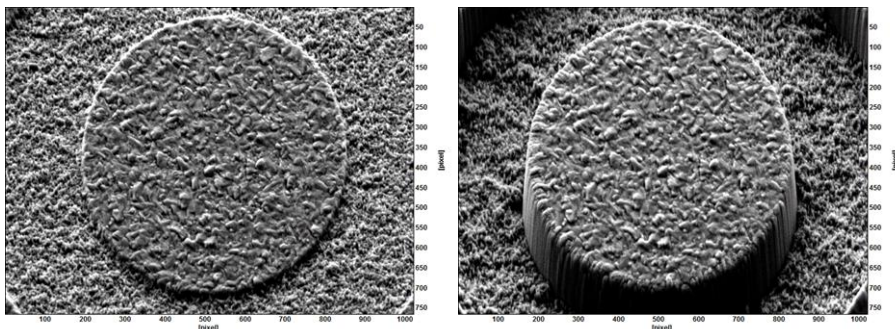


Figure 15. Example of a TiN coating, where no additional patterning was required.



Tip – Do a quick test – a simple stage movement & DIC analysis - to check if patterning is required. This is a relatively simple and quick experiment to establish whether the existing surface is suitable for DIC analysis by capturing a pair of images before and after a small sample or stage movement and analysing the image pair to determine whether the DIC analysis is successful.

Geometries and dimensions of surface patterns and features

The suitability of the pattern depends largely on the area of interest, the SEM magnification, the milling geometry, and the DIC parameters to be used for the displacement and strain calculations. If the pattern density is too sparse compared to the DIC “window” or “subset”, the DIC correlation might breakdown because there is insufficient detail and unique features to carry out the processing.

General recommendations for pattern features and size include requirements that:

- The pattern or features should be random rather than a regular grid
- Features should have an intensity gradient across their width rather than sharply defined edges
- The contrast and brightness should be chosen to give a good distribution of greyscales in the image, avoiding the extremes
- Images should exhibit low noise (achieved by filtering or integration and averaging of single noisy images)
- Best results will be achieved if the DIC window or subset covers several features to ensure that each is unique

If using a randomly generated dot pattern some variation in dot proximity will result in coalescence of dots giving an effective variation in the size of the dot pattern distribution, which is generally more desirable for the DIC calculations. The substrate on which the pattern is deposited will also affect the overall quality and nature of the pattern as seen in the images below (Figure 16), where platinum (Pt) has been deposited on silicon (Si) and a CMSX-6 superalloy.

In this example the pattern on the Si, which has a dot density of 5,000 dots per $10 \mu\text{m}^2$ appears more binary, as there is a high contrast between the substrate and the Pt dots; and the close proximity of some of the dots in the pattern has led to coalescence and a wider range of effective dot sizes, from 20 nm to almost 100 nm diameter. The dot pattern on the superalloy has a density of 12 000 dots per $10 \mu\text{m}^2$ and the higher average atomic number (i.e. density) of the superalloy gives rise to less contrast difference between the dots and the substrate. Both patterns were, however, found suitable for processing using the same DIC parameters.

The success of the pattern can be checked by examining the DIC correlation coefficient and uniformity of the DIC vector data. This is discussed in Chapter 9 later in this guide.

As noted previously, the addition of a surface pattern may not be necessary if the sample has sufficient texture or roughness features on the surface. **There are many advantages if this is the case, particularly the savings in both time and cost** from not having to apply/deposit a

pattern and the **additional flexibility for making measurements at any point on the sample**, rather than being restricted to the areas where a pattern has been deposited.

Finally, even though some samples may have sufficient texture and an inherent pattern to carry out DIC, the quality of the DIC may be improved if additional pattern is applied. Users are encouraged to investigate for themselves – do the DIC check and also if possible compare the image quality, DIC displacement fields and correlation coefficients obtained with and without any additional patterning.

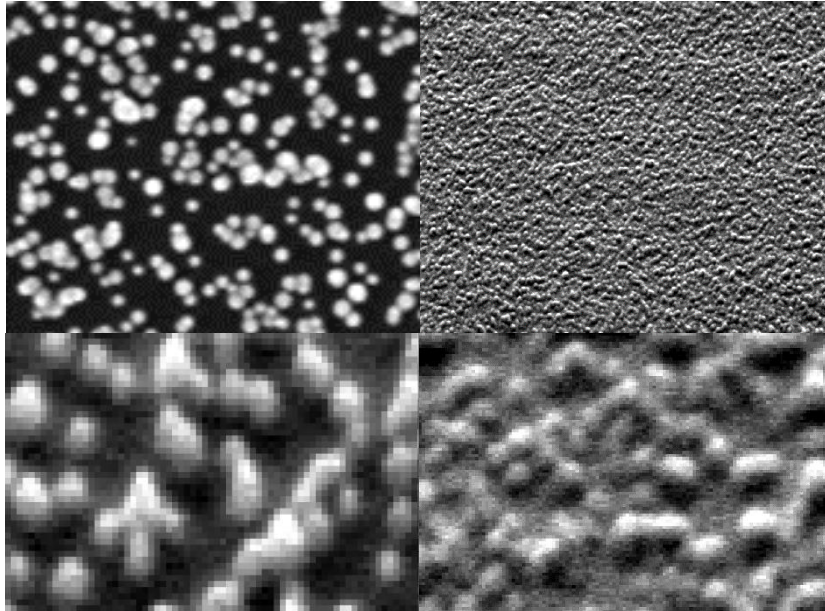


Figure 16. Representative Pt dot patterns deposited on Si (left) and a CMSX-6 superalloy (right).

In-situ FIB-SEM assisted deposition

Most FIBs will have as standard a GIS with a Pt-based precursor being the most common (then W). This material can be deposited either by electron-beam or ion-beam using the instrument's patterning software and a suitable binary dot pattern from a bitmap image, or a third-party vector-based patterning system (e.g. The NPVS patterning engine software as often found on current Zeiss instruments). **If possible the use of the electron beam is preferred with this method as the dots tend to be smaller, thus enabling a higher dot density, and the electron beam is in the vast majority of cases non-damaging to the sample.** Alternatively the ion beam can be used but this generally results in a reduced dot density, larger dots and exposure of the sample to the ion beam which may result in beam induced damage and

possible change to the stress state of the material. Figure 17 shows representative examples of dot patterns deposited by the two different beams.

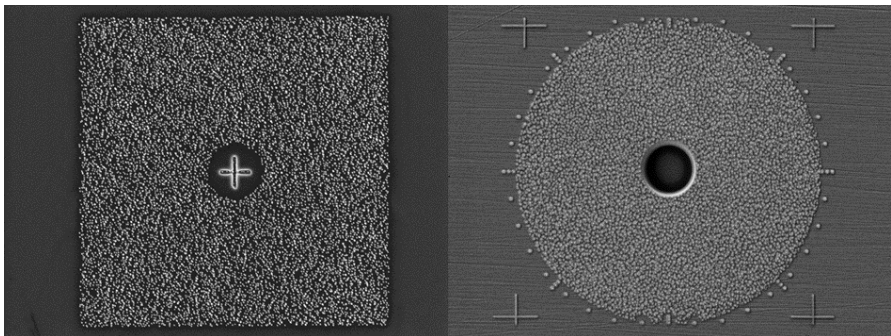


Figure 17. Comparison of dot patterns deposited by the electron beam (left) and ion beam (right).

Other surface decoration approaches

In some cases, FIB-DIC experiments may benefit from having a pattern deposited over a large area or even the whole sample (depending on the sample size and nature) and alternative approaches to depositing a fine pattern external from the FIB have been developed. This may be beneficial, for example, when a series of milling experiments are being made and it is not cost effective or practical to deposit a large number of GIS deposited patterns. Using FIB or electron beam (EB) deposition techniques is both expensive and time consuming and milling is then restricted only to those areas where the pattern has been applied. As an alternative approach to patterning, external sample surface decorations may be used. Various methods and techniques have been tried and developed, depending on the type of the material and size of the sample and area of interest. These include using yttria-stabilised zirconium (YSZ) particle deposition [36], gold layer remodelling [37], and colloidal silica etching. Examples of some of these are shown below.

Figure 18 shows an example of using YSZ particles of size 20-30 nm that have been precipitated from 40 % aqueous ethanol suspension and dried at room temperature.

In order to protect the sample surface from Ga^+ implantation and minimise sample charging, the surface of the specimen was coated with carbon film which assists in attaching the particles to the sample surface. The coverage of the sample surface is controlled by particle density in the ethanol suspension and the number of repetitions. This method can cover large areas, give sharply defined surface decoration but is not easy to mask within very small areas, and the deposited pattern can be inhomogeneous.

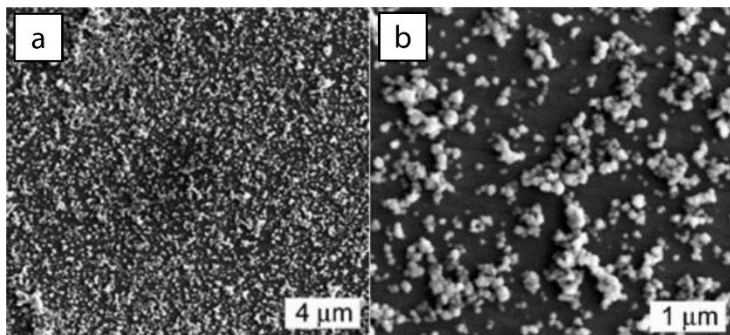


Figure 18. Examples of external patterning using yttria-stabilised zirconium particles [36].

Another method that has been developed and is suitable for covering large areas is remodelling of a gold deposited layer. The method was developed by Luo [38] and first proposed by Scrivens [39] and Gioacchino and Quinta de Fonseca [37] who have used it to present DIC maps of plastic strain in metals. The technique works by covering the sample surface with a thin layer of gold nanoparticles and using a heat source to generate vapour which causes the gold to cluster into small particles to create a separate and distinct gold speckle pattern. The gold nanoparticles are usually applied to the sample in solution and meticulous surface preparation is important as both the physical finish (surface roughness) and chemistry (surface energy and cleanliness) can affect the success of the pattern. The form of the final pattern also depends on the thickness of the gold layer, and the time and temperature used in heating process and vapour. Figure 19 shows examples of the type of pattern that can be produced with this approach [37].

With all these patterning techniques it is essential that the process of applying the pattern itself does not change the nature of the surface, particularly the residual stress state that is present, which is a potential issue when temperatures are involved. The pattern must also remain securely attached as the sample is strained. There may also be issues with having a pattern on the sample if other techniques (e.g. EBSD, nanoindentation etc.) are being used to make measurements at the same position.

Generally, the gold remodelled patterns have been used for high resolution studies of strain and plasticity during in-situ testing in the SEM [37], and not with FIB-DIC milling. Observations have been made (Figure 20) where the milling process itself causes modification to the pattern leading to significant errors and strain artefacts, so care should be taken.

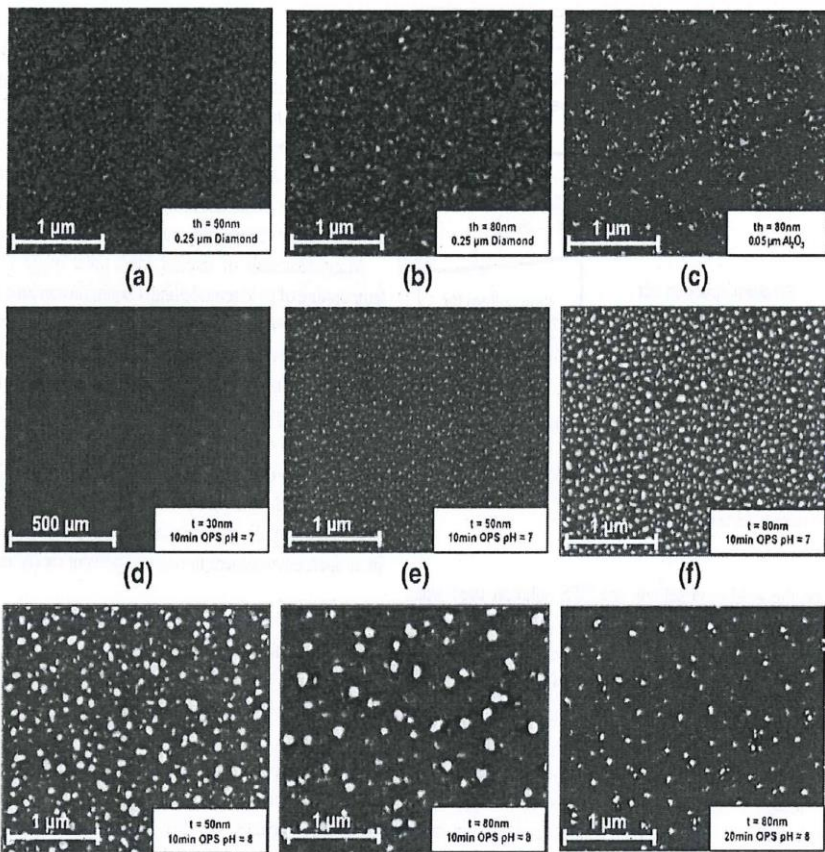


Figure 19. Examples of gold vapour remodelled patterns [37].



Tip – It is a general recommendation that the stability and robustness of any pattern is examined for milling induced changes, particularly if these extend into the areas over which the DIC processing and strain calculations are carried out.

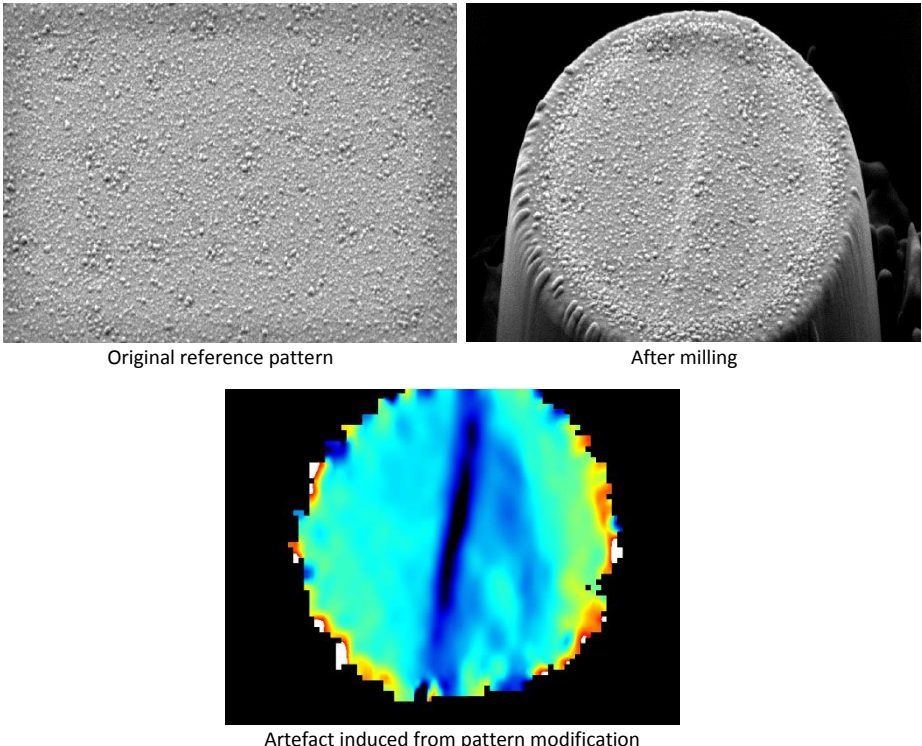


Figure 20. Example where a deposited gold pattern has been modified by the milling process itself leading to induced strain artefacts and errors.



Chapter 6

Milling conditions and issues

- General milling parameters
- Establishing the milling rate
- Measuring the milling depth
- Minimising ion beam damage
- Strategies for best depth resolution and deposition reduction

General milling parameters

A number of factors should be considered depending on the particular experiment, milling geometry and material being examined. Modern instruments offer many possibilities for milling strategy, but **it is generally preferable to mill with a low ion dose per pass of the pattern and undertake many repeat passes.** Factors such as beam dwell time, beam current and beam overlap can control the ion dose. Generally, the beam overlap is fixed to at around 50 % of the beam spot size with the beam current chosen appropriately for the volume of material to be removed in a reasonable time. The beam dwell, i.e. how long the beam sits at each point in the pattern, is for most patterning the single biggest influence on ion-dose over the milled area. As the milled volume is determined by the total dose over the area, if the beam dwell time is low then the number of repeats over the area must be high. This is found to be preferable to attempting to mill with a high beam dwell and fewer passes, as the latter tends to lead to more redeposition and milling artefacts.

Establishing the milling rate

Establishing the milling rate of the material is important for the FIB-DIC process. Firstly, the depth of the geometry to be milled must be sufficient to fully relieve the stress in the sample, or be of a known depth for a given dose if the stress is being profiled. The required milling depth can be directly attributed to the ion dose the sample is subjected to. Furthermore, a knowledge of the milling rate enables the user to adjust the beam current to achieve the required depth in a reasonable time. The milling rate of materials is very dependent on the composition and crystallinity of the material. The milling rate can be thought of as the amount of material removed for a given ion dose and is derived from the sputter yield (sputtered atoms per incident ion) and the beam current (i.e. number of ions in the beam). Generally, sputter yield scales with the density of the sample. For alloys, compounds and amorphous materials the sputter yield will depend on the composition of the alloy, the bonding and any other phases present in the material amongst the many other possible variables that make up engineering materials.

If the milling rate of a new material is to be established or if significant changes have been made to the instrument then it may be necessary to adjust dose accordingly and re-test the milling rate for the material.

In some cases, a material will not mill uniformly. The most prominent example of this is found in polycrystalline samples. In this case, ions will sputter different numbers of atoms from individual crystals (grains) in the sample depending on their orientation with respect to the ion beam. This phenomena (known as ion channelling) is extremely difficult to compensate for owing to the often unknown orientations and grain sizes of the material before a measurement is carried out. In the vast majority of these cases, milled depths will vary over an

area that has been subject to a uniform ion dose and may result in roughness on a scale approaching the grain size.

If a milling rate cannot be established with an acceptable degree of certainty, depth profiling of the residual stress will not be possible. Additionally, establishing any residual stress value in the sample will require the milled depth to be sufficient to cause a saturation of the strain relief. In cases where the sample will not mill sufficiently uniformly it will be necessary to mill the whole region to be removed to depth known to be beyond the saturation limit even if parts of this region are substantially deeper.

To establish the milling rate it is recommended that a series of milling tests are carried out with a new material, particularly if depth profiling is being carried out as it is important to know how deep the specific geometry has been milled at all stages of the test. This is not so critical if milling to full depth provided the geometry has been milled sufficiently deep to achieve full strain relief but a knowledge of the rate is still useful to achieve this.

The examples in Figure 21 below show data from calibration tests on a TiN coating, a Si_3N_4 coating (both on Si substrates) and a BMG specimen. In all cases a set of circular holes of $3 \mu\text{m}$ diameter were milled with different doses and the depth measured to define a calibration curve. The tests were repeated several times to get an average value for the milling rate, and dose rates varied from $1\text{-}6 \text{nC}/\mu\text{m}^2$ to cover the range that is typically used for these materials to achieve suitable depth for stress determination.

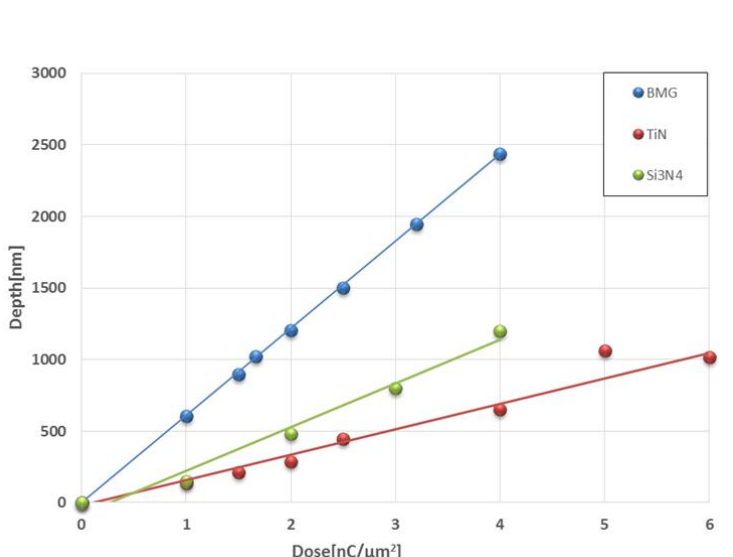


Figure 21. Representative milling rates for FIB milling in a BMG, Si_3N_4 and TiN coating.

In reality, the milling rates calculated from similar experiments should only be considered as a guideline and as can be seen for some samples some deviation from linear is observed. In many practical cases, the actual milling rates achieved are not constant with depth due to a number of factors such as stress gradients, local material density variations (particularly for thin films) and changes in grain size. As can be seen in the example above the BMG sample produced very consistent data with a very linear milling rate whereas the Si₃N₄ sample increased in rate with depth and the TiN sample had a higher scatter but was broadly linear.

Additionally at higher milled doses there tends to be a reduction in milling rate as the slot/geometry becomes deeper due to a combination of redeposition, and the increasing aspect ratio of the milled geometry that leads to some screening of the beam, making the milling less effective. **Generally, for most materials, an aspect ratio of 2:1 for depth to width of milled holes would be deemed within safe limits to achieve reasonable depth accuracy** but this may be lower for materials particularly prone to redeposition such as polymers.

Measuring the milling depth

The FIB-DIC residual stress method is intrinsically a surface analysis technique, but in many cases the location of the most critical residual stress lies below the surface. In order to access this location, sample sectioning has to be performed, but the sectioning process itself can relieve the stresses in the direction normal to the newly created surface, thereby modifying the residual stress state in the area of interest. If full depth and full strain relief has been achieved then this is not an issue. Otherwise, simple approximations can be developed based on the relationship between the initial and modified stress state using the comparison between plane strain and plane stress relationships, respectively [40], but to fully understand the interaction, more complex FE simulations are required involving intrinsic parameters such as eigenstrain [41, 42].

The destructive nature of sample sectioning can also induce residual stresses during sample preparation, so gentle removal techniques should be used to remove material from the sample surface, for example electrical discharge machining [43], diamond wafering [44] or grinding. Incremental fine grain polishing, heavy ion beam polishing [45] or electropolishing [46] can then be performed to reduce the depth of the residually stressed region. The exact magnitude of stresses induced and the region over which this influence extends is highly dependent upon the substrate material and polishing regime. However, FIB milling and DIC based techniques are typically highly sensitive to near surface effects, and therefore this behaviour is known to influence the measure of residual stress originally present in the sample.

Depending on the milled geometry it may be possible to measure the depth of the image without further sectioning by measuring the ends of the slots or side walls of the geometry milled. The images below show the measurement of the final depth of the Double slot

geometry. Alternately the milled profile can be filled using the standard deposition gas in the FIB, such as Pt or W, and this may help to define and highlight the milled geometry to aid the measurement of depth, profile and other dimensions.

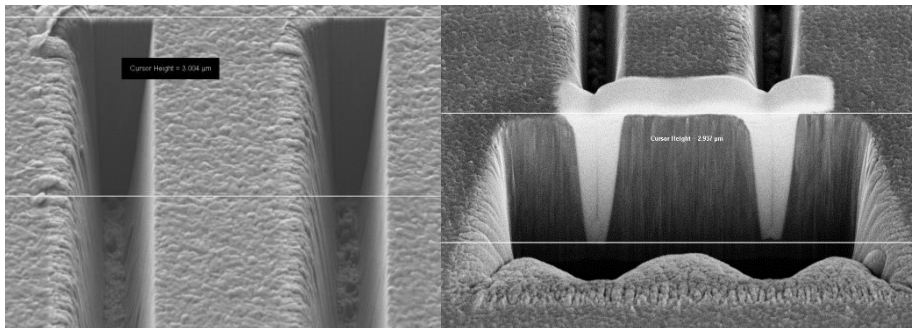


Figure 22. Determination of depth of Double slot geometry. Measuring the ends of the slots (left) and measuring by filling the trenches with Pt and cross-sectioning (right).

Because there may be some local variation and possible uncertainties in identifying the top surface and bottom of the milled feature, it is recommended that a number of repeat measurements are made, and the average depth used. In the example above this was carried out at the end of the milling stage, after all the DIC images had been captured, tilt corrected for cross sectional measurement. For some of the milling geometries being used if the holes are very deep it is likely that sectioning and milling of the cross section will be required to accurately establish the final depth.

Although it is recognised that the milling rate is not always uniform with depth, unless “real time” measurements of the milling depth can be made at each milling increment a uniform milling rate should be assumed. For calculations of the average stress the variation of milling rate is not important and all that needs to be measured is the final depth, but if stress profiling is being carried out it is important that the true depth is measured (or at least estimated with some consideration of the potential change in milling rates with depth) as this will affect the final calculated stress profile.

In many cases, particularly with high ion-beam currents, due to the Gaussian shape of the beam some beam tail effects may affect the final geometry, as will redeposition of milled material and the particular difficulties associated with milling certain materials. The final milling geometry may deviate somewhat from the target geometry but it has been shown that the actual final shape (parallel sided or modestly tapered slot) has little effect on the relieved strain, providing the effects are not significant. The change in milled profile tends to be more pronounced as the milling depth increases and the associated magnitude of surface strain relief is reduced (strain sensitivity). A discussion of beam damage and redeposition is covered in the next two sections along with strategies to reduce their effects.

Minimising ion beam damage

The process of ion beam milling involves bombarding the surface of the sample with high energy ions to effect material removal. Although on the macro-scale this approach is very gentle, locally this ion interaction causes ion implantation and possible amorphisation which can lead to the enhancement of material defects, local changes in material properties, inelastic shrinking or swelling and the generation of residual stresses [47, 48]. The ion damage affected zone is believed to be confined to layers between 10 and 100 nm thick from the edge of milled trenches, depending on the ion energy, target material and angle of incidence. This phenomenon introduces a resolution limit for FIB milling and DIC based techniques, below which ion milling itself begins to affect the residual stress state perceived. The impact and location of the ion radiation damaged zone is also dependent upon the choice of milling geometry, with some techniques proving to be more robust than others.

The degree of material amorphisation as a consequence of FIB irradiation can be studied in some materials and visualised using EBSD, a technique that is capable of capturing the underlying crystal quality and orientation by probing a shallow material layer with sub-micron spatial resolution. With EBSD a target material is illuminated by an electron beam that undergoes diffraction, producing a so-called Kikuchi pattern. The degree of material crystallinity affects the quality of these Kikuchi patterns, so that the pattern quality is progressively reduced, and in the extreme case of fully amorphous material the pattern is entirely destroyed.

Quantitative assessment of the quality of Kikuchi patterns can be correlated with the degree of material amorphisation in some materials. As an example in an experiment on a Si wafer, different areas of the sample were exposed to several distinct Ga ion doses, and the loss of Kikuchi pattern quality was measured using EBSD. The same approach was then used to evaluate the consequences of ion beam exposure for geometries of interest when ion beam milling is employed in the FIB-DIC method of residual stress measurement.

As can be seen in Figure 23, the degradation of the Kikuchi diffraction pattern as a function of dose provides a useful and sensitive indicator of amorphisation. The results show that for doses in excess of ~ 2 ions/ nm^2 the diffraction pattern is almost completely destroyed. This corresponds to the amorphous fraction $> 70\%$. In other words, although EBSD analysis loses sensitivity at large amorphisation levels, it is very sensitive under low dose conditions. It has been shown that the transition from a fully crystalline to amorphous state in Si involves an increase in volume with the volume change likely to be on a similar scale (i.e. nm per mm^2) to that detected by DIC in the FIB-DIC method.

FIB manufacturers give quoted values for ion beam spot sizes and while it is known that the beam tails extend well beyond the beam core determining the extent of the tails is difficult to carry out and rarely discussed. Usually, the beam spot size is defined using the Full Width at

Half Maximum (FWHM) of the Gaussian peak function, but this description does not fully account for the presence of the tails, which might extend to the region of interest over which the DIC displacement and strain measurements are being calculated. This is particularly important in thin films, where the thickness and dimensions may be only a small multiple of the beam interaction depth.

The FWHM of the beam increases in size as the beam current of the system is increased and can result in a very significant number of ions in the tails beyond the FWHM. As an example Figure 24 shows the effect of a focused 5 nA beam in single spot mode on Si for three different beam dwells. At a beam dwell of only 1 ms the extent of the crystalline damage caused by the beam tails can mapped by EBSD is shown to be over 4 μm in diameter. It is important to note that the manufacturers quoted FWHM beam size for this beam current is extremely small: it is equal to ~ 170 nm and is represented by the white circle in the 1ms map on the left. It follows that even at low exposure times the amorphous region far exceeds the beam spot size, i.e. it is observed that the effect of beam tails extends over many microns. At higher exposure times or for a greater number of repeats of a pattern required to remove a volume of material, the beam tail effect becomes considerably more pronounced.

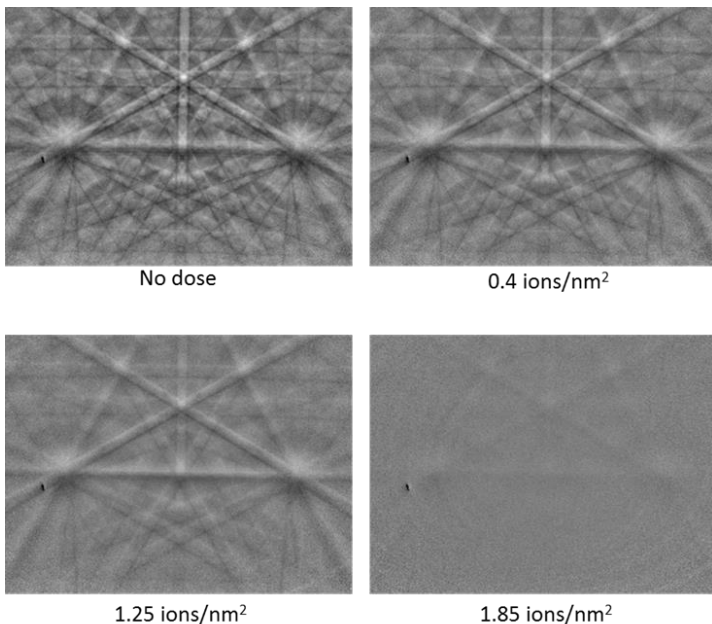


Figure 23. EBSD Kikuchi patterns in Si showing the effect of increased exposure to Ga ions on the level of amorphisation.

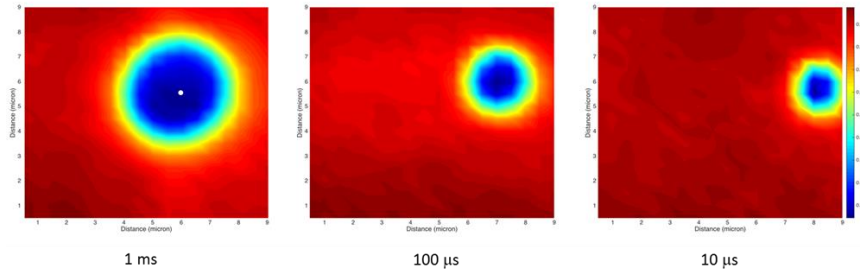


Figure 24. Extent of amorphisation in Si caused by a focused 5nA beam with different beam dwells.

To examine the potential impact of beam tails on the FIB-DIC method used for residual stress measurement, a series of maps were acquired over the field of view once the milling process was completed. This was performed for the Double slot and Ring-core geometries using a 120 pA beam current and 30 keV ion beam energy. As seen from Figure 25, the FIB-affected region where the material has been fully or partially amorphised extends far beyond the region used for displacement evaluation by DIC. It is also obvious that this process is associated with the introduction of structural changes that are associated with permanent strain (eigenstrain) and hence lead to residual stress modification. Finally, it is worth observing that the path traced by the beam during milling was captured by the technique used here, as visible in the Double slot example (streaks from the bottom right of the map) that are probably caused by delay in the actuation of the ion beam blanker.

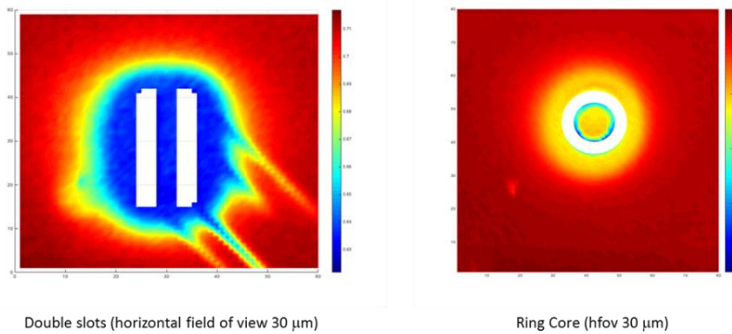


Figure 25. Amorphisation degree maps around FIB-DIC (a) Double slot and (b) Ring-core milling geometries.

EBSG has been shown to be a suitable technique for the qualitative assessment of the loss of material crystallinity/material amorphisation following exposure to Ga ion beam. The analysis of a single spot exposure showed that the effect of beam “tail” is increasingly significant at high ion currents.

While not all materials will retain ion damage in the same manner as Si (due to its covalent bonding) all materials will undergo microscopic structural change due to the presence of ion interactions, and these effects could alter the stress state of the material in the region being studied. Measurements of the extent of beam tails for given spot sizes indicate that for a given geometry, **milling for the FIB-DIC procedure is best done at the lowest possible beam current** acceptable within a tolerable duration of the experiment. While it is possible to mill the geometries described here in under a minute, in most materials the required beam current would be very high and the subsequent beam tails cause considerable damage to the surrounding material. Milling with reduced beam current increases the time the sample is exposed to beam tail effects, but the extent of the tails is reduced in the lower beam currents, and in the **vast majority of samples studied beam currents ranging from 50 to 600 pA have proved to be most conducive to milling in a reasonable time and with tolerable beam damage.**

Strategies for best depth resolution and deposition reduction

When an ion beam is milling a sample, ejected atoms, ions and clusters are removed from the sample surface. The majority of these particles are ejected far enough from the region being milled to be pumped away by the vacuum system with some condensing on the instruments chamber walls or condensing on regions of the sample far from the milled region. However, some materials (polymers in particular) are known to redeposit very close to the milled region and, additionally, a poor selection of milling strategy can result in significant redeposition problems.

Figure 26 shows examples comparing the effect of different milling strategies on the final milling geometry. The image in Figure 26 shows three sets of parallel trenches milled in a TiN coating, 3 µm apart and aiming for 2 µm deep. They have been filled with I-beam deposited Pt and then cross-sectioned to show the depth and shape of the trenches. Different milling strategies have been used for each set but in all cases the total dose to mill the trenches was the same. A 100 pA beam current was used with a 12 nm beam step. The beam dwell at each point was adjusted and compensated for by altering the number of repeats of the pattern. Figure 26a shows the effect of low beam dwell (1 µs) and 1200 repeats, Figure 26b shows the same dose but taking 10 repeats with a corresponding longer beam dwell (120 µs) per point and Figure 26c shows the effects of the same dose but in a single pass with very long beam dwell time (1.2 ms).

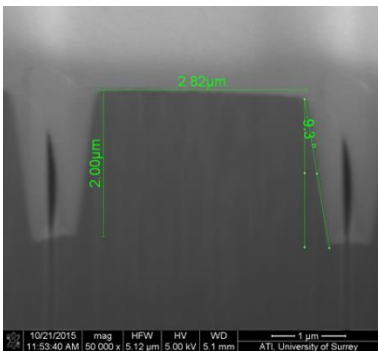
In the case of the multipass, low-dwell time milling, Figure 26a, there is very good depth accuracy and reasonable definition of the milled geometry with minimal redeposition. There is some reduction of width between the trenches at the top with the trenches tapering towards the bottom giving a taper of about 9° due to the beam tail effects but is within acceptable

limits. As the dwell time increases the desired/target milling geometry is less well defined, Figure 26b, with an increase in depth on one edge of the trench and a significant reduction on the outer edge of the trench. This effect is a good demonstration of a further consideration to be taken into account, **the direction of the beam path can also affect the final geometry**. When milling Double slots for example, it is preferable to begin the trench at the outer edge working in towards the centre for both slots. Redeposited material as a general rule tends to deposit on the faces that were exposed first with the last face exposed having little or no redeposition. This is highlighted even more clearly in Figure 26c where the geometry is severely compromised when the instrument conditions/settings are set to mill the geometry in a single pass. In this case there is extensive redeposition, visible as the mid-grey material in the trenches, and it is also clear in this case that even though the total dose is the same it is not possible to achieve the correct depth.

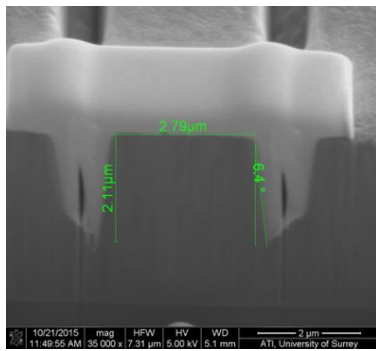
Figure 26d shows further evidence of problems milling with long dwell times. This plot compares the actual milling depth achieved for a single pass and multipass strategy. As can be seen repeating sets of many low dose passes to achieve a target depth is found to be reasonably linear and achieves good agreement with the target depth. However, when repeating high beam dwell single passes and using the same dose per depth as the multipass shows a significant over milling at low repeat numbers, but then tails off rapidly following an approximate $d^{1/2}$ relationship. This effect would be a major issue if incremental milling is used to measure the strain relief and residual stress with depth as the depth is clearly not constant as the milling goes deeper.

As a general rule therefore the best depth resolution combined with reduced deposition is achieved with fast beam dwell times of 1-2 μ s (certainly less than 10 μ s) and as many repeats of the pattern as necessary to achieve the depth. Attempting to reduce the number of repeats does not save time as the overall dose to remove the material is fixed. Increasing the beam current may save considerable time but may result in unwanted beam tail effects modifying the stress state of the region of interest.

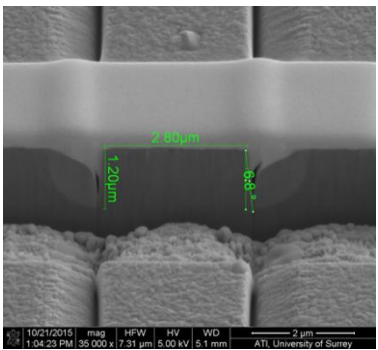
In addition to its effect on the shape of the milling geometry and efficiency of the milling process itself, redeposition of material on the surface can change the quality of the features (the natural surface or applied pattern) used by DIC to track the surface displacement, thereby increasing the uncertainty in the final stress estimate. As mentioned earlier, milling at reduced rates (i.e. low ion beam current) or reducing the amount of milled material also reduces material redeposition on the sample surface. An alternative approach is to apply a deposition barrier [19] or Si mask between the DIC region and the milling location. This has proven to be successful at reducing redeposition, but it does increase the experimental time and may influence the residual stress state prior to measurement.



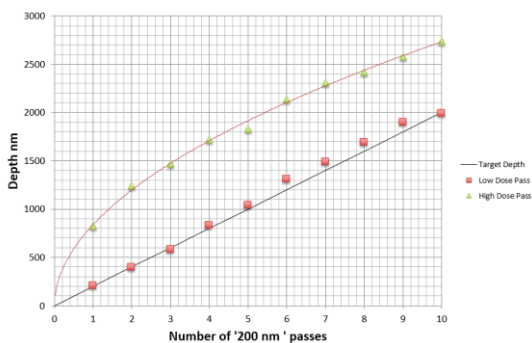
a) Multi-pass Milling: Approximately 0.6 nm removed per pass



b) Multi-pass Milling: Approximately 200 nm removed in each repeat pass



c) Single pass: To full depth in 1 pass of the beam



d) Comparison of milling strategy on the actual depth achieved

Figure 26. Comparison of milling profiles developed in TiN using different milling strategies.

This page was intentionally left blank.



Chapter 7

Recommended FIB milling geometries

- Recommended FIB milling geometries
- Surface slots/trenches
- Double slot and H-bar milling
- Ring-core milling
- Hole drilling
- Selection of the best milling geometry
- Effect of elastic anisotropy

Recommended FIB milling geometries

Advances in FIB software and hardware have in recent years greatly expanded the range of geometries that can be milled using ion beams. This flexibility has enabled a wide range of FIB milling and DIC residual stress analysis techniques to be developed. Each technique has been designed to meet the needs of the specific application or to quantify a particular stress state of interest, and therefore has particular advantages and limitations when compared to others. Examples of the different geometries are shown in Figure 27 and discussed in the following sections.

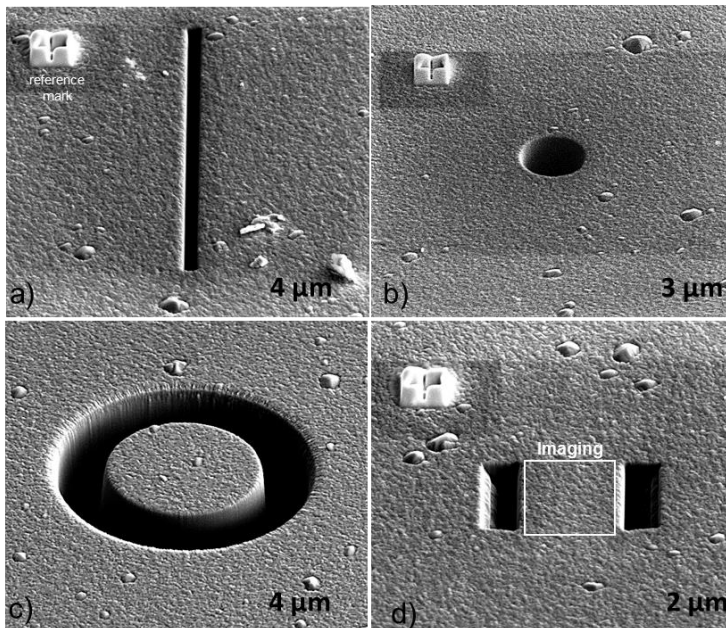


Figure 27. Examples of typical milled geometries used in the FIB-DIC procedure.

Surface slots/trenches

FIB micro surface slotting was the first published application of the FIB-DIC residual stress measurement technique [8] and is based on the miniaturisation of the macro-scale crack compliance method [49]. The approach is based on milling a single narrow slot or trench into the material surface (Figure 27a). In order to quantify the displacement field, DIC is performed on SEM images of the regions on either side of the slot. A comparison between the relief observed and that from FE simulations [50] or appropriate analytical solutions [8, 15], is then used to back-calculate the average residual stress in the direction perpendicular to the long

axis of the slot. The surface slot approach has the advantage of a simple milling regime and can be used for measuring stresses in very thin films. Recent developments have extended this approach to provide depth resolved measurements [26, 51] and spatially resolved analyses [17, 52, 53].

In addition to the obvious limitation of only providing one of the normal tensor components of the in-plane stress by a single slot, micro-slitting also requires FE simulations to extract stresses from the strain relief [54]. The magnitude and gradient of the displacement relaxation field on both sides of the trench (Figure 28) depend on the trench geometry, material properties and stress state normal to the trench line. Unlike other milling patterns, such as the Hole or Ring-core geometries, a simple master curve for an average measured relaxation strain as function of the residual stress and milling depth does not exist. FE simulations taking into account trench profile and elastic material properties have to be used to match theoretical relief displacements with the measured values. Also, unlike the Hole, Ring-core and Double-slot geometries complete stress relief at the sample surface cannot be achieved, so a simple mathematical relationship between complete relief strain and the original residual stress is not available.

The higher complexity of stress determination from the release displacements makes this milling geometry favourable to some of the others, particularly if those geometries lead to severe strain gradients, which cannot be neglected. This is the case for thin films with thicknesses in the sub- μm region, where for example, milling of isolated pillars with sufficient surface area of constant strain for sufficiently low aspect ratios becomes difficult. Furthermore, the shape of the trench strain field depends on stress and Young's modulus, which in general enables measurements of both of them. DIC capture of displacement fields in slices along longer narrow trenches opens access to lateral stress gradients and in doing so, a lateral spatial resolution of 100 nm has been demonstrated [55].

Details about corresponding data analysis and stress calculation for the surface slot/trench geometry is given in Chapter 11 and Appendix 2 of this GPG.

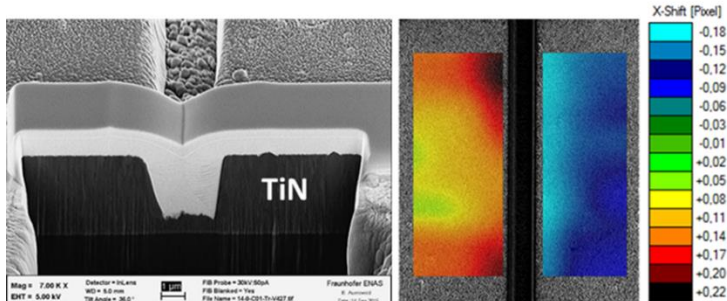


Figure 28. Typical trench milling feature.

In Figure 28 above the trench profile has been filled with Pt to improve the contrast, and the typical DIC displacement field in the vicinity of the trench middle is shown on the right. The left and right displacement fields exhibit a discontinuity crossing the trench line and a sharp gradient with distance from the centre of the trench. Small variations in the displacement field in the direction parallel to the trench axis are caused by tiny SEM stage drifts during image capture, but they can be suppressed in the stress extraction algorithm, which is sensitive to the relative displacement changes in the horizontal SEM line scan direction only.

Double slot and H-bar milling

The Double slot or H-bar geometry was originally proposed by Krottenthaler et al. in 2012 [33]. The approach is based on milling two identical trenches/slots on either side of the central gauge volume (Figure 27d). The estimate of the residual stress component in the direction perpendicular to the long axis of the trench is then obtained. In comparison with the Single slot method described above, the H-bar has a more precise gauge volume definition both in terms of position and size. Similar to the Ring-core methodology, this approach also benefits from uniform strain relief across the central bar/island, and from the increased magnitude of the surface strain relief. This geometry also enables DIC analysis to be performed over relatively large regions, thereby improving DIC marker averaging compared to the Ring-core approach.

The main limitation of the H-bar approach is that the technique only provides stress quantification in 1D, but a recent publication by Sebastiani et al. extended this technique to 2D by milling a series of additional slots perpendicular to the originals to leave a fully relieved core in the form of a square [28]. This final geometry is very similar to the Ring-core approach, but by employing a 2-stage milling process (first parallel bars, then additional cross lines) it can be used to calculate the Poisson's ratio behaviour at the micro-scale.

Ring-core milling

The micro-scale Ring-core FIB milling and DIC approach was first proposed by Korsunsky et al. in 2009 [11] and is based on the miniaturisation of the macroscopic Ring-core method originally developed by Keil [56]. With this method an annular milling pattern is used to obtain full strain relief of a core of material lying at the sample surface (Figure 27c). This approach ensures that the gauge volume (central core) is well defined both in terms of position and size. Due to the isotropic milling geometry, by examining the strain relief in the core in different orientations the Ring-core technique can provide a quantitative measure of the complete 2D in-plane stress state in the sample of interest. Other advantages of this geometry include the fact that the strain relief observed in the core is typically much larger in magnitude than for the micro-scale Hole drilling (exterior field) and micro-slotting methods. Since the displacement values are larger, the method is therefore more robust with respect to noise. It has also been shown that the strain relief induced across the centre of the core is

predominantly uniform [57], ensuring that effective averaging can be used to improve the robustness of interpretation. Finally, the use of a central core, rather than a reliance upon surrounding region means that pattern markers can be placed close together for high resolution spatially resolved analysis [40]. Depth resolved analysis has also recently been demonstrated using this technique [58].

The main issue associated with the micro-scale Ring-core FIB milling geometry is the scale of the region over which the DIC analysis is performed, which is typically smaller than the other milling geometries. In order to overcome this limitation, an approach based on incremental milling and repeated SEM imaging has been developed [27, 16, 59]. This methodology provides a record of the average strain relief within the central micro-pillar “island” or “core” as a function of milling depth which is then compared with the results of FE modelling. The use of multiple milling steps and images greatly improves the precision with which strain can be determined, in contrast with the simple comparison between only two sets of SEM images taken before and after milling. Further improvement is afforded by analysing subsequent images, thereby improving the reliability of the DIC marker tracking and accuracy.

Hole drilling

FIB micro Hole drilling was first published by Sabaté et al. in 2007 [14] and is based on the miniaturisation of classical macro-scale blind Hole drilling method originally developed by Schajer [60]. This approach provides a measure of the 2D stress state in the surface of interest by milling a small circular hole into the sample surface (Figure 27b). DIC of the surrounding region is used to quantify the strain relief field induced by milling in order to provide an estimate of the stress state originally present. Micro-scale Hole drilling benefits from being experimentally simple and fast, and depth-resolved extensions of this technique have recently been reported [25].

Despite these improvements, micro-scale Hole drilling relies on the DIC analysis of the stressed regions **outside the gauge volume location**, and therefore suffers from reduced gauge volume precision in a similar way to surface slots/trenches. Another difficulty associated with this experimental approach is the limited amounts of strain relief induced by milling. The impact of noise on the perceived residual stress values are therefore far greater than for other methods, and the solution of the inverse problem associated with this technique requires careful regularisation [25]. Regularisation reduces unrealistic variations in the stress values obtained, but also limits the sensitivity of the technique.

Selection of the best milling geometry

Table 1 below summarises the key attributes and applications of the various milling geometries considered in the FIB-DIC procedure. The final choice of geometry, however, will

often depend on the material and sample of interest, the stress state and in some respects the capability of the FIB and expertise of the user.

Milling Geometry	Stress state resolved	Depth resolved measurements	Pros	Cons
Single slot or trench	Uniaxial	YES - but slope of trench has a significant influence	<ul style="list-style-type: none"> Simple and fast 	<ul style="list-style-type: none"> Low spatial resolution Only single component measure of residual stress Strain relief decreases rapidly from the edge
Double slot /H-bar	Uniaxial		<ul style="list-style-type: none"> High positional accuracy Large gauge volume Uniform strain relief 	<ul style="list-style-type: none"> 1D stress quantification
Ring-core	Biaxial		<ul style="list-style-type: none"> High position accuracy Complete 2D in-plane stress estimation Uniform strain relief 	<ul style="list-style-type: none"> Small gauge volume
Hole drilling	Biaxial	YES – and the possibility of using same equation as in macro-scale	<ul style="list-style-type: none"> 2D stress quantification 	<ul style="list-style-type: none"> Complex strain field around the hole Strain relief decreases rapidly from the edge Low spatial resolution

Table 1. Summary of the merits and applications of the different milling geometries.

Although a wide range of milling geometries are possible and have been used in the studies reported in the literature, within the iSTRESS project standard geometries and dimensions were proposed for the Single slot, Double slot and Ring-core cases. These have been chosen, based on a combination of practical measurements and FE studies, details of which are presented later in Chapter 10.

The recommended geometries are summarised in Figure 29 together with representative images showing the typical field of view and location of the areas over which the DIC displacement/strain fields should be measured (the gauge volume in pink).



Tip – If the FIB instrument and images are susceptible to drift it might be necessary to allow for this and zoom out slightly. It is important to make sure that the field of view (FOV) is unaffected by end effects so it is recommended that the full slot length is always milled.

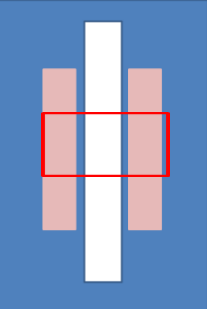
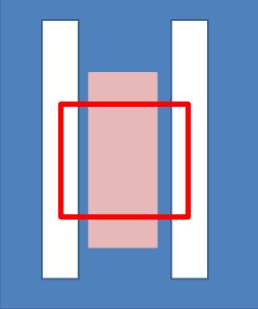
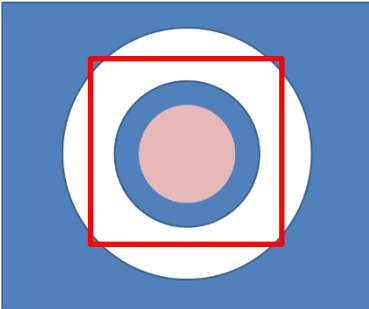
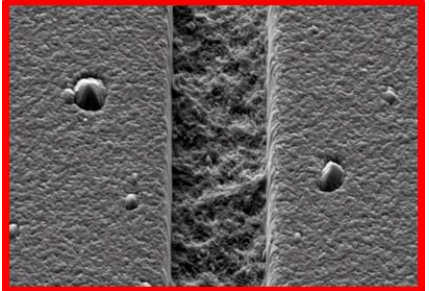
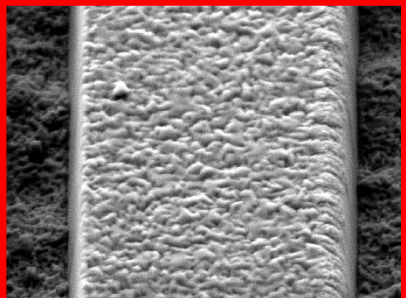
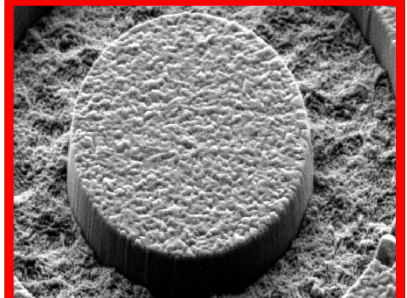
Single slot geometry Target dimensions are: 3 μm wide slot x 60 μm long	Double slot geometry Target dimensions are: 2 x 1 μm wide slots 3 μm apart (between the inner edges of the slots = width of free standing lamella) x 12 μm long	Ring-core geometry Target dimensions are: Diameter of central island 5 μm Width of trench/ring 2 μm
		
		

Figure 29. Recommended milling geometries, and the corresponding fields of view for DIC analysis.

Effect of elastic anisotropy

Engineering reliability and durability analysis for design, e.g. against creep or high cycle fatigue, conventionally uses criteria based on stresses, rather than strains. For isotropic materials, the stress calculation can be readily performed using the combination of only two elastic parameters: Young's Modulus, E , and Poisson's Ratio, ν . However, care must be taken for the case when the material is anisotropic and possesses cubic symmetry. The uncertainty of residual stress evaluation, at the inter- and/or intragranular level, depends on the material's degree of anisotropy. Therefore, in materials with high anisotropy factor the knowledge of grain orientation is mandatory in order to accurately evaluate stresses.

To clarify this issue, Figure 30 shows an example of the FIB-DIC method (H-bar geometry) on an annealed copper sample, where only 2-3 grains with unknown orientation are involved in the relaxation process. In the case of copper, a significant difference between the elastic properties along the [111] and [100] lattice directions is reported [61], being $E_{111}/E_{100} = 2.87$, whilst the anisotropy ratio is 0.31. This means that the measured relaxation strains for the annealed Cu coating (Figure 30) could be the result of an unknown combination of the crystal orientations of the 2-3 grains in the sample volume, where even the mismatch strains at the grain boundary could play a significant role. In this situation, the stress state could be significantly different from one test to another.

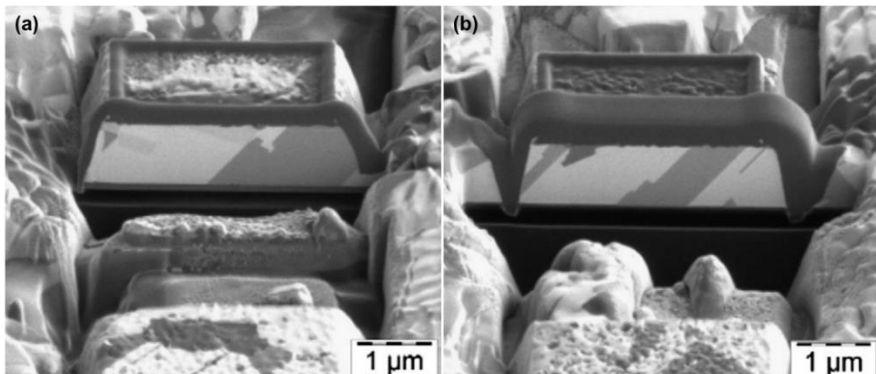
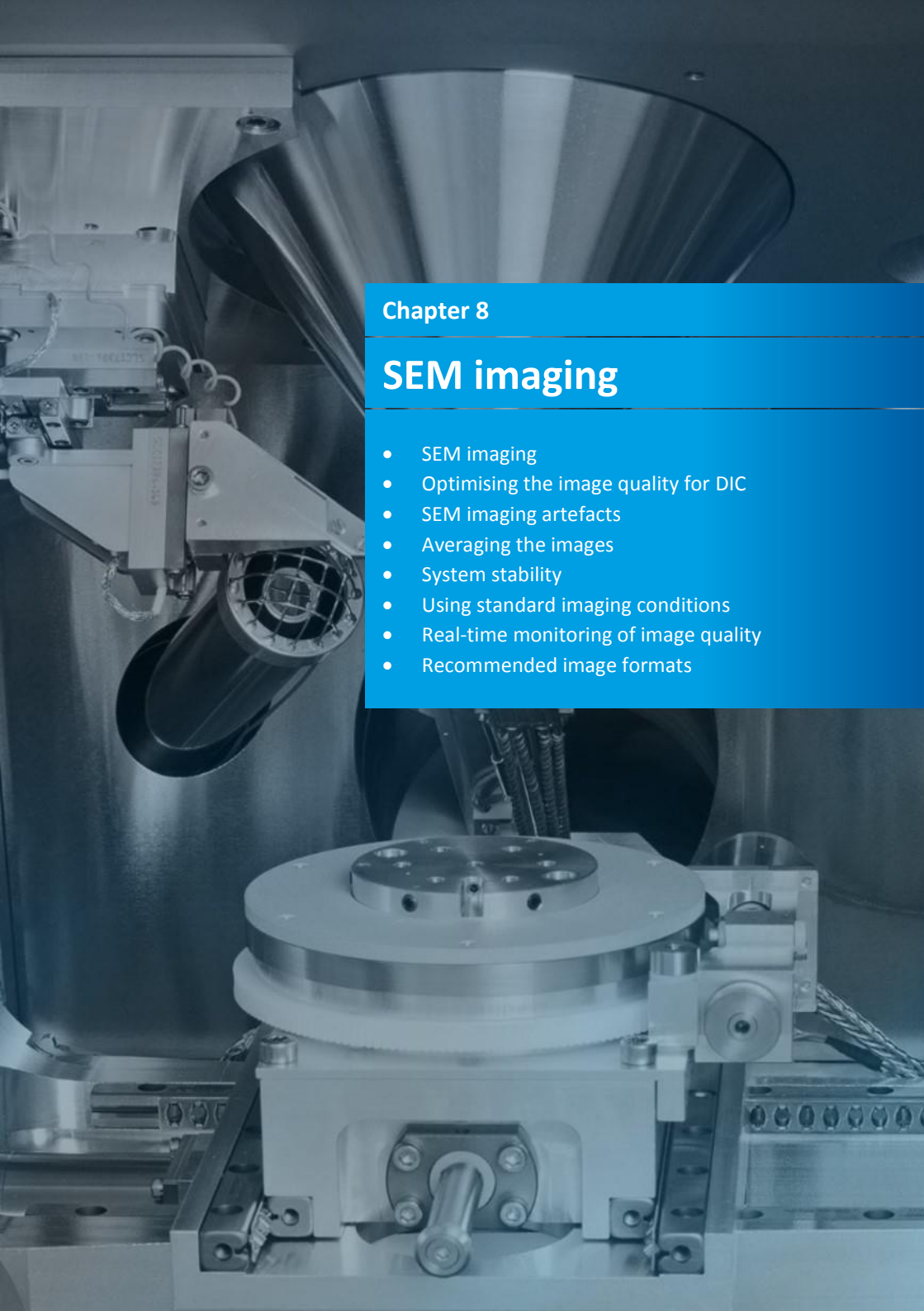


Figure 30. FIB cross sections of tests on annealed (coarse crystalline) copper coatings highlighting different grain orientation [28].

In another study by Salvati et al. [62] three different materials were examined to validate the influence of anisotropy factor on stress determination: a Ni-base super alloy (IN718), single crystal silicon and aluminium alloy with anisotropy factors of 2.83, 1.57 and 1.27 respectively. Results showed that the material with the highest anisotropy factor (IN718) displayed the broadest distribution of stress values. It is important therefore to highlight that care must be taken in the selection of milling geometry for the correct estimation of residual stress

especially in the case of anisotropic materials. For example, Krottenthaler et al. [63] demonstrated that the H-bar geometry allows the calculation of uniaxial relaxation for both isotropic and moderate anisotropic elastic behaviour ($A \leq 3$); but for higher anisotropy ratios, an additional milling step using Four slot milling provides more reliable results.

This page was intentionally left blank.



Chapter 8

SEM imaging

- SEM imaging
- Optimising the image quality for DIC
- SEM imaging artefacts
- Averaging the images
- System stability
- Using standard imaging conditions
- Real-time monitoring of image quality
- Recommended image formats

SEM imaging

The quality of the captured SEM images is of vital importance to obtain the best stress results with lowest uncertainty and this chapter covers a number of ways that image quality can be optimised and checks for ensuring that the FIB-SEM system is performing well. **Prior to any experiment the instrument stability and performance should be checked and if necessary a series of quick measurements carried out to avoid carrying out a full set of measurements that cannot be subsequently analysed satisfactorily.** This could include checking the quality of the images in terms of noise levels, sharpness and contrast and brightness. Simple DIC checks can be made on subsequent images to check that images have not degraded or drifted and that the DIC code can analyse them without error. It is appreciated that many FIB-SEM instruments are in shared facilities with multiple users and many projects, and while ideally the instrument should be set up for FIB-DIC only, **the multiuse nature of these instruments mean that checks are essential to ensure that the system is operating to its full capability prior to use.**

Optimising the image quality for DIC

For DIC analysis the best looking highest-contrast image is not always necessary but as a minimum it must contain sufficient detail and be consistent with other images in the same experiment. It is important to avoid highlights, have a reasonable contrast range, and most importantly be low noise. Figure 31 shows representative images of reference samples imaged by the different partners and FIB-SEM systems within the iSTRESS project. These images were of a random pattern of Pt dots (30 nm in diameter, on average) on a silicon wafer and exhibit a range of contrast and brightness levels with some significantly less sharp and some exhibiting significant beam astigmatism. The variation in quality, noise and resolution from the different FIB systems and different levels of operator skill is clear, but it was still possible to carry out DIC analysis in all cases providing there was consistency between subsequent images.

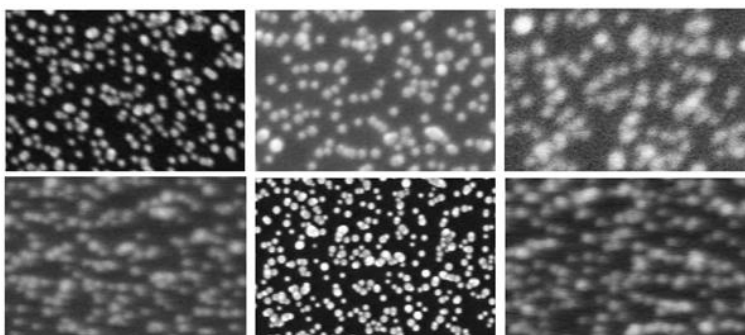


Figure 31. Representative images of the 30 nm Pt dots on silicon reference samples showing the variation in quality, noise and resolution from different FIB-SEM systems and operator skill.

Despite the apparent tolerance of the DIC software, **it is still good practice to obtain the best images possible on the instrument for a given sample**. This may involve experimenting with accelerating voltage, spot-size, and image capture conditions for different samples, but once ideal conditions are found they should be kept identical for all images in the same experiment.

SEM imaging artefacts

DIC can be applied to a range of different image sets and scales. Traditionally it has been most often used to measure macroscopic strain and displacement fields in materials testing using conventional macroscopic charge-coupled device (CCD) cameras and lenses, typically imaging small samples in test machines. The scope and scale is limitless, but of interest in this work is the application of DIC on images taken from the FIB-SEM. Because of how these images are generated errors and artefacts can be introduced that affect the DIC processing and must be taken into account. The papers by Sutton [64, 65], and Mansilla [66] and co-workers give good background to the problem. Representative images from tests carried out in the iSTRESS project, showing some of the artefacts in the DIC displacement fields are given in Figure 32.

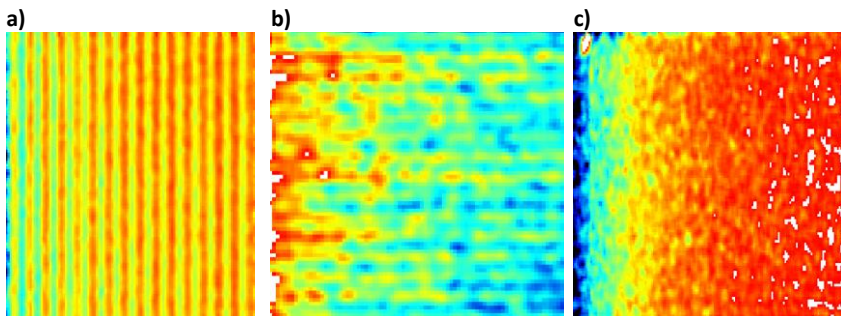


Figure 32. Examples of SEM artefacts in the DIC displacement fields.

Mansilla et al. [66] developed various criteria based on the ratio of the standard deviations of the displacements in the rows and columns of the SEM image, and other self-correlation parameters to rank the performance of a range of SEM imaging systems, and **users are recommended to examine their own setups being used for the FIB-DIC process using a similar approach, particularly when high precision measurements are to be made**.

The problems are caused by how the SEM images are generated. The imaging process in the SEM steers an electron beam across the sample in an x, y raster pattern, and the beam pauses at each x, y position. A signal is collected from a number of possible detector types and the intensity of the signal is then assigned to the corresponding x, y position in the digital image.

At low magnifications the beam covers the widest solid angle and the lenses are required to deflect the beam by producing a large swing in magnetic field. At these magnifications there

are distortions at the edge of the image, where the beam has had to travel furthest, compared to the centre where the deflection is zero. The result is that a DIC image from a rigid translation of the sample will show rotational displacements in a circular pattern, increasing with distance from the centre.

At high magnifications where the beam is deflected the least, the distortions are less a result of imperfections in the magnetic lenses, but more likely due to errors in the way that the x , y raster pattern is generated. In a digital SEM, the x and y positions in the scan are generated by a fast digital to analogue converter (DAC), which generates an analogue voltage corresponding to the position in the microscope. The DAC is never perfectly linear and depending on the type of converter may have imperfections which can give rise to a ramp that while overall may appear linear will contain small errors that give rise to pixel positions that are not equi-spaced.

This is a common cause of vertical and horizontal banding in SEM DIC results and is probably the type of artefact most often seen (Figure 32a,b). It may depend on the internals of the SEM scan generator, but typically the position and number of bands will not be affected by magnification or scan rate, only the number of pixels in the image. The intensity of the banding will be reduced depending on the size of the image shift and can be affected by the DIC processing conditions. Banding in DIC images is most pronounced when small DIC windows are used; and can be reduced to a large extent by suitable choice of DIC parameters. Figure 33 below shows the DIC displacement field generated from the same SEM pair of images using different DIC window sizes – effectively changing the resolution of the displacement field. Interpolation has been used in this case to provide pixel level displacement data, but the effect of using a larger DIC window is to suppress some of the artefacts (vertical banding in this case). It is important to realise that Some FIB-SEM systems are more prone to these artefacts and whilst changing the DIC parameters may suppress them they are still present. They also tend to be more visible in higher resolution images. **Fortunately the magnitude of the displacement artefacts associated with banding are small compared to the displacements generated from strain relief and milling, so even if they are still present their influence is small.**

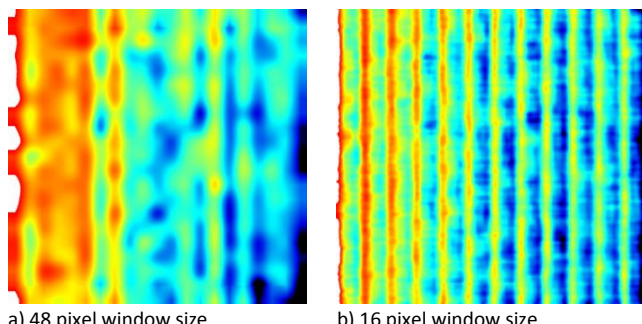


Figure 33. Effect of different DIC parameters on the displacement field and artefacts.

Another related distortion is dependent on the flyback of the beam in the SEM. The ramp for an SEM is a sawtooth, so if the ramp is 0 to 10 V, at the end of a line the voltage is at 10 V and must then immediately get back 0 V to get to the beginning of the raster. This means the DAC and all the subsequent amplifiers in the SEM involved in generating the ramp must be able to cope with this slew rate. Most SEM's already allow a settling time to mitigate this, but when examined at the sub-pixel level using DIC it appears that the pixel spacing at the beginning of a line is smaller than at the end of the line. This is characterised by a roll-off in image shift at the beginning of a line in the x direction (Figure 32c). This roll-off increases with increasing scan speed, and can be mitigated by increasing the settling time at the beginning, sometimes called the front porch. This effect is only seen in the x direction, as the raster in the y direction is orders of magnitude slower.

A third common form of distortion in the SEM is a result of mains interference. This manifests itself in DIC images as diagonal stripes across an image. The frequency of these lines will change with scan speed and will often be exacerbated by introducing mains frequency signals into the SEM chamber by poorly designed electrical feedthroughs for example.

The simplest way to examine the effects of image distortions on DIC results is to look at the results of simple translations of the sample with respect to the camera. If a sample is moved by 20 pixels in the x direction, then with a perfect camera the result of the DIC x shift will be a shift of 20 pixels for every image point. If the camera now has a defect at the 41st x position such that for each row the pixel spacing is actually 39, 40, 40.5, 42, 43 etc. and the same 20 pixel shift is performed then the result will be different. The image that in the first image was at 40, 40.5, and 42 will now be at 60, 61, 62 so will register as a 20.5 pixel shift. Additionally the pixels at position 40, 40.5, 42 in the second image will be matched to the pixels at 20, 21 and 22 from the first image, thus registering a 19.5 pixel shift. The result now is that rather than registering a 20 pixel shift for every point there will be two bands spaced 20 pixels apart, one at 19.5 shift and one at 20.

These artefacts are not particularly relevant for normal FIB operations or SEM imaging, but are a feature of DIC processing when small sub-pixel displacements are being measured and even small imperfections in the images will be highlighted. The fundamental principle behind the DIC technique is that the images used have equi-spaced pixels, and indeed the information contained in the common file formats is the x , y raster position as an integer and the intensity integer or real, at this point. There may be some associated metadata indicating what the integer raster position represents as a real value, but it is assumed the pixels are equi-spaced and there is no scope to account for any distortions. In optical imaging the camera lenses are the most likely source of distortion, but there could also be imperfections in the manufacture of the CCD chip itself. The image generation method in the digital SEM is fundamentally different but there are still several camera/lens distortions which can result in non equi-spaced pixels.

Averaging the images

To increase the signal to noise level of the images to be processed by the DIC software it is recommended that they are captured with a relatively high frame rate in the range of 0.1 to 0.5 seconds per frame, then either averaged or integrated for at least 16 frames to reduce the noise level but still allowing for image capture in a few seconds per image. To further improve the quality of data, multiple images should be captured at each step and the obtained stress data averaged. Care must be taken to ensure that the sample does not move significantly as this will lead to blurring of the pattern which may introduce artefacts into the DIC calculations.

The example in Figure 34 shows the effect of noise reduction in three different FIB-SEM systems, comparing a single scan (on the left) with the result of averaging 10 frames (right). It is important to note that because DIC operates on the sub-pixel level any reduction in noise is clearly beneficial. The use of slow scan (few seconds or more) single frame captures should also be avoided. While this will in most cases reduce the noise in the image significantly there is also a high probability of small scan-distortions resulting in differences between subsequent images that will give misleading strain data when the images are processed. In samples prone to charging this effect will be significantly greater and the images may be distorted very badly by the slow charge build up from a slow scan whereas faster scanning and frame averaging will reduce this effect considerably.

Averaging can be carried out on the images or following DIC analysis, by averaging the calculated displacement fields. The former approach is probably the preferred option.

Figure 35 shows data from an exercise in the iSTRESS project where partners were asked to carry out DIC processing on four sets of images, from a Ring-core and Double slot milling experiment. For both geometries, 10 repeat images were taken at each milling step, and these were then processed to give a single averaged image. The multiple strain plots in each figure correspond to the strain data calculated by each partner, but it is clear in both instances (comparing Figs 35b,c for the Double slot and Figs 35e,f for the Ring-core) that the effect of averaging is to significantly reduce the scatter in the individual strain profiles. The overall scatter and difference between the profiles is solely due to differences in DIC analysis parameters as each partner analysed the same set of images. This is discussed further in Chapter 9.



Tip – During the milling and imaging process it is recommended that operator interaction with the instrument is kept to a minimum to avoid unnecessary changes which might subsequently affect the quality of images and DIC analysis minimised. The use of magnification lock, sample current monitor to reduce drift is highly recommended.

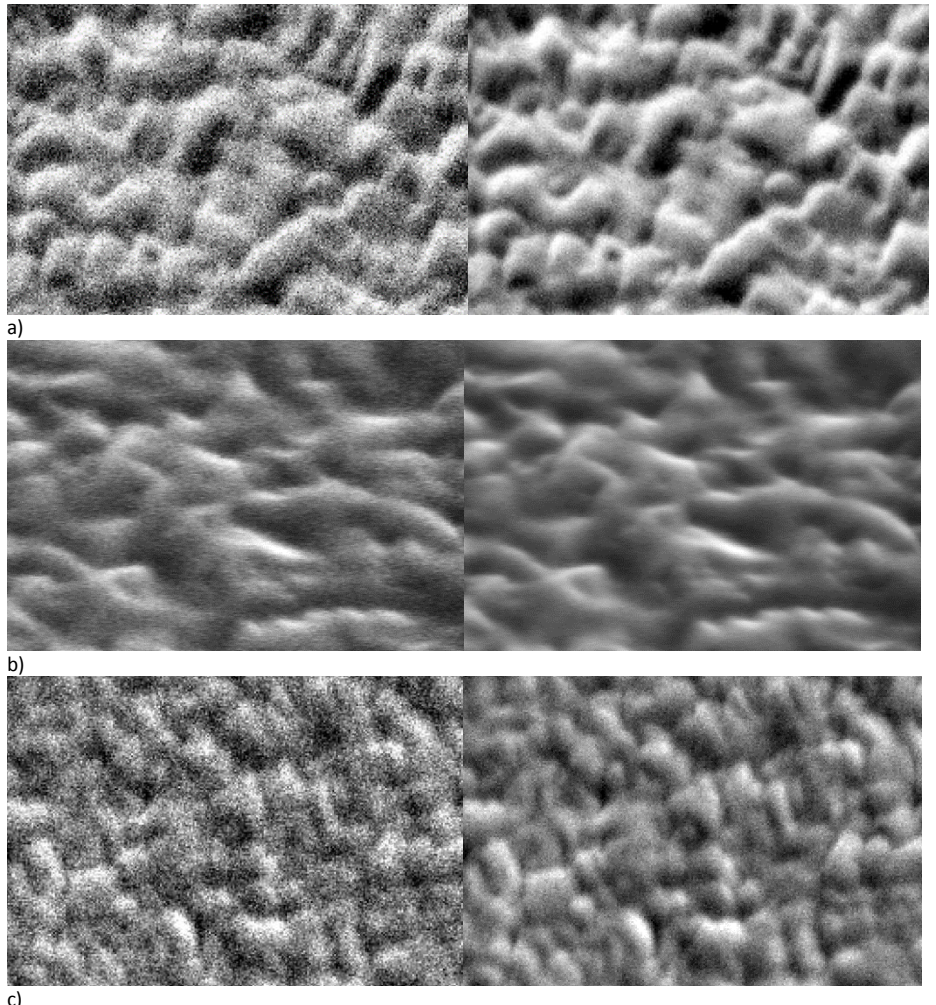
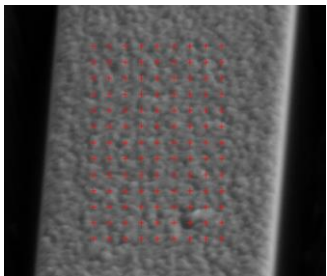
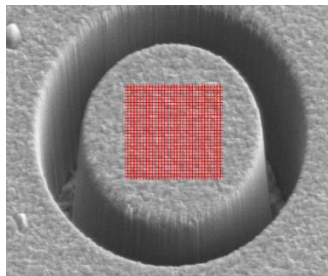


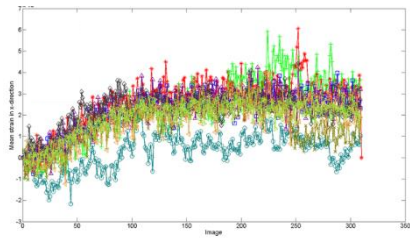
Figure 34. Example of reduced noise through averaging in different iSTRESS partner FIB systems – single images (left), averaged images (right).



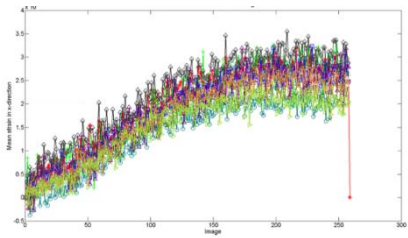
a) Double Slot Image set



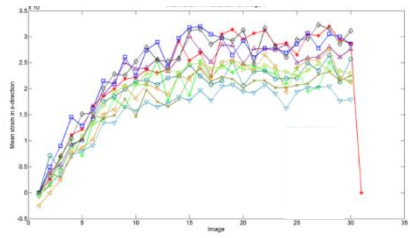
d) Ring-core Image set



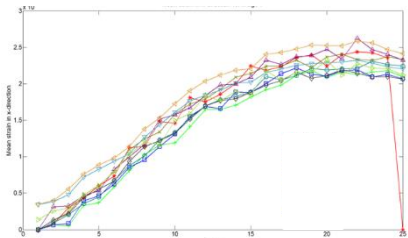
b) Double Slot full dataset (310 images)



e) Ring-core full dataset (260 images)



c) Double slot averaged images (31 images)



f) Ring-core averaged images (26 images)

Figure 35. Comparison of strain relief calculated using individual repeat images and averaged images.

Figure 36 shows DIC derived strain data from a Double slot milled in a TiN coating, where milling was carried out in 18 equal depth increments and 10 images (each consisting of 10 averaged frames) were captured at each increment. The plot shows the early part of the test (first 5 depth increments/50 images) and compares strain data calculated from DIC analysis of the individual images with data from the average of the 10 individual DIC strain data calculations at each step.

If the individual images at each increment were perfectly identical the data in Figure 36a would show a series of distinct steps for each set of 10 images (as seen previously for the DIC

data in Figure 12), but that is not the case in this example indicating that there are small differences between repeat images, probably caused by small beam scan errors (as the pixel size is relatively large compared to the beam spot) which also leads to small natural variations in local contrast and brightness (at the pixel level) between images. The same data is plotted in Figure 36b against depth increment, and the individual strain values calculated from each image shown. This gives an indication of the potential uncertainty in the strain data at each milling depth, because the typical variation in strain at each depth increment (the highlighted red boxes) is of the order 2×10^{-4} . Although this result is specific to this particular test, material, FIB instrument, milling rate, imaging and DIC analysis conditions it is a useful indicator of the potential variation and errors in the strain, if only single images are taken.

It further supports the recommendation that multiple images should be taken at each milling step as even the highest quality single images will have differences due to minor scan variations.

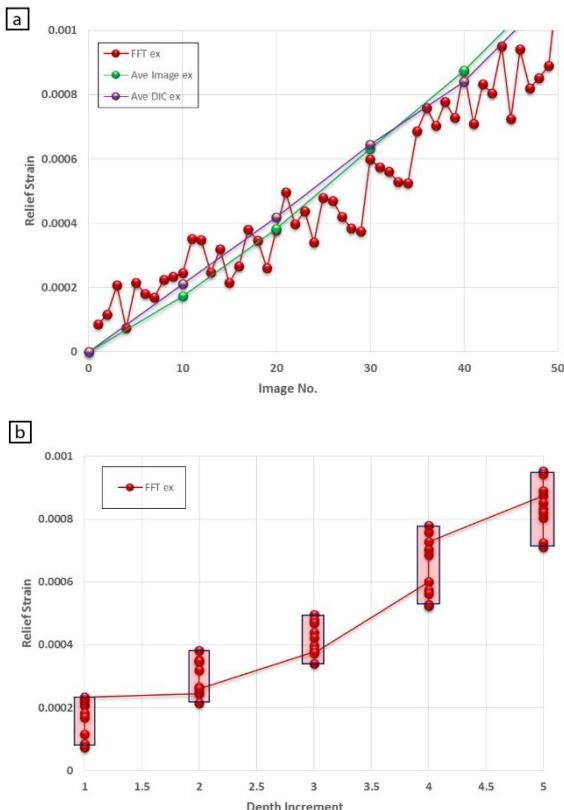


Figure 36. Illustration of the natural variance in calculated strain values for multiple images captured under nominally identical conditions.

Using multiple images at each depth increment is also useful for highlighting potential errors or issues with the process, highlighted by the data in Figure 37, which shows a systematic offset to the strain data calculated from the first image of each set of 10 images. This was caused by an operator-affected change in the SEM imaging mode from live imaging to averaged imaging after each consecutive milling step. It was later found that allowing a sufficient time (of 30 s) for the image to stabilise between the changes in scan-mode alleviated this problem.

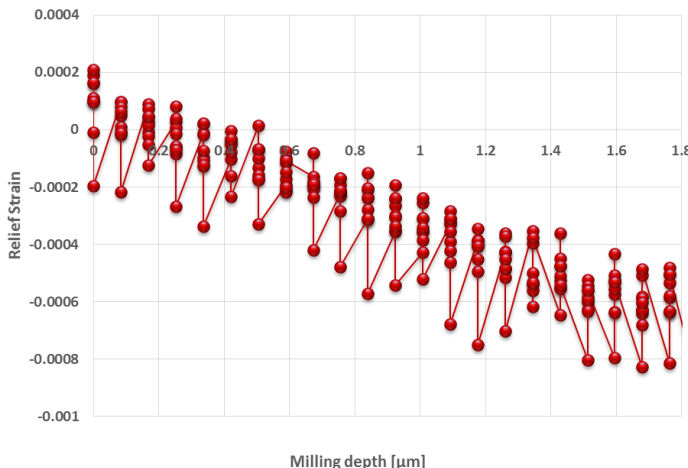


Figure 37. Systematic variation in the calculated strain values during capture of multiple images and spike due to change in SEM image mode.

There are many advantages in capturing multiple images, not least as a backup in case there are problems with some of the individual images, for identifying systematic problems with the instrument or set-up (by identifying changes in the image quality or drift between sets of nominally identical images) and for quantifying potential uncertainty in the analysis, particularly if depth profiling is being carried out and the changes are likely to be small between each step. The main disadvantages are the additional time to capture the images and size of the multiple image files to be analysed, along with extra effort and computational time required carrying out the DIC analysis. There is also the potential for degrading the scanned area by repeatedly imaging the same area in samples prone to contamination issues.

System stability

As multiple images are captured during the FIB-DIC procedure and comparisons made between these images at the sub-pixel level by the DIC software, stability of the instrument is paramount. **One of the main sources of error is caused by physically moving the sample between imaging and milling steps as this highlights the small scan errors that most SEM columns have.** These can manifest as simple stretching or compressing of the image in one or both image directions and include scan errors along individual scan lines and random non-systematic errors, all of which can lead to significant degradation of the strain and displacement data and in extreme cases lead to completely erroneous measurements.

Figure 38 shows an example of the apparent DIC displacement data from a series of tests carried out by the individual iSTRESS partners on a range of FIB systems. In this test, Si wafer samples coated with a Pt dot pattern were imaged in the FIB-SEM under a range of different conditions to examine the FIB performance and stability. The displacement data in Figure 38 shows the results from tests where DIC was carried out on sets of 10 repeat images, taken at the start and after holding in position (with no stage movement or auto tracking) for 2, 5, 10 and 20 minutes respectively.

Figure 38a shows the DIC displacement data comparing the original set of images with those after a dwell of 20 minutes. In ideal cases there should be a small level of random noise, with no defined structure. This is clearly not the case with many of the instruments as “banding” and “edge effects” are clearly evident. Figure 38b plots the corresponding average displacement throughout the test for each partner. Five discrete sets of images were taken, and the data clearly highlights the relative performance and stability of the different machines. This is important as it will have an influence on the accuracy of the subsequent DIC data during milling.

It is generally best practice, for minimising scan errors, to keep the sample in a fixed position for the whole of the analysis including both ion milling and imaging steps. This generally means that the sample will be tilted towards the ion column so that ion milling is carried out with the ion beam orthogonal to the sample surface and the SEM is imaging with the sample tilted. With the sample in a fixed position and no further movement, any drift caused by the relaxation of the stage will be minimised, with a corresponding reduction in detectable scan errors. If imaging is carried out with the sample tilted it is advisable to use tilt correction for the SEM, but it should be remembered that the correction assumes the sample is flat and the surface was perpendicular to the stage when mounted in the instrument. In the case of the Ring-core geometry successful application of tilt correction will show the milled geometry as circular in the SEM image. **For the Double and Single slot geometries it is preferable to have the slots running from top to bottom of the image,** i.e. the strain relief will occur perpendicular to the direction of tilt correction and if in error will not have any effect on the final result.

The image field of view (and magnification) depends to a large extent on the milling geometry and the performance of the FIB-SEM, particularly related to stability or drift. Many FIB instruments have automatic drift correction, based on tracking a fiducial mark in a corner of the image away from the area that is being milled, and this was implemented in some of the iSTRESS partner systems. **If image drift is perceived to be a problem, an alternative is to use a slightly wider field of view, to ensure that the area over which the DIC is to be carried out remains within the field of view throughout milling process.** The magnification should be chosen to maximise the area of interest for the DIC analysis taking into account likely image drift or stage drift over the time taken to perform all the milling steps. If too low a magnification is used and the milled geometry only covers a small part of the image, then there is likely to be a drop in resolution and accuracy.

Further potential problems can be caused by changes in contrast and brightness over time and this is often seen as a continual degradation in brightness and image quality as more images are captured. This is often attributed to a contaminated sample and to reduce this the sample should be cleaned by the methods described in earlier sections if practical. In cases where the sample cannot be cleaned it may be possible to use the instrument auto contrast and brightness functions but these are often not totally consistent and can cause problems for DIC analysis.

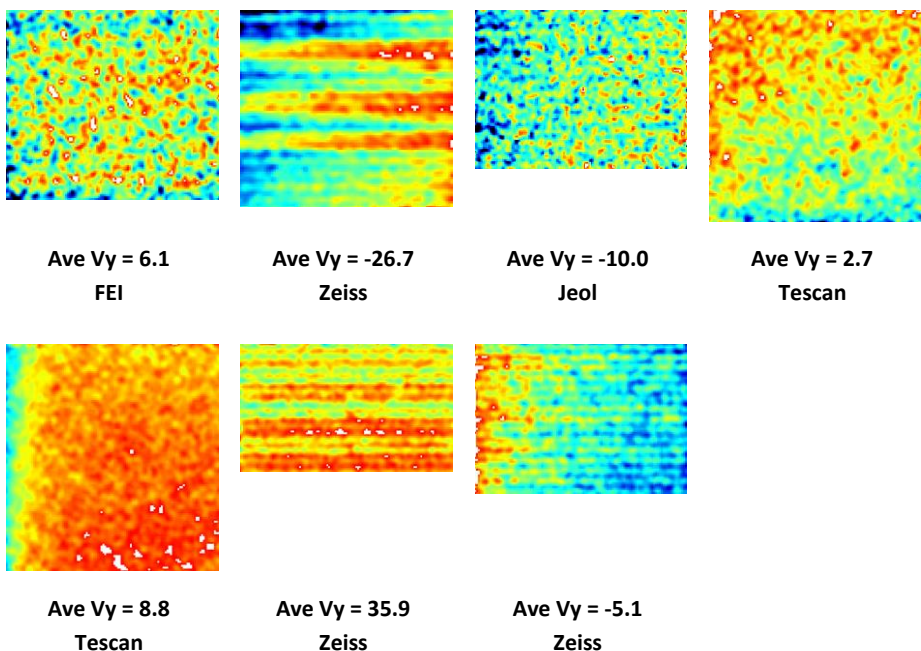


Figure 38a. DIC displacement fields after a dwell of 20 minutes.

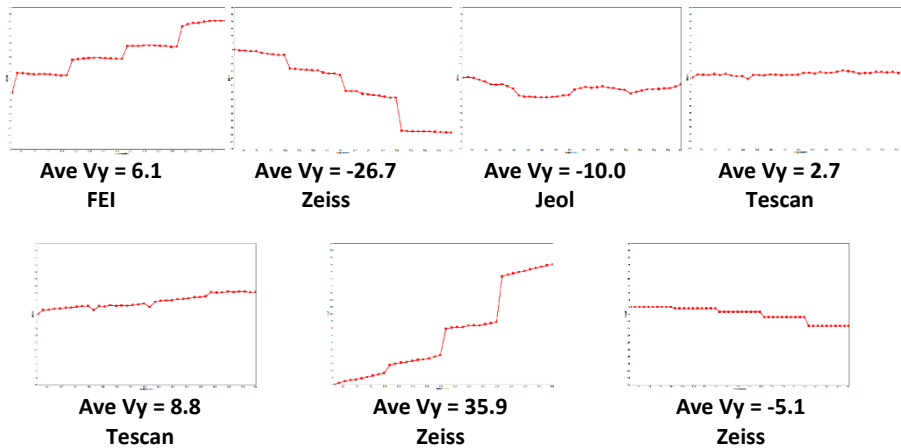


Figure 38b. Average DIC displacement data showing the variation with dwell time (2, 5, 10 and 20 minutes).

Using standard imaging conditions

It is recommended that wherever possible standard imaging conditions such as resolution, frame scan speed, frames averaging and if possible contrast and brightness are used for tests on the same material, but this does not always guarantee that the images will be ideal or that they will be error free due to the previously highlighted issues. However, maintaining as much consistency as possible should guarantee the best possible outcome for the particular sample.

Contrast and brightness settings will of course be the most sample specific variable and may also change with modification of the SEM accelerating voltage. **The user should aim to use the full grey scale available without any saturation of the image. As previously stated frame integration or averaging should be used, with a fast frame speed and at least 16 scans.**

For the vast majority of samples imaging with an image width of 1024 pixels (or nearest machine specific equivalent) gives the best compromise between resolution and speed.

Although most FIB-SEM systems will now allow much higher resolution images to be captured there is little benefit in using image resolutions above ~ 1000 pixels as the computation time for the subsequent DIC can be extended greatly by high resolution images for little or no gain in actual stress resolution and the storage requirements for the significantly larger images file sizes may also be prohibitive.

Real-time monitoring of image quality

If possible, **the ability to carry out some real-time monitoring of the SEM image quality is recommended** as it can reduce the likelihood of a failed experiment, particularly if the results show that the subsequent images and data are unsuitable for DIC processing. Even if the capability for real-time monitoring is not available, it is still recommended to do a quick test by capturing a set of images and carrying out a quick assessment of their suitability using DIC. Subject to the DIC results the full milling experiment can then begin.

Real-time monitoring was implemented in the DIC software developed in the iSTRESS project, based on analysing the correlation coefficient of the current image with that of the original “reference” image to see if significant degradation of the image had occurred. **Other criteria could be used, based on noise levels, brightness, contrast, drift etc. but all are designed to avoid wasting time and effort making measurements that cannot be subsequently analysed.**

Recommended image formats

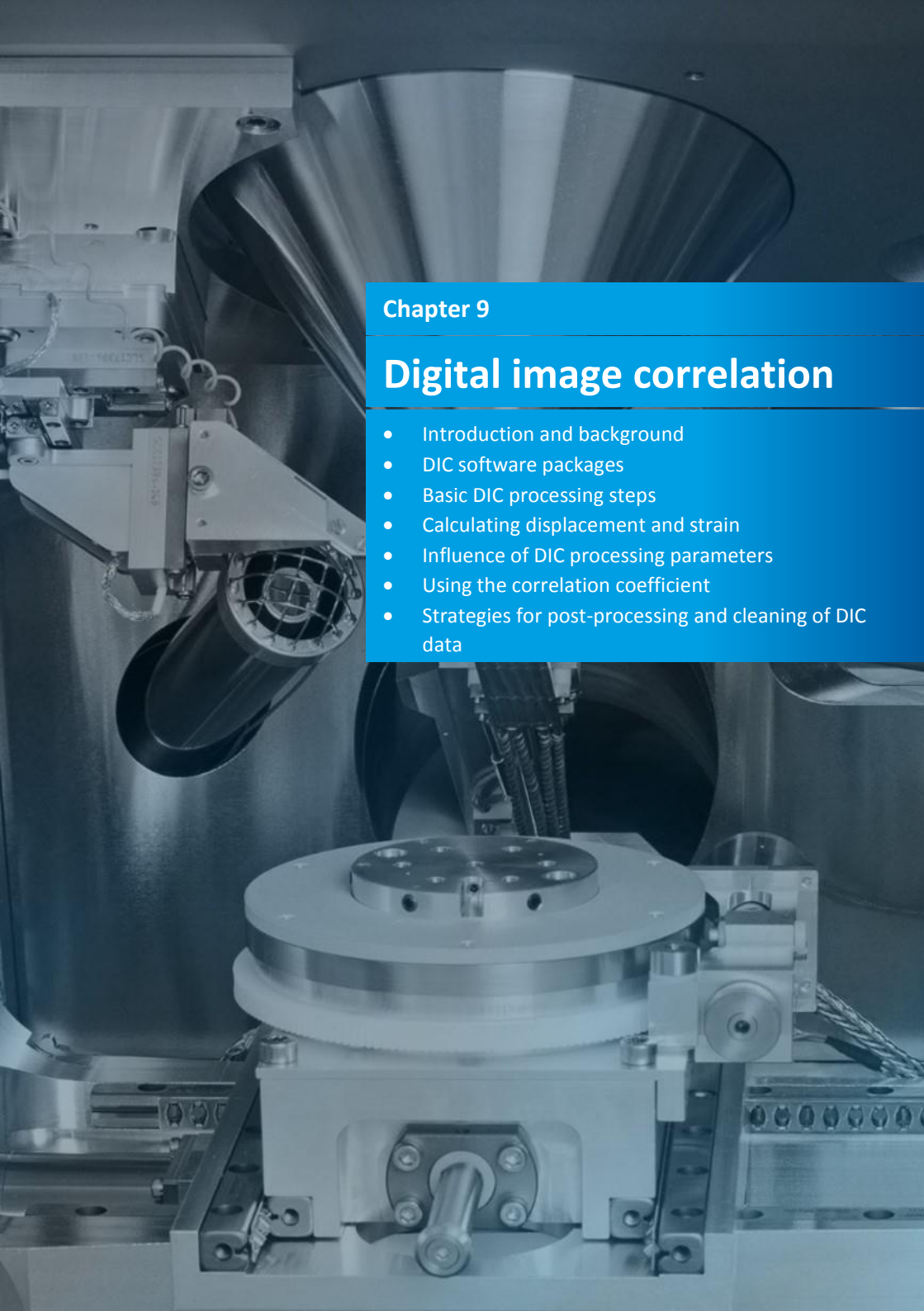
Images should be saved as uncompressed 8-bit TIFFs or bitmaps. Some instruments can save images in 16-bit format but some of the DIC and image analysis software cannot handle this format, and the 8-bit monochrome images generally have sufficient grey scale levels (256) for reliable DIC. **Capturing good quality, stable images is probably more important.**

Typically an 8-bit TIFF image of resolution 1024 x 768 pixels could be 1 MB in size so it is possible, where multiple image sets are being saved at a number of depth increments, to very quickly generate a set of 300-400 MB images from a single test.

Files should be named and numbered appropriately and saved complete with the Metadata or EXIF data, which can be accessed if necessary to check the instrument and imaging settings through a suitable text viewer, web browser plug-in or image editing software.

Care should be taken in importing the images into the DIC software to ensure that the image order is correct. Some of the DIC software packages will automatically order the images alpha-numerically and can be confused if there is not a consistent and sensible numbering.

If possible it is good practice to check the image sequence before DIC processing is carried out and users are also advised to backup and save test data and image files on a separate hard disc or different computer.



Chapter 9

Digital image correlation

- Introduction and background
- DIC software packages
- Basic DIC processing steps
- Calculating displacement and strain
- Influence of DIC processing parameters
- Using the correlation coefficient
- Strategies for post-processing and cleaning of DIC data

Introduction and background

DIC is a full field non-contact strain measurement technique that was first developed in the 1980s [67, 68], and has seen significant development and uptake in recent years due to the availability of high resolution cameras and increased computing power. It is a versatile tool, and is being used extensively in a wide range of applications including the characterisation of material behaviour, mapping the evolution and distribution of strain fields around features and defects, crack tip and crack propagation studies, dynamic vibration analysis, high temperature strain mapping, structural health monitoring and FE model validation. A key reference and a good starting point for the reader is the book published by Sutton and colleagues [69]. Most of the applications of DIC have been on the macro scale but recent developments, including those relevant to the current application, have seen the focus extend to micro-scale measurements, using DIC to monitor images and tests carried out in the optical microscopes and the SEM.

DIC works by comparing images of a sample or component at different stages of deformation and tracking blocks of pixels to measure surface displacements relative to a reference state and image to build up full field 2D and 3D vector fields and strain maps. The position of the centre of the pixel blocks is determined to sub-pixel accuracy over the whole image using sophisticated correlation functions, from which the vector and strain components can be calculated. Different DIC analyses have been developed to obtain sub-pixel resolution based on non-linear optimisation techniques, intensity interpolation, Fourier transform analyses, Newton-Raphson iteration methods, least squares matching, genetic algorithms and neural networks [70]. The particular correlation analysis will often depend on the DIC software package used, but **in most cases the typical resolution for 2D DIC is ~0.01 pixel or better for displacement, although practical factors associated with the experimental setup, including the image resolution and quality and the DIC calculations themselves may affect the ultimate accuracy and resolution.** It should be noted also that some of the DIC terminology is software and user specific. Examples include the terms “blocks, subsets, windows, facets” all relate to the pixel area over which the correlation is carried out.

Successful implementation of DIC requires images with a random, stochastic pattern and a reference image against which all the measurements are made – and this still applies in the FIB-DIC technique. In some cases the texture and structure of the material examined in the SEM will be sufficient for DIC, but often some form of pattern will have to be applied (see Chapter 5); the reference images are usually those taken before milling has started. Where possible the process should be automated and have minimal operator intervention, using the same processing parameters for each setup providing the milling geometry, field of view, image resolution is the same.

Considerable work has been carried out to optimise the imaging conditions, the accuracy of DIC measurements and to compare the stability and accuracy of the different FIB-SEM systems

used within the iSTRESS project. Specific issues relevant to the optimisation of the FIB-DIC processing are discussed in the following sections.

DIC software packages

A number of commercial DIC software packages are available for analysing the SEM images, including those supplied by Correlated Solutions, LaVision, Dantec, GOM, Match-ID and Imetrum. This is not an exhaustive list, and proprietary in house systems such as the VEDDAC software developed by the Fraunhofer Institutions and the iSTRESS DIC software which has been specifically designed to analyse images from the FIB-DIC experiments are also available, together with various other freeware or Matlab-based codes.

The DIC software developed within the iSTRESS project is available to download from the iSTRESS website at <http://www.stm.uniroma3.it/iSTRESS>, and a list of other relevant DIC software websites is given at the end of the guide.

It is recommended that users become familiar with the software they are using, and optimise the DIC processing conditions for the images produced by their particular FIB-SEM system. Where possible, validation of the DIC processing conditions is recommended by using reference image sets or experimental setups with known levels of displacement or strain. A good source of images for validation of DIC software is the SEM DIC Challenge website [71] (<https://sem.org/dic-challenge/>) where a range of image sets are available, designed to validate and optimise the results from the DIC analysis. Whilst not specifically using images on the scale of those produced in the FIB-DIC experiments, it is nevertheless a useful source for validating software and investigating the effect of DIC processing conditions on the calculated displacement and strain fields.



Tip – Users should be familiar with DIC software and have a good understanding of the relationships between DIC settings/parameters and the measurement problem, field of view, required accuracy and resolution. It is very easy to select different options and DIC parameters during the processing stage which can adversely affect the quality and reliability of the results.

Figure 39 shows an image and representative displacement data in the x and y directions obtained from the DIC analysis of the SEM Challenge “High Contrast Set” where the image set was created by numerically binning a 14-megapixel image to supply 122 subpixel shifted images including the reference images with 0.1 pixel shifts from 0 to 1 pixel in both the x and y directions [71]. The average displacement data over the central section of the image (bounded by the red rectangle in Figure 39b) is plotted against image number.

A series of analyses were performed using a range of DIC processing conditions. Results showed that **for this dataset** there was little significant difference between results using

different window sizes. With a field of view of ~300 pixels, the typical mean difference of 0.003 pixels could contribute to an error which appears as an apparent strain of 1×10^{-5} . This is likely to be a lower bound on the total error as in practice, the measurements will also be affected by non-uniformity of displacement and strain in the field of view, the area over which the strain is averaged, variable imaging conditions and other artefacts.

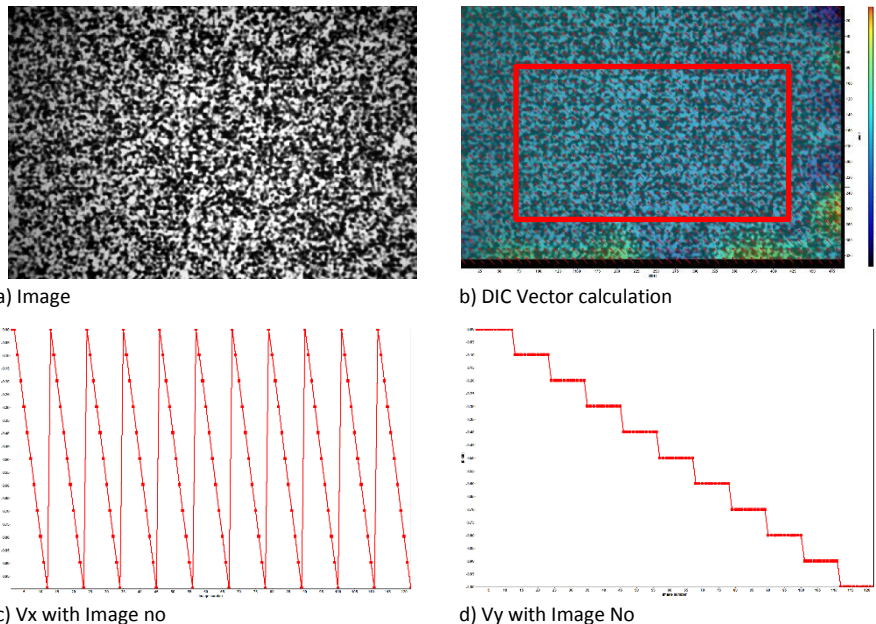


Figure 39. Representative Images and data from DIC analysis of the SEM Challenge (High Contrast image set) to validate the DIC software and processing conditions.

Basic DIC processing steps

The flowchart below illustrates the basic processing steps that should be taken when carrying out DIC analysis of the FIB-SEM images. Depending on the specific DIC software package used some of the steps will vary, but the basic concepts and flow of the analysis have been developed to provide a consistent approach that should give reliable results.

The exact DIC settings will depend to some extent on the actual software, the FIB-SEM system and imaging conditions used, and should be investigated by a series of initial trials (using the reference samples for example). These optimised settings can then be used in subsequent tests to reduce errors and uncertainties associated with varying the DIC processing conditions.

DIC Analysis Flowchart/Processing Steps

At this stage it is assumed that the images have already been captured during the FIB-DIC milling experiment, and any relevant checks on image quality and suitability for DIC measurements have been carried out.

- Order and renumber the images and import them into the DIC analysis software, using a separate folder for each test
 - Check the histograms, noise levels, sharpness, brightness and contrast
 - **Only if absolutely necessary** – adjust all images using the same settings to give a consistent image set
 - **Average the images** if multiple images have been taken to reduce noise and improve the S/N ratio
 - If appropriate carry out Image registration to remove drift and rigid body motion
 - Identify the “Reference image” against which subsequent DIC measurements will be made
-
- Agree a strategy to process the image set relative to the original reference image, or a different image
 - Carry out DIC processing – using “Standard and optimised DIC conditions”
 - Calculate Full field displacement data – V_x, V_y *
 - Examine DIC displacement data over the gauge volume of the chosen milling geometry for consistency – if necessary reprocess using different DIC settings (e.g. window size or different reference image)
 - Check correlation coefficients (Chapter 9)
 - Examine the displacement fields to identify the area identified from the FE model AND unaffected by milling artefacts and edge effects
 - Extract or calculate Full field strain data - ϵ_x, ϵ_y *
 - If appropriate export data/displacement data into other software to calculate strain data
-
- Post processing and cleaning of data as appropriate
 - Plot the variation of strain relief with depth/Image number
 - Fit data to predicted relief profile to obtain strain at full relief for the milling geometry used
 - Calculate Residual stresses (see Chapter 11)
 - Estimate uncertainties (Chapter 13)
 - Report results (Chapter 14)

* And other orientations depending on the requirements and milling geometry used



Tip – It is important to use a reliable and good quality image editor software – e.g. ImageJ or MATLAB – to make sure artefacts and errors are not introduced

Calculating displacement and strain

Most DIC software will calculate displacement maps, and these are convenient, particularly for validation of FE and for calculating strains based on the slope of the displacement field.

It is often also possible to extract the strain components directly from the DIC, but users should be aware of the potential limitations and give careful consideration to how the strain is calculated, particularly with regard to the effective “gauge length” over which the strain is calculated, the uncertainties associated with small DIC windows, and the assumption and reality of uniform strain within the area of interest.

Displacement is a basic DIC output, and should be used for checking the suitability of the DIC processing conditions and for validation and comparison with FE models. In most cases the DIC software will calculate a single displacement vector for each DIC window or subset and interpolation is then required to generate the displacement field at the pixel level.

Some DIC software algorithms have problems handling images that have large rigid body motion, as has been observed in some of the milling experiments carried out within the iSTRESS project. This might be a consequence of stage movement or image drift, and if the movement is sufficiently large (particularly compared to the DIC window size) the DIC analysis might breakdown. In many cases this can be overcome by performing some form of “image registration” about a fixed point in the image so that the effective rigid body motion is reduced. It should also be recognised that the images taken in the FIB-SEM are 2D, so the user should be aware that there may be errors in the calculated displacement fields caused by out of plane displacements that cannot readily be accounted for.



Tip – It is important to check the displacement field to ensure that the DIC processing has been carried out successfully, particularly over the area of the image from which the displacements and strains are being used for the residual stress calculations.

Strain can be calculated directly from DIC or external software from DIC displacement data. In the FIB-DIC process the focus is on the magnitude of strain relieved as a consequence of removing material by milling – and this is then used for calculating the residual stress.

The data and images in Figure 40 compare different approaches to calculating strain during the milling of a Double slot geometry in a TiN film. Milling was carried out in 30 discrete steps and 10 repeat images captured at each stage; DIC processing used an effective DIC window size of 12 x 12 pixels. The insert shows the DIC displacement field at the end of milling.

Superimposed on this is the red rectangle, which shows the area over which the average strain has been calculated directly from the DIC derived strain data, and a green line showing the gauge length (approx. 500 pixels) over which the strain has been calculated using the slope of the displacement data. Figure 40a shows how the slope of the displacement data changes during milling, and these have been plotted in Figure 40b together with the average DIC strain data calculated within the red rectangle.

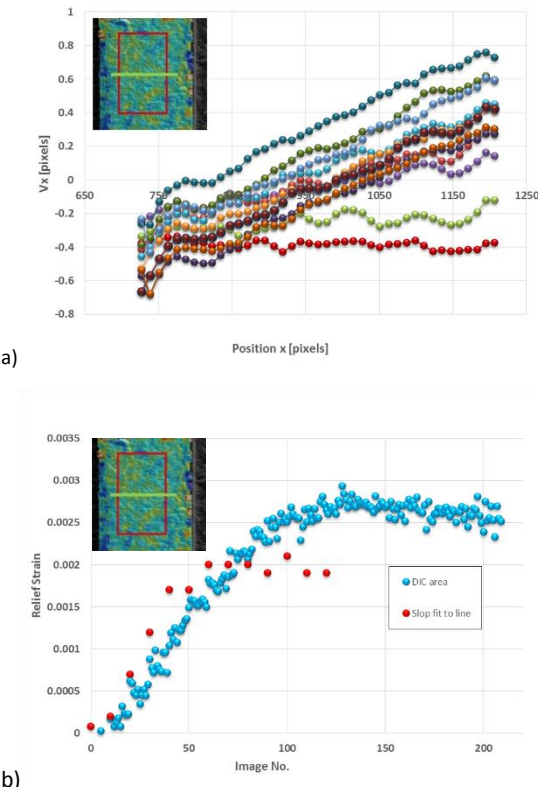


Figure 40. Example showing the different approaches for measuring strain.

Initially there is good agreement, but the saturation relief strain at full depth is lower from the slope measurements and shows more scatter. This is due largely to the greater uncertainty from analysing a line of DIC displacement data rather than an area. **It is recommended, therefore, that the strains are calculated over an area rather than single line of pixel blocks, as detailed in the iSTRESS geometries in Chapter 7 and Figure 29.**

It is also important to examine the DIC displacement field and strain map and report how the strain has been calculated. The assumption in most cases is that the strain is constant and

does not vary along the gauge length or within the gauge volume, but if it does this will lead to errors in the calculated values. And, although FE models of the FIB milling geometry can be used to identify the area over which the displacement and strain fields are uniform or known, care should be taken in assuming that this is true in practice. More details and advice on this are included in Chapter 10 (modelling), but in many cases with FIB milling there are practical factors that mean this is not the case. This is particularly true close to the boundaries of the milled geometry, where artefacts caused by the drift of the milling beam and redeposition might degrade the pattern and affect the accuracy of the milled geometry itself. Figure 41 shows an example of a Double slot milled geometry, highlighting the change in the shape of the milled profile and pattern, and in Figure 41c and d, changes in the overall image quality and degradation of the pattern close to the boundary.

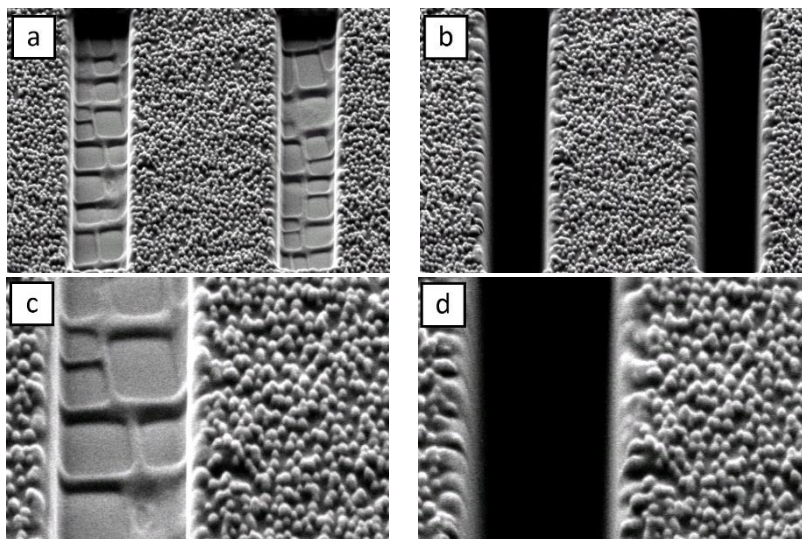


Figure 41. Example of the changes in milling geometry and edge/pattern degradation during milling.

It is useful also to examine the displacement maps to help identify the area for DIC analysis. The displacement field usually break down when there are significant changes to the image or pattern and this also helps to identify the extent of FIB damage and a “stable region” where the DIC data is likely to be reliable and unaffected by milling artefacts and drift etc. The images can also be analysed using edge detection algorithms to identify the limits of the milled geometry, but this will not readily identify the area of the gauge volume that has been affected.

Influence of DIC processing parameters

The different DIC software packages available vary in the level of complexity and user interaction; some are effectively “black box” solutions which allow little user input whilst others permit extensive user selection of the DIC processing parameters. **Irrespective of the software being used it is imperative that the user has a good and solid knowledge of the impact of the DIC processing conditions on the accuracy of the subsequent displacement and strain calculations.**

Amongst the most important parameters that affect the DIC calculation are the DIC subset or window size, correlation and strain calculation algorithms, how the software deals with rigid body motion, selection of the appropriate images used for the “reference” against which all the DIC processing is carried out, and strategies for filtering and post processing data. These are considered in the following sections.

Effect of DIC window size

The images in Figure 42 show the effect of different DIC window sizes on the calculated displacement field. In this case the individual vectors show are associated with a block of pixels (over which the displacement is assumed constant). As used previously, the images are the “High contrast set” from the SEM DIC Challenge website, which show displacements in x and y , and the DIC maps show the displacement fields calculated at step 60. The effect of using a smaller DIC window is to increase the spatial resolution, but at the expense of strain resolution. In this example the effect is not as pronounced as the image set is good quality and the displacement fields designed to be uniform, **but the consequences will be more significant if the strain field varies.**

Some compromise is often required between using a small interrogation windows (high spatial resolution, but low strain accuracy) and larger interrogation window (low spatial accuracy, but high strain accuracy). A big advantage of DIC, however, is that once the images have been captured they can be reanalysed with different parameters to get both sets of information. **It is recommended that the user experiment with different settings to optimise the conditions for their own set up, image resolution and DIC software. The same settings and optimal conditions can then be used for all subsequent tests.**

Table 2 shows the effect of DIC window (subset) size on the accuracy of the displacement and strain calculations. These are the theoretical values based on the correlation analysis and sub-pixel interpolation. In practice the accuracy is likely to be reduced because of the influence of practical factors such as noise, lens distortion, lighting changes etc.

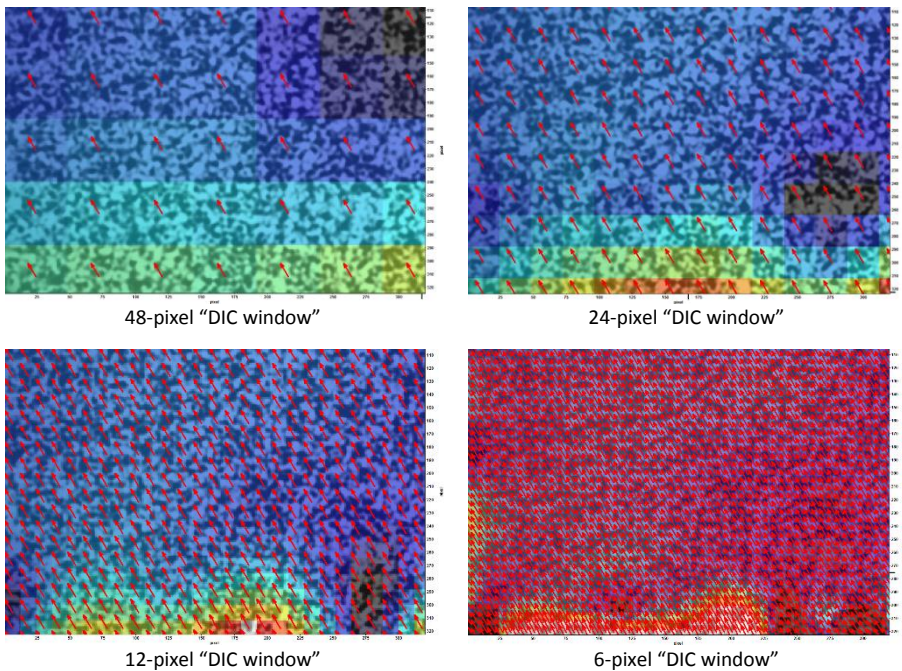


Figure 42. Variation in displacement field with different DIC pixel blocks/windows (SEM Challenge High Contrast Image Set [71], analysed using the LaVision Davis software).

Size of DIC window (pixels)	Accuracy of calculated vectors	Accuracy of calculated strain values
128 x 128	0.01 to 0.03 pixel	0.094 %
64 x 64	0.02 to 0.05 pixel	0.3 %
32 x 32	0.05 to 0.2 pixel	1.25 %
16 x 16	0.1 to 0.3 pixel	5 %

Table 2. Influence of DIC subset size on the calculated strain and displacement values [72].

Dealing with rigid body motion and drift

SEM imaging and FIB milling are both reliant upon the acceleration and focusing of electrons and ions. This results in relatively strong electromagnetic interaction with the sample surface. In the case of a highly insulating sample, or one in which a clear conduction path to the earth connection is not present, the build-up of charge can influence the path of incident electrons used for imaging, and thereby cause the apparent image distortion and sample drift. This effect reduces the quality of SEM images and the effect on the ion beam may manifest itself as a drift in the milling position. Both effects reduce the effectiveness of the DIC marker tracking. Several techniques have been used to reduce the impact of charging; improved mounting and the introduction of conduction paths by sputtering thin (a few nm) conductive coating (for example, Au or Pd), or applying conductive paint to provide conductive path close to the region of interest or charge neutraliser systems can also be used.

DIC software can generally accommodate in-plane rigid body motion and drift, but if the movement between successive images is excessive the correlation can sometimes breakdown. In extreme circumstances the area over which the DIC displacements are calculated might move out of the field of view and this can ultimately effect the accuracy and relevance of subsequent residual stress calculations.

To alleviate this problem some FIB-SEM systems can be set up to correct for drift automatically during milling by using fiducial markers on the sample, positioned outside the region of interest or milling (Figure 43), which enables the area of interest on the sample to remain largely in the field of view.

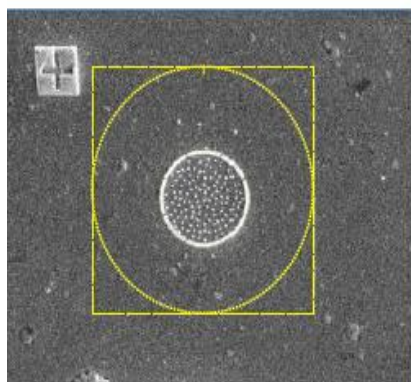


Figure 43. Example of fiducial marker for tracking and maintaining a stable field of view.

If this solution is not available, the problem of drift can be mitigated to some extent by either using a lower magnification to more readily accommodate the movement, but this will be at the expense of accuracy and resolution. **Although not recommended, if images are**

repositioned manually between milling steps, care must be taken not to change the magnification or SEM scanning conditions. Figure 44 shows an example of milling a Double slot geometry where there has been excessive drift (~over 100 pixels in y) effectively reducing the area over which the DIC displacements could be calculated. In this example, if a higher magnification had been chosen it is highly likely that the area of interest would have drifted completely from the field of view causing the experiment to be abandoned.

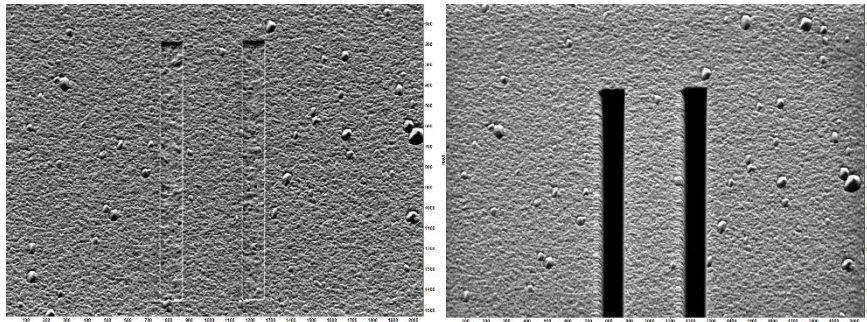


Figure 44. Example showing excessive drift during milling (over 100 pixels in y).

If drift is still an issue an effective approach is to carry out some form of image “registration” or “shift correction” after capturing the images so that all are effectively centred about a point in the field of view and a new coordinate system. This will only affect the relative magnitudes of the displacement field, by applying an offset at each point, relative to the origin of the new coordinate system; it will not affect the calculated strains. Figure 45 compares displacement vectors from images with drift (left) and those that have been “shift corrected” (right) to take into account the large-scale movement.

The magnitude and origin of the displacements is clearly different as shown in Figure 45 below, which shows equivalent displacement vectors from processing the images with drift (left) and centred about a fixed point (right).

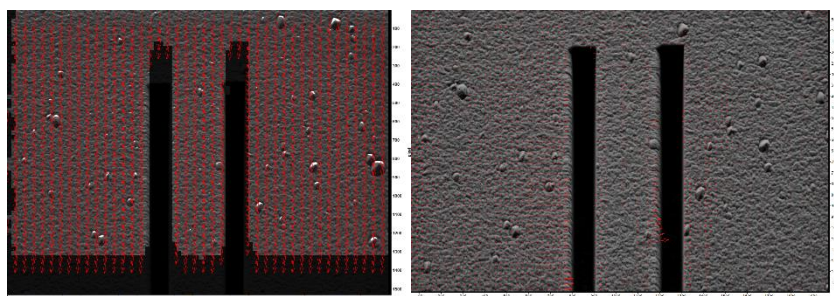


Figure 45. Results of processing (DIC vectors) without drift correction (left) and with (right).

Using intermediate images as the DIC reference

The choice of reference image against which the DIC is carried out is also important and can influence the quality of the subsequent DIC calculations. They should be good quality and represent the original state of the sample or component being tested. In the case of the FIB-DIC measurements of interest in this work, this will be the original condition with residual stresses present.

There may however be situations when the original images are unsatisfactory or corrupt. In such cases it is usually still possible to carry out the DIC analysis by using either a different “reference image” taken at some known state close to the start of the test, but recognising that the very first part of the data will be missing and the subsequent strain and displacement data may be offset by an unknown amount.

There may also be occasions when image quality degrades throughout the test resulting in the breakdown of the DIC calculations with respect to the original reference images. In such cases a useful approach is to use intermediate images as the reference against which the DIC calculations are made and sum the sets of individual displacements calculated from these. This will have an effect on the ultimate accuracy of the calculations as the errors associated with small changes between sets of successive images will increase and there is also the cumulative effect of adding these together.

Using the correlation coefficient

The correlation coefficient is a useful indication of the quality and accuracy of the DIC displacement field and should be examined in parallel with the DIC displacement outputs, as it is possible to generate DIC displacement fields which look reasonable, but contain significant errors due to poor correlation.

When sharp, high contrast, low noise images are captured, the cross-correlation surface typically takes the form of a single, sharp and well defined peak as shown in Figure 46a. The peak correlation coefficient in this case is close to 1, and the sharpness of the peak provides a precise estimate of the relative offset. In the case of a poorly focused, blurred or low contrast image, significant peak broadening is observed in the cross-correlation surface illustrated in Figure 46b. Even though the correlation coefficient in this case may also be close to unity, the precision of the displacement evaluation between the two images is much reduced. Cross-correlation of images containing large amounts of noise will result in a high roughness cross-correlation surface as shown in Figure 46c. Noise also produces random differences between the reference and deformed image subsets, thereby reducing the magnitude of the correlation coefficient at the peak. These two effects lead to a large decrease in the signal to noise ratio, and a reduction in the precision of displacement determination between the two images.

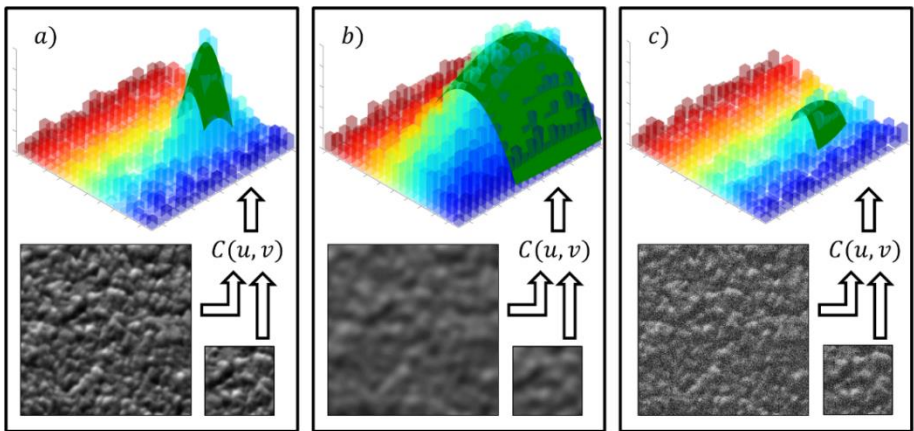


Figure 46. Effect of image quality and on the correlation peak [73].

Examination of the three cases outlined in Figure 46 demonstrates that the correlation coefficient on its own does not provide a good measure of the precision of displacement determination. Despite this, the parameter is a useful thresholding measure to remove noisy data points. **It can also be used as an effective mask to automatically eliminate the milled area from the DIC calculations as the correlation will break down where material has been removed.** In addition to providing sub-pixel resolution DIC, peak fitting also gives an estimate of the standard deviation of peak position. This is a much more reliable measure of displacement determination precision, and therefore is critical for error estimation and the removal of poorly tracked markers.

Figure 47 shows representative maps of correlation coefficient from a range of tests carried out by four partners in the iSTRESS project, after a variety of samples with different patterns have been shifted by a few pixels. Ideally the value of the correlation coefficient should be close to 1 and be random across the field of view. A value significantly less than 1 means an associated error will be present in the calculated displacement fields. The correlation coefficient should also be independent of the pattern, but that is not the case in some of the examples shown below where the correlation coefficient follows the pattern or breaks down where there are gaps in the pattern. **This again highlights the importance of having a random pattern, and that image quality has an important influence.**

Choosing the correct combination of DIC parameters for the pattern density and expected displacement field is important as it can have a large influence and affect the quality and accuracy of the subsequent DIC calculations.

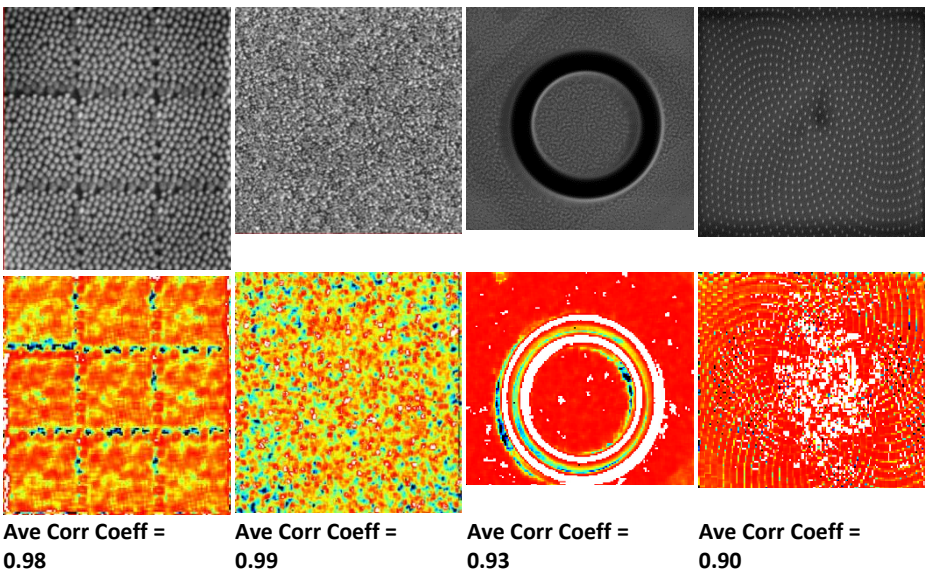


Figure 47. Example images and DIC correlation coefficients.

The correlation coefficient is affected most by the quality of the images, but the choice of DIC parameters is also important. It is often still possible to carry out DIC on poor quality images with low values of correlation coefficient, **but every attempt should be made to maximise the value by appropriate choice of DIC parameters relevant to the particular milling geometry, image quality and resolution, and the uniformity and gradient of the displacement field.**

Strategies for post-processing and cleaning of DIC data

Image quality is probably the most important parameter affecting the DIC results and every effort should be made to optimise images during the acquisition stage. The recommendation for averaging images prior to DIC processing was discussed in Chapter 8 and should be followed but it may also be necessary to carry out additional filtering and cleaning of the images, particularly with respect to reducing noise.

Prior to carrying out any filtering of the DIC data it is recommended that the DIC displacement field be examined carefully, and if necessary the DIC parameters varied and the processing of the images re-run to try to optimise the result and reduce the need for significant post-processing of the data.

Different DIC software packages will offer a variety of filters and options for fitting and cleaning the data and some of those used in the iSTRESS DIC software are detailed below.

Generally, applying sharpening, smoothing and edge detection should be avoided as these can introduce significant artificial artefacts which can affect the DIC processing.

Noise, which is independent of spatial coordinates can be compensated by spatial filters (e.g. median, mean); spatially dependent noise can be reduced by low-pass filters (e.g. Gaussian). Brightness and contrast adjustment may be necessary to correct for poorly exposed images but should be used carefully as should image normalisation as this may lead to inconsistent results if correcting a set of images taken over a long period of time, which might vary significantly in quality.

At stages during the DIC processing there may also be a need to carry out some post-processing to improve the quality of the displacement field and strain data. Low-pass filters, based on different criteria are often used to remove outliers and mathematical fitting of the data will be used to obtain the strain relief curves.

The DIC displacement data in particular should be examined to identify anomalies or inconsistencies that may affect the subsequent strain relief and residual stress calculations. The removal of poorly tracked DIC vectors/markers (and their outliers) may be necessary to give a more reliable estimation of the resultant displacement field. Ineffective tracking can be caused by a variety of different effects including aliasing, re-deposition of FIB milled material onto the sample surface, noisy images or changes in the surface pattern near the milling locations. A range of different techniques, each with their own strengths and limitations, can be used to remove outliers including thresholding based on the correlation coefficient or peak position standard deviation, the local displacement of markers/vectors and outliers to the expected displacement field. Experience demonstrates that a combination of these methods typically provides the best possible overall result.

Depending on the software used, some of these operations can be chosen explicitly by the user; in other cases they may be applied implicitly in the DIC software itself and the user has no control over their parameters or application. Care should be taken to both consider and understand what the post processing or filtering of data is doing, particularly if such processes are at the expense of accuracy. It is important also to report exactly what post processing has been carried out.

Correlation coefficient thresholding

The maximum correlation coefficient can be used as a threshold to remove markers/vectors for which there is a large difference between the reference image and deformed image, for example when there are large amounts of noise. It can be used as a simple technique to leave only markers with a high magnitude peak in the cross-correlation surface. Figure 48 shows an example where correlation coefficient thresholding has been used to remove a number of vectors with values of correlation coefficient below 0.7, but this has resulted in the loss of a significant proportion of the markers. **Care should be taken to ensure that an excessive**

number of markers are not removed as this can lead to the fit to the displacement data used to define the strain being compromised.

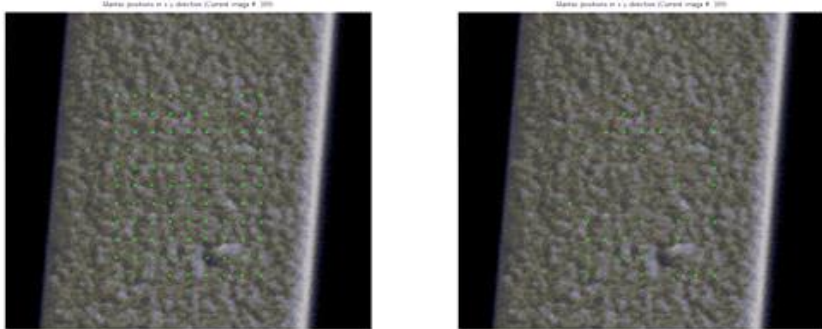


Figure 48. Reduction of DIC markers through correlation coefficient thresholding.

Peak position standard deviation thresholding

As mentioned earlier, the standard deviations of the estimates of peak position provide estimates of the sharpness of the peak in the cross-correlation surface. Relatively high standard deviations in either direction indicate a poorly tracked marker, and therefore thresholding can be used to leave only those markers with high precision peak estimation. A typical histogram of the peak position standard deviation for the Ring-core FIB milling and DIC approach is shown in Figure 49.

Care must be taken when choosing the threshold value: for example, 0.2 pixels is effective for the data in this case. The application of thresholding to this data set was warranted, since noise will typically result in an increase in the standard deviation of all the markers. An effective approach is therefore to threshold values based on a parameter descriptor of the set, for example the average.

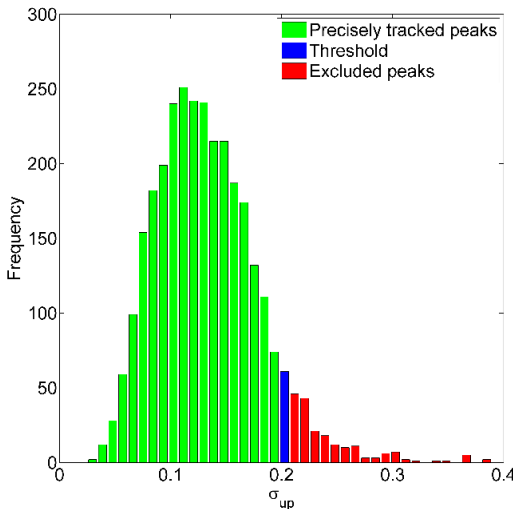


Figure 49. Histogram of the peak position standard deviation, showing a thresholding of 0.2 pixels [73].

Markers moving relative to neighbours

The vector displacement field associated with each of the DIC markers/windows can be analysed to assess if any show large displacements relative to their neighbours, and thereby remove those erroneous points. In the case of the FIB-DIC Ring-core and Double slot geometries, the displacement fields observed within the gauge volume are approximately uniform, so such anomalies are relatively easy to spot. Various criteria can be used including comparing displacement to one or several of the nearest neighbour(s) or to the average displacement over the gauge volume or area of interest. Vector removal is also usually performed iteratively by removing markers showing the largest discrepancies and recalculating the relative shift of all other markers.

Outliers to the expected displacement fields

FE modelling or analytical calculations can be used to characterise the displacement fields associated with each type of milling geometries. Least squares fitting of the expected displacement field profile can then be used to determine one or more scaling parameter values, and the fitting process used to estimate the distance between each marker and the expected profile. Thresholding can then be used to remove markers which are far from the nominal distribution. This process can be effective in removing any remaining outliers but care must be taken to ensure that the initial fit is representative of the behaviour observed. **This**

process must therefore only be performed after other outlier removal techniques have been applied.

In the case of the iSTRESS Ring-core geometry, uniform strain is assumed, and the expected displacement field is linear across the central core. The distance between markers and this linear trend can be used to remove outliers as shown in Figure 50. As noted above, care must be taken when selecting a suitable threshold for tall the data sets. Based on previous experience, a value equal to 1.5 times the average distance is a robust displacement limit for this application and dataset (as implemented in Figure 50c).

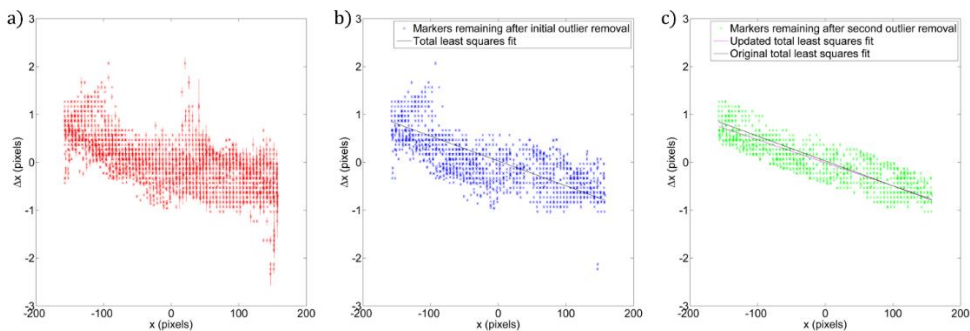
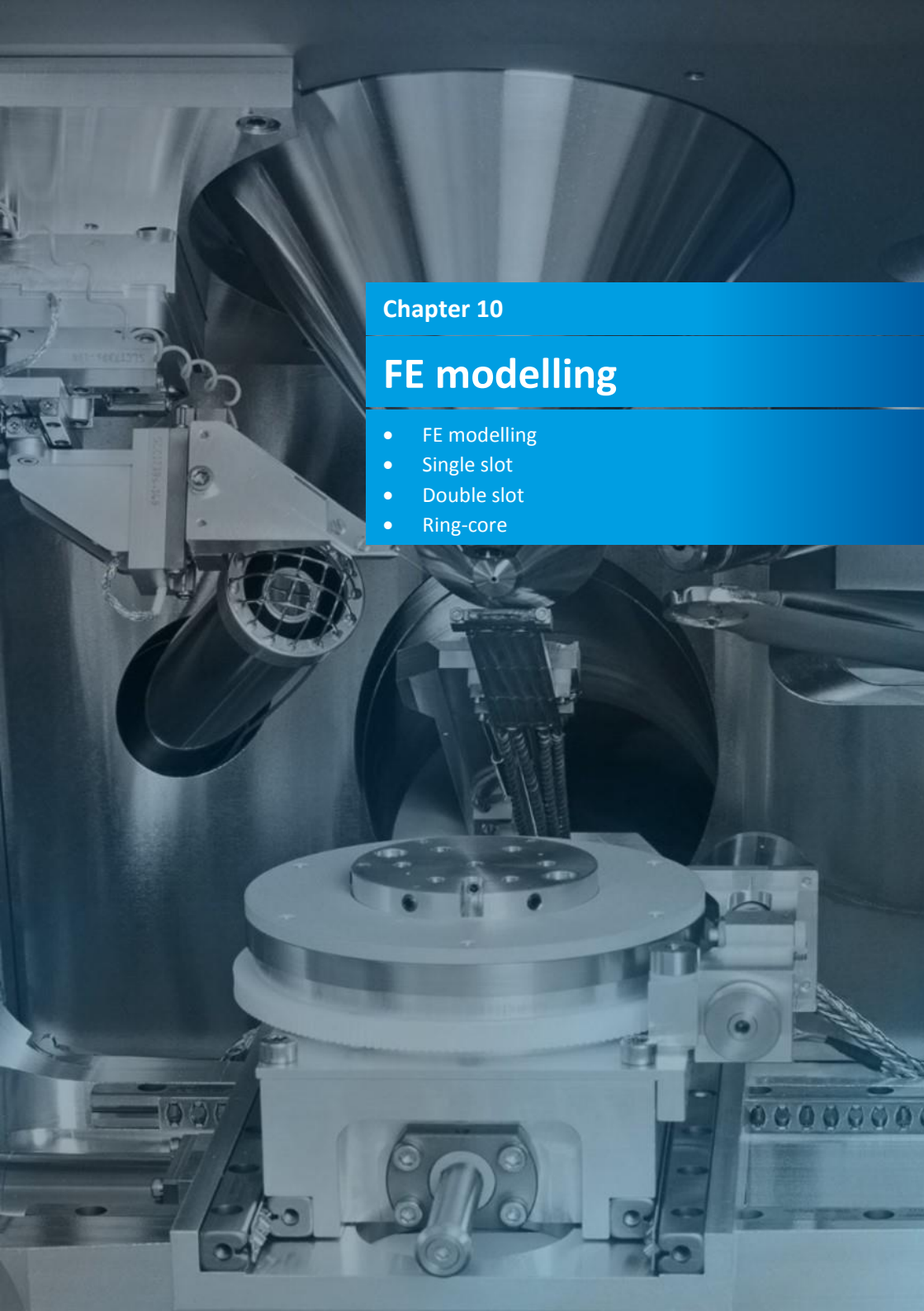


Figure 50. Example of the progressive removal of markers through thresholding and outlier removal to generate the linear fit to the linear x -displacement data (in Figure 50c) [73].

Manual marker removal

Manual examination of the strain or displacement fields produced by DIC serves as an effective approach in revealing outliers and poorly tracked markers. Typically, a peak in the strain or displacement field is indicative of a poorly mapped region or marker and can therefore be manually removed from the data set. These regions are often associated with aliasing, the impact of FIB re-deposition or the surface profile changes within the milled region.

This page was intentionally left blank.



Chapter 10

FE modelling

- FE modelling
- Single slot
- Double slot
- Ring-core

FE modelling

FE modelling of the milling geometries is essential for investigating and optimising the proportions of the milling geometries themselves, and for calculating displacement and strain fields within the gauge volume for the calculation of residual stress and validation of the experimental data. Details from studies on the different geometries are given in the following sections.

Where possible the FE models have used the recommended iSTRESS milling geometries (Chapter 7, Figure 29) with unit material properties and loading conditions. The outputs can then be scaled by the elastic properties of the material being measured.

Single slot

FE models were created to represent material with a Single slot milling geometry; the slots were 12 µm long and 1 µm wide. Both rectangular profile and V-shaped slots were modelled at a range of milling depths to determine the displacement fields and the effect of geometry. Figure 51 shows representative x and y displacement fields associated with a perfect, flat bottomed slot at milling depths of 0.5, 1, 1.5, 2, and 3 µm, plotted on the same scale to show the relative changes with increasing milling depth.

To ensure that the x -displacement profiles are not affected by end effects, the recommended iSTRESS single slot geometry has been scaled up (60 µm x 3 µm) to give a longer gauge length with a consistent displacement profile. The displacements in the y direction, which are concentrated about the ends of the slots, are negligible and can be ignored.

Figure 52 shows the predicted displacement profiles taken along a line perpendicular to the slot axis as a function of milling depth. Symmetry is assumed so only the profiles from one side are shown. Selected profiles from the V-shaped slot are also included and show little difference from the rectangular, flat bottomed geometry. This is relevant as in practice the milled slot is unlikely to maintain the flat-bottomed geometry with increasing depth, but the FE model shows that the actual geometry is not too critical and has little effect on the surface displacements, particularly as the slot becomes deeper.

The magnitude of the displacements (Figure 52a) is greatest close to the edge of the slot and falls significantly within the first 5 µm (which represents ~5x the slot width in this case). In practice it is difficult to measure the displacements very close to the edge of the slot due to redeposition and milling artefacts but the distribution can still be used in the calculation of residual stress. **For this milling geometry only the DIC displacement distribution is used; strains do not need to be calculated.**

Further modelling of the single slot geometry, together with details of the DIC processing and analysis developed by one of the iSTRESS partners is presented in Appendix 2.

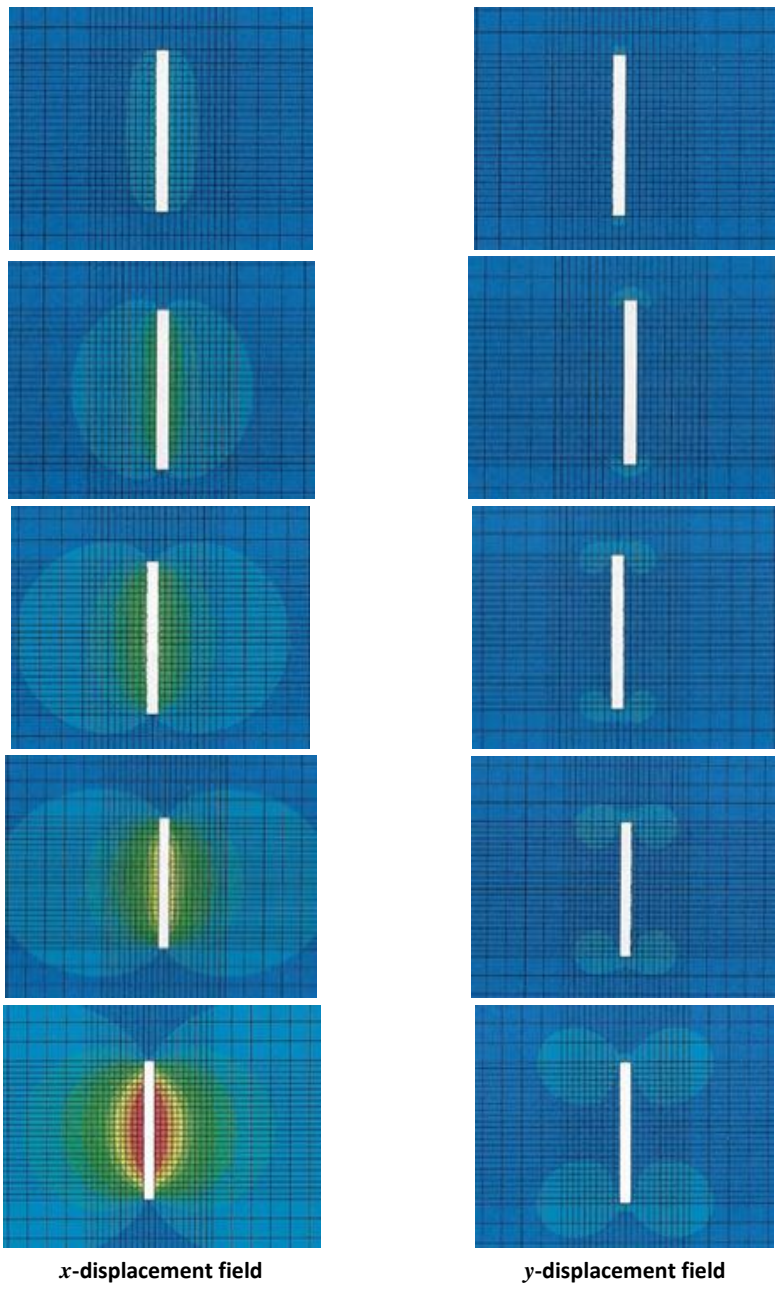


Figure 51. Predicted displacement fields developed during milling the Single slot geometry.

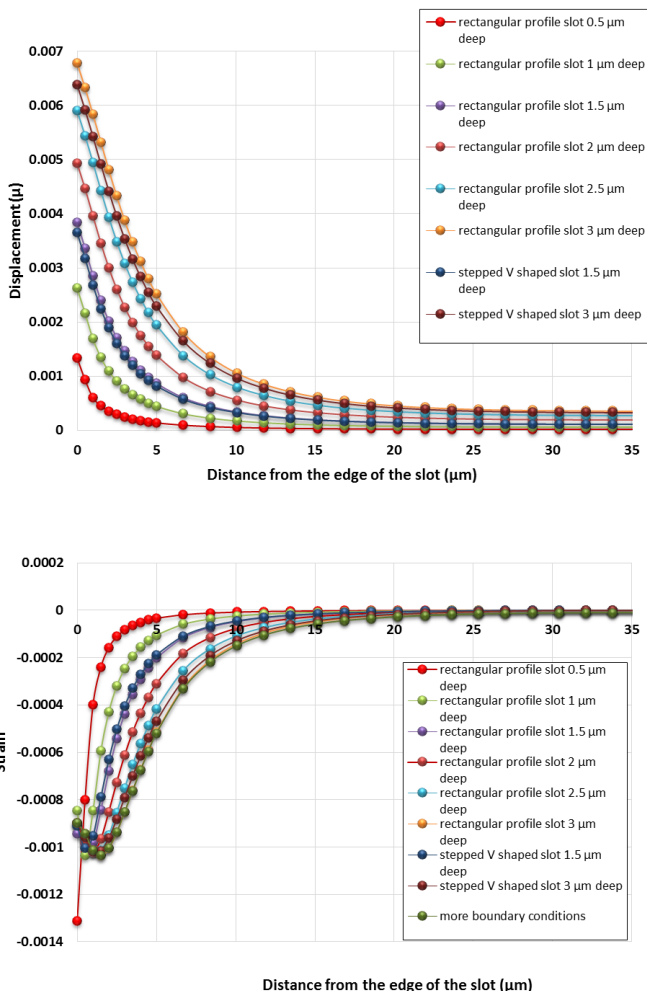


Figure 52. Predicted displacement profiles, V_x (top) and strain, ϵ_x (bottom) from the edge of the Single slot.

Double slot

As noted in Chapter 7 the Double slot or H-bar geometry is attractive because it offers uniform strain relief across the central island, although it only possible to measure residual stress in the direction normal to the slot axis.

To confirm the assumption of uniform strain in the gauge volume, FE modelling of the Double slot geometry has been carried out. Studies were made to examine the influence of slot dimensions and geometry on the strain relief, to identify the area of uniform strain and the potential errors that may be introduced by selecting areas where edge effects might affect the strain values. This was achieved by first modelling a Single slot geometry and superimposing the output when a second, adjacent slot is introduced. The same unit material properties and loading conditions were used.

Figure 53 shows the predicted strain distribution in the x -direction at different milling depths for the region between two $1\text{ }\mu\text{m}$ wide rectangular slots, $3\text{ }\mu\text{m}$ apart, chosen to simulate the recommended iSTRESS Double slot milling geometry (Chapter 7, Figure 29). The strain in the centre of the gauge volume is reasonably uniform apart from areas close to the ends and the very edges of the central island.

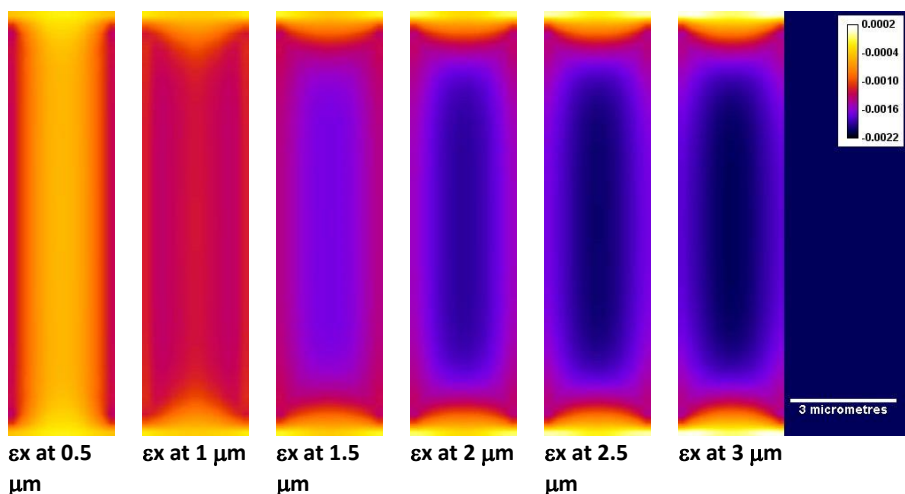
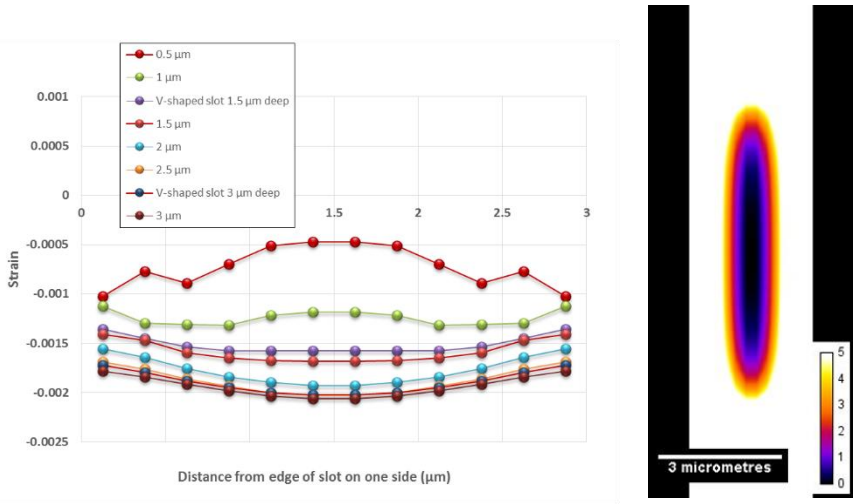


Figure 53. Evolution of the predicted x -direction strain relief in the central section between two rectangular slots, $3\text{ }\mu\text{m}$ apart at various milling depths.

Figure 54 shows the variation of the strain with slot depth in the x -direction across the central island, showing a reasonably uniform profile across the whole $3\text{ }\mu\text{m}$ width, particularly at greater slot depths. Figure 54b shows the percentage difference in the strain compared with that at the centre of the island at a depth of $3\text{ }\mu\text{m}$. Even though it appears as if there is an area

of uniform strain in the centre, there is still some variation which will add to the uncertainty in the average strain values, so the area over which the strain is calculated is important and should be considered carefully to minimise this variation.



b) % variation in strain

Figure 54. Predicted variation of strain with slot depth across the central island in the Double slot geometry.

A further series of 3D FE simulations was carried out to determine the strain relief profile generated from milling the Double slot geometry. Quadratic temperature-displacement elements were used, and a wide range of material property combinations were considered ($E = 70-200-350 \text{ GPa}$; $\nu = 0.15-0.3-0.45$), with the assumption of isotropic elastic behaviour. The stress relief induced by milling was simulated by the incremental removal of elements after the application of a constant calibration unit stress. The surface increment strains $\Delta\varepsilon_x$ and $\Delta\varepsilon_y$ were assumed to be given by the strain differences with respect to the original residually stressed state, and were calculated over the central square area after each removal step as a function of the milling depth h .

The FE results after the two-slot milling operation are shown in Figure 55. It shows the plot of the computed strain relief over the central island for all material combinations. For the purposes of normalisation, all strain increment values have been multiplied by the plane-strain modulus, $E' = E/(1 - \nu^2)$, and divided by the (unit) initial residual stress. These values are plotted against the normalised trench depth, h/d , where h denotes the current depth of the trenches, and d the distance between them.

The results of the simulation also confirm that after milling $\Delta\epsilon_{yy}^{(I)} = 0$, provided the length of the two slots is significantly greater than the distance between them. If this is not the case however, then $\Delta\epsilon_{yy}^{(I)} \neq 0$ due to edge effects and interactions. For milling depths exceeding the inter-trench distance ($h/d > 1.2$), the normalised relaxation strain consistently approaches unity for all material property combinations, indicating complete uniaxial stress relief over the central area (Figure 55).

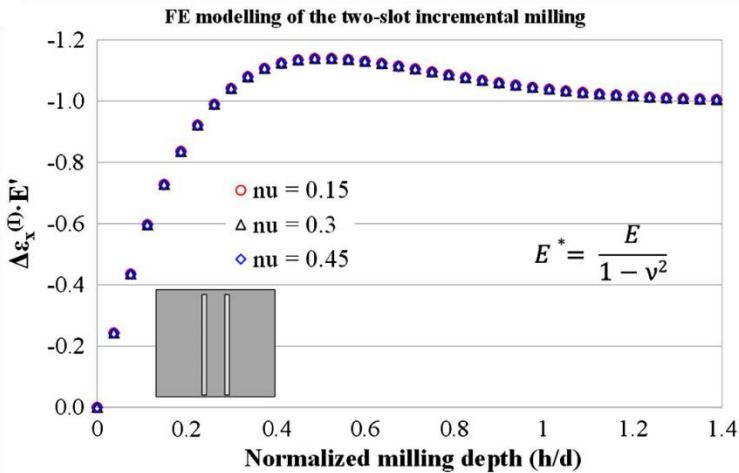


Figure 55. FE modelling of relaxation strain profiles for milling of two parallel slots giving full uniaxial stress relief, under plane strain conditions, for milling depths exceeding trench distance ($h/d > 1.2$) [28].

Of course the FE model shows the idealised case because it does not include any contributions due to milling, redeposition, variations in milling geometry, beam tail effects, drift etc. that can affect the actual distribution of strain relief. In practice, during milling there will be small variations towards the edges, so to reduce uncertainty and errors in the strain relief measurements these should be minimised by selecting an area in the central section of the island, as recommended in the iSTRESS milling geometries previously presented in Figure 29.

To further reinforce this point, Figure 56 shows the DIC x-displacement data from a Double slot milling test, taken at 10 depths. An image of the milled geometry has been superimposed to clarify the locations of the relative displacements. The results show a linear displacement across the central island, which corresponds to an area of uniform strain, and displacement profiles on the outside reminiscent of the Single slot. Local variations at the extremities of the slot can be seen, which are probably associated with redeposition and drift, reinforcing what has been discussed above about ignoring the areas close to the edges of the slot.

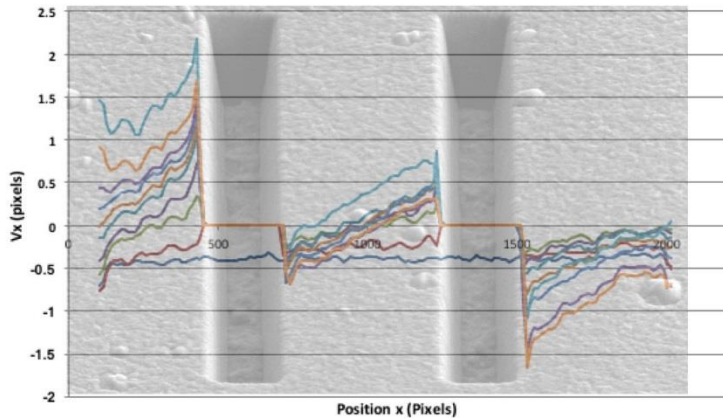


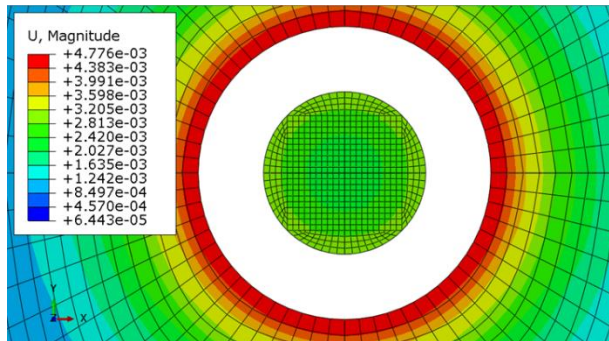
Figure 56. Average x -displacement profiles across the Double slot geometry, with increasing depth.

Ring-core

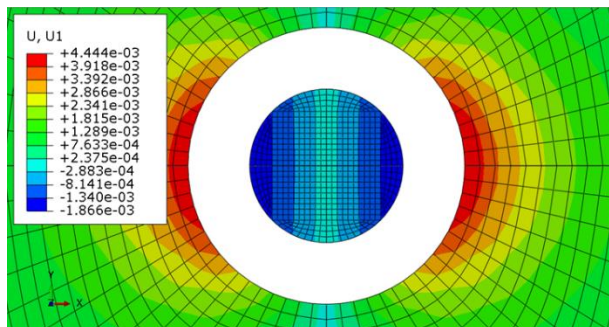
A similar exercise has been carried out for the Ring-core geometry to confirm the presence of uniform strain in the core. An FE model was developed in ABAQUS using C3D8R linear elements to represent the iSTRESS ring core geometry with a central core diameter of $5\text{ }\mu\text{m}$ and a trench width of $2\text{ }\mu\text{m}$ to match the recommended iSTRESS milling geometry. A quarter of the whole geometry was modelled and symmetry applied. Boundary conditions preventing displacement in the x , y and z directions were applied to one node at the base of each model to prevent whole body motion. The material was assumed to be isotropic, with a Poisson's ratio of 0.3 and uniform unit pressure was applied to the inner and outer surfaces of the ring trench to simulate the equibiaxial loading scenario. The model was run at $0.5\text{ }\mu\text{m}$ depth increments to show the evolution of displacement and strain fields with depth.

Figure 57 compares the displacements at full depth; Figure 57a the magnitude of displacement and Figure 57b and 57c the x and y displacement fields respectively. The full Ring-core geometry was modelled, showing the displacement fields outside the trench, which are representative and relevant to the Hole drilling geometry. Figure 58 shows the development of the strain in the core with increasing depth.

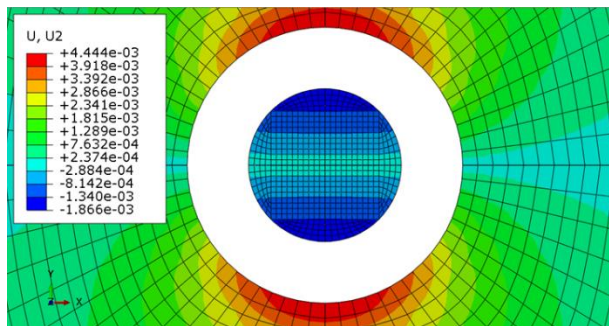
It is clear that most of the strain relief occurs in the early stages of milling and there is more variation in the strain field in the early stages of removal. At greater depths the strain becomes more uniform although, similar to the Double slot geometry, there is still some variation across the gauge volume and there are also edge effects. As a consequence the recommended area over which the strain should be calculated should be a maximum of 60-80 % of the core diameter, as specified previously in the recommended iSTRESS geometries (Figure 29).



a) Magnitude of displacement



b) x-displacement



c) y-displacement

Figure 57. Predicted displacement fields developed during Ring-core milling (shown at milling depth of 3 μm).

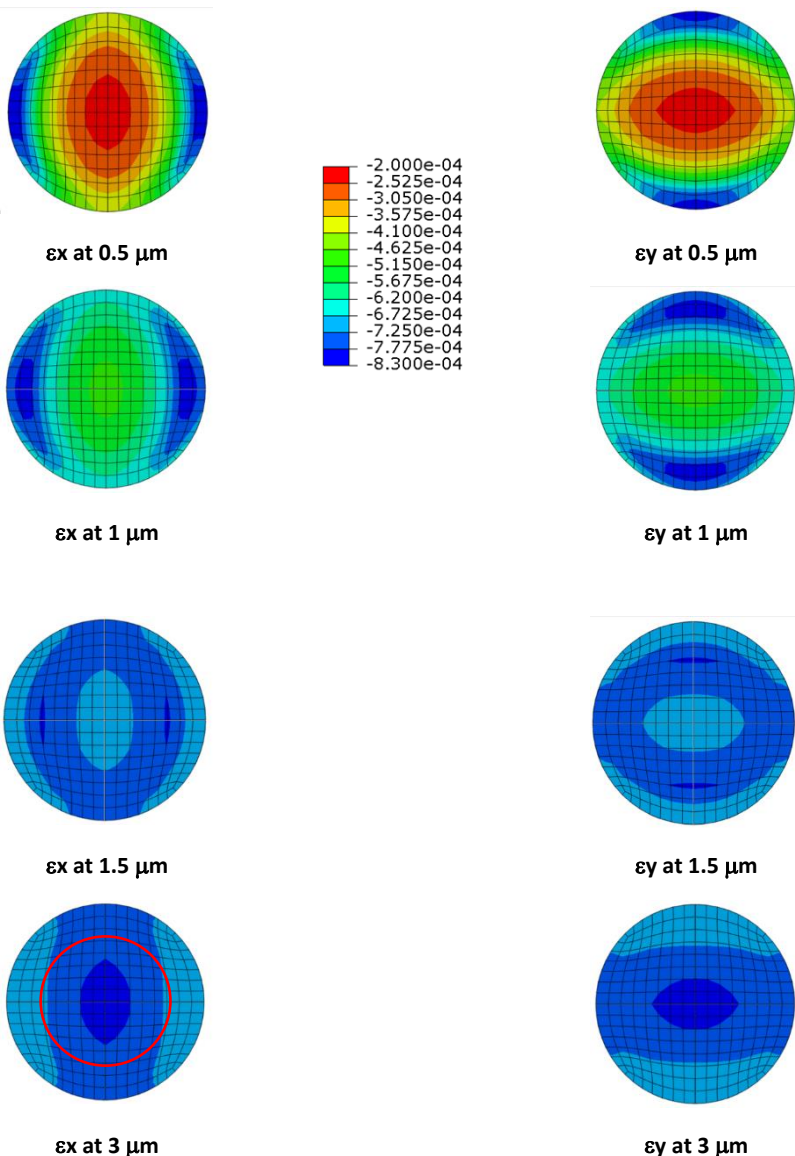


Figure 58. Evolution of strain in the core, with increasing milling depth (and in the bottom left, the recommended area over which the DIC strain should be calculated).

Figure 59 shows the predicted variation of elastic strain across the central island of the Ring-core geometry with normalised milling depth and radial position. As mentioned earlier, at shallow milling depths there are significant strain gradients close to the edges; but as the milling depth increases the distribution becomes more uniform. In this example the residual elastic strain in the material is the apparent strain at $h/d = 0 \rightarrow -0.00095$.

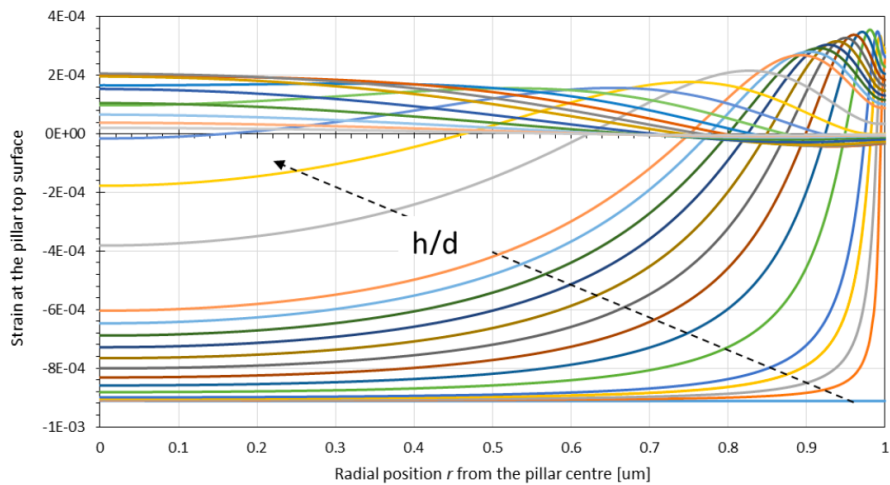
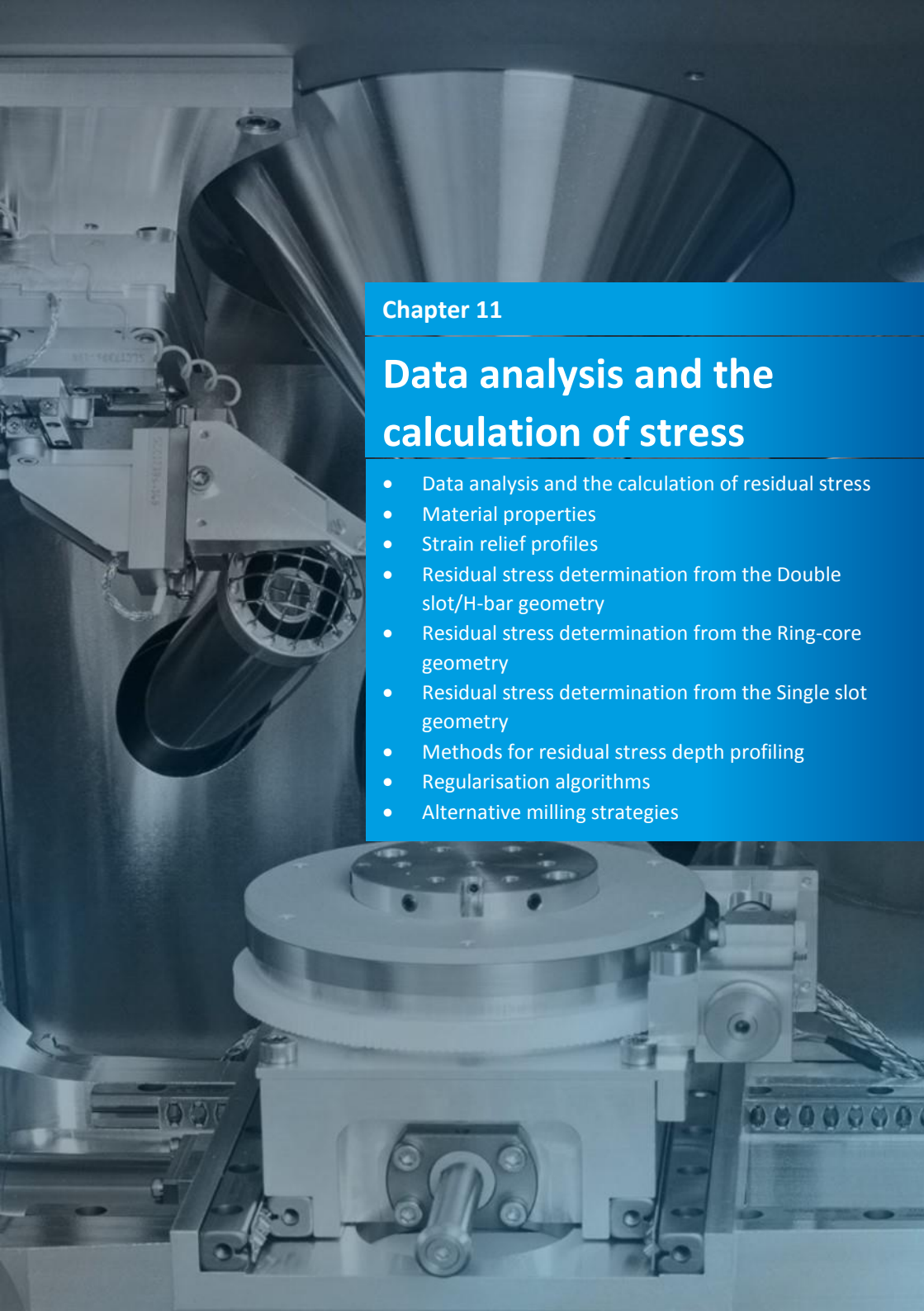


Figure 59. Predicted evolution of elastic strain with the normalised milling depth h/d for the Ring-core geometry.

This page was intentionally left blank.



Chapter 11

Data analysis and the calculation of stress

- Data analysis and the calculation of residual stress
- Material properties
- Strain relief profiles
- Residual stress determination from the Double slot/H-bar geometry
- Residual stress determination from the Ring-core geometry
- Residual stress determination from the Single slot geometry
- Methods for residual stress depth profiling
- Regularisation algorithms
- Alternative milling strategies

Data analysis and the calculation of residual stress

The fundamental basis of all FIB milling and DIC residual stress analysis techniques is the relationship that exists between the stress state originally present within the gauge volume of interest and the resulting strain relaxation measured by DIC after material has been removed. This relationship is based on accurate and precise quantification of one or more parameter descriptors of the DIC displacement field. For example, in the case of micro-slitting, the gradient of the linear displacement profile expected in the region surrounding the slot is matched directly to the results of FE simulations. Similar solutions for the other milling geometries have been developed to model the displacement and strain relief associated with the representative gauge volumes, and are presented in the following sections to enable the relief strain data measured from the FIB-DIC process to be converted to residual stress (or applied stress in the case of in-situ loading).

The relationship between surface strain relief and the residual stresses originally present in the surface forms the fundamental basis of the FIB-DIC technique. This relationship is based on the elastic stiffness constants of the substrate material, which follows from the assumption that no reverse plastic flow occurs during FIB milling. In the case of the Ring-core FIB-DIC geometry, this assumption is well-justified, since material removal causes proportional unloading towards the origin (unstressed state). In order to calculate reliable estimates of residual stress, both the surface strain relief and the elastic stiffness must be taken into account.

Material properties

Elastic modulus and Poisson's ratio are the two key material parameters required to convert the strain measurement to residual stress. For isotropic or untextured nanocrystalline materials, reliable values of continuum material elastic constants are available and can be used in the calculation of residual stress. Inside a typical FIB milling and DIC micro-scale gauge volume, many thousands of grains will be present in a nanocrystalline substrate material, so that the different elastic responses of each grain are averaged out, producing a response representative of the global (macroscopic) behaviour. **However for many applications of the FIB-DIC technique, there may be significant variations in microstructure within the gauge volume, and the use of the macroscopic modulus value is not strictly true and will lead to errors in the calculated residual stresses.**

In recent years a suite of analytical techniques has been developed to quantify the elastic behaviour at the micro-scale. The techniques provide insight into the mechanical behaviour at the same length scales as those probed by the FIB-DIC residual stress analysis, and can typically provide estimates of elastic behaviour that are more representative than bulk analysis.

The analysis of Young's modulus at the micro-scale can typically be grouped into two distinct experimental groups. The first is based on the use of micro-scale testing devices to apply

precise loads and to measure the resulting micro- or nano-scale displacements. For example, micro-scale quantification of Young's modulus has been calculated using miniaturisation of the bulk scale tensile loading test [74, 75], microbeam bending or deflection [76, 77], nanoindentation [78-82], atomic force microscopy [83], the so-called thin film biaxial 'bulge test' [84, 85], and through micropillar compression tests [86, 87]. Of particular interest is the micropillar compression tests as this configuration and geometry is identical to that used in the Ring-core FIB milling and DIC approach. The integration of the two techniques has the potential to provide measures of the strain relief, modulus and Poisson's ratio, all within a single experimental session.

An alternative approach for high resolution Young's modulus determination is based on the interaction between wave like media and the sample, such as surface acoustic waves [88-90], resonant ultrasound spectroscopy [91, 92] and X-ray diffraction [93], all of which have been used to quantify Young's modulus at the micro-scale.

The other case where a simple macroscopic value for modulus is not relevant is with anisotropic materials, where the stiffness is dependent upon the orientation. Elastic anisotropy can be due to underlying crystallinity, preferred grain orientation (or texture) or composite nature of the material. For example, the directional stiffness in Yttria Partially Stabilised Zirconia (PSZ) is known to vary by a factor of 2.6 depending upon the orientation in which load is applied [94]. The impact depends upon the relative size of the gauge volume and the anisotropic region. In the case where the anisotropic region is approximately equal to or greater than the gauge volume, orientation uncertainty may have a significant impact on the confidence intervals of the elastic modulus.

Poisson's ratio is another parameter which is a factor in the conversion from surface relief to residual stress. Several different approaches have been developed to quantify this parameter at the micro-scale, many which are based on similar methodologies as those used in the quantification of Young's modulus. For example, nanoindentation, atomic force microscopy, the thin film 'bulge test', surface acoustic waves and X-ray diffraction [95] have also been used to quantify Poisson's ratio at high resolution. Alternative techniques based on bidirectional thermal expansion [96] or the use of FIB milling [28] can also be used to determine Poisson's ratio at the required scales.

In recent decades the development of techniques to grow macro-scale single crystals has allowed control of creep e.g. of nickel-based superalloy materials, and widely increased the capabilities of optical systems [97]. In these systems the crystal orientation is typically determined through EBSD, XRD, or prior knowledge of the expected crystal growth direction [98]. The influence of grain orientation uncertainty, in combination with the impact of underlying processing parameters, then can be used to provide estimates of the overall uncertainty bounds.

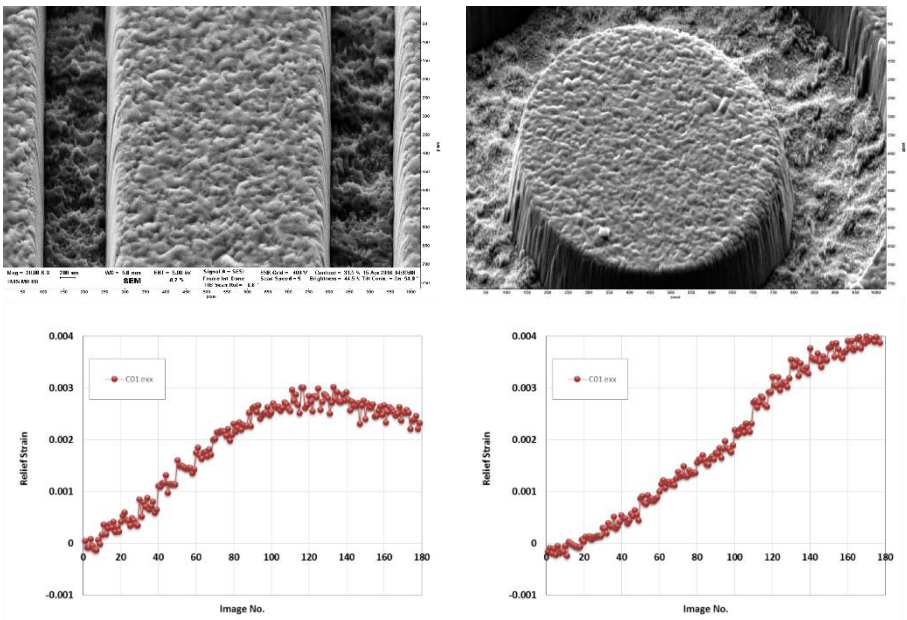
An alternative approach based on statistics can be used to declare the residual stress error bounds in the case of a single crystal substrate or in the intermediate case of when the gauge volume contains a small number of grains [62]. This approach is based on using the anisotropic elasticity to generate residual stress estimates for many thousands of randomly orientated grains, or equivalent grain sets. The resulting distribution can be used, in combination with confidence intervals for the strain relief, to obtain upper and lower bounds for the residual stress estimate.

It is important to note that many of the FE simulations of FIB milling and the resulting relaxation are based on the **assumptions of material isotropy and homogeneity**. In the case of single crystal or large grained materials (relative to the gauge volume size) these predictions will no longer be representative of the relief observed, and modified simulations are required in such systems.

Strain relief profiles

For calculating the average residual stress it is only strictly necessary to measure the strain relief at full depth, but it is important to ensure that this has been successfully achieved. **As noted previously it is recommended therefore that incremental milling is carried out and the strain relief plotted at different milling depths.** Figure 60 shows representative profiles generated from the recommended iSTRESS Double slot and Ring-core geometries from an intercomparison exercise on a thin TiN coating. With the Ring-core geometry, milling was not carried out to sufficient depth to give full strain relief, as seen in Figure 60b.

Further examples of experimentally obtained strain relief profiles from Ring-core milling are presented in Figure 61; the profiles are from a 3 µm TiN coating on a silicon substrate and a 5 µm electroless Ni coating on a steel substrate. The relief strain is positive in the case of TiN coating, while it is negative in the case of Ni coating, reflecting the different nature of the residual stress present. Both cases are in excellent agreement with the numerically predicted curve. Note that, similarly to the curve predicted from FE simulations, the experimental stress relief profile shows a maximum, with a reduction of strain relief and then saturation at higher depths.



a) Double Slot

b) Ring-Core

Figure 60. Comparison of strain profiles obtained from the different milling geometries – iSTRESS intercomparison exercise on the C01 TiN coating.

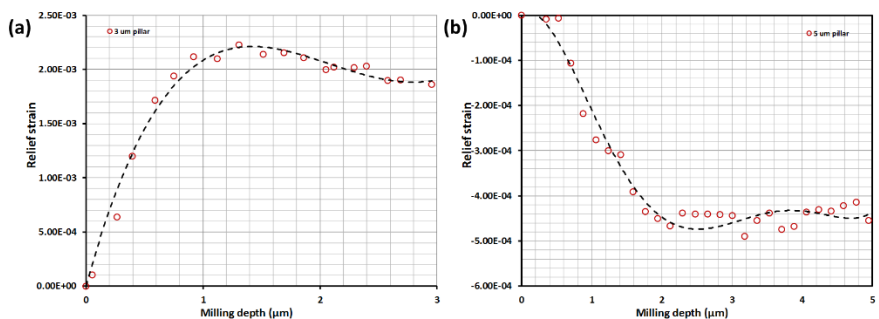


Figure 61. Experimentally measured relief strain on the (a) TiN coating and (b) Electroless Ni Coating.

Figure 62 shows a plot of the computed strain relief curve for the case of a constant equibiaxial stress through the thickness for a Ring-core geometry with $d/t = 1$. The relief strain has been normalised with respect to the biaxial modulus $E/(1 - \nu)$ and trench depth with respect to the core diameter (h/d).

For the Ring-core geometry the general form of the strain relief profile, the so called ‘master curve’ has been determined through FE simulations of the milling process [11] and a functional representation of the profile obtained [16]:

$$f(\Delta\varepsilon_\infty, z) = 1.12\Delta\varepsilon_\infty \times \frac{z}{1+z} \left[1 + \frac{2}{(1+z^2)} \right], \quad (1)$$

where $z = h/0.42d$, h is the milled depth, d is the core diameter and $\Delta\varepsilon_\infty$ is the full strain relief at an infinite milling (or full) depth. Most of the strain relief occurs in the early stages of milling close to the surface, and for $h/d < 0.3$, the relief profile is very steep. The relief profile demonstrates a peak at approximately $h/d = 0.4$ which is associated with the “pinch like” behaviour of the base of the core, and tends towards a plateau $\Delta\varepsilon_\infty$ at deeper milling depths ($h/d > 0.6$). An important observation is that the stress relief approaches unity for $h/d > 1$, meaning that **full stress relief is achieved when the trench depth is at least equal to its diameter**. This observation is independent of the elastic properties of the substrate. Furthermore despite often milling up to $h/d = 1$, it is important to note that the evaluated residual stress is an average value of the actual residual stress present in a shallower layer of material ($0 < h/d < \sim 0.3$).

Typically only nominal estimates of the milling depth are known and therefore a further parameter (η) is often introduced to relate the milling depth to the image number (I), such that $h = \eta I$. Setting this parameter to a constant implies that the milling rate remains constant throughout the process. As mentioned earlier, although this is approximately true in the near-surface region, the approximation becomes increasingly invalid at greater depths.

It is important also to note that the above conclusions are valid provided the core diameter, d , is equal to, or is smaller than the coating thickness, t . In the case where $d/t > 1$, a dependence of the relief strain profile on the elastic properties of the substrate may be observed. It is also worth noting that the relief strain was found to be nearly uniform over the surface of the core, as expected and already confirmed in the models presented in Figure 59, and the experimental DIC data.

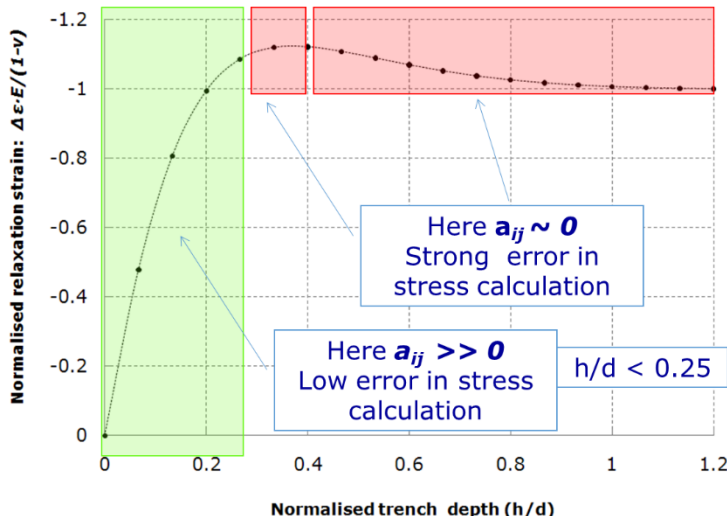


Figure 62. FE modelled normalised stress relief as a function of normalised drilling depth.

In the case of experimental data subject to noise, it is likely that the saturation region starting at around $h/d > 0.6$ cannot be clearly identified. The scatter in the calculated strain values can be reduced by introducing a weight function in the fitting process. This weight function must highlight the greater contribution given by the experimental data extracted in the region lying between $0 < h/d < 0.4$, according to Figure 62 above. An example of fitting noisy data is shown in Figure 63 below. **Although the fitting process has been performed successfully, it is worth noting that the evaluated residual elastic strain will be subjected to a larger uncertainty which cannot be ignored and should be included in the subsequent calculations.**

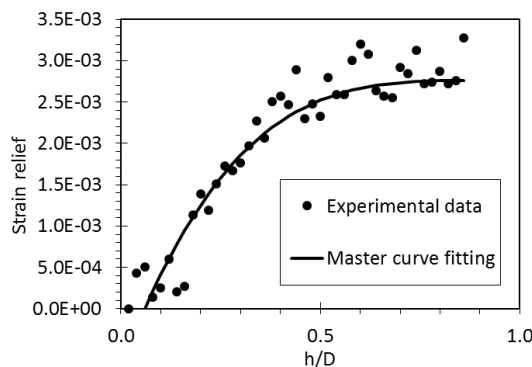


Figure 63. Example of strain relief fitting in absence of clear strain saturation.

Residual stress determination from the Double slot/H-bar geometry

The principles and details of how the residual stress is calculated from the strain relief obtained during milling is presented for the Double slot case below. A similar approach is used for the other milling geometries, but these are not covered in the same detail.

To begin, consider the typical biaxial stress state for a thin film attached to a substrate. The equibiaxial residual stress state $\sigma_{xx}^0 = \sigma_{yy}^0 = \sigma_R$, with the Cartesian axes x and y defined in the plane of the sample surface as shown in Figure 64.

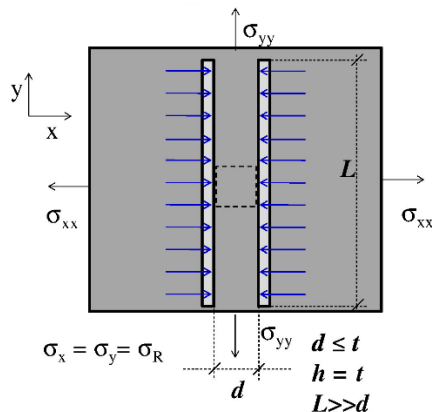


Figure 64. Milling of two parallel slots induces uniaxial stress relief $\Delta\varepsilon_{xx}^{(I)}$ [28].

The milling of two long parallel slots leads to uniaxial relaxation strain $\Delta\varepsilon_{xx}$ that occurs in the central squared area along the x -direction normal to the extent of the slots (blue arrows in Figure 64). Here d is the distance between slots, L is the length of slots, h is the depth of the trenches and t is the film thickness.

As noted previously the final depth of milling should be larger than the characteristic distance between the slots. **In the case of thin coatings, the distance between the slots should also be lower than the film thickness in order to reduce the effects of the interfacial stresses, which cannot be released by the milling procedure, as the coating will be still attached to the substrate.**

To derive the expression for residual stress, now consider the central squared island outlined by the dashed line. Due to the thinness of coating and the proximity of the free surface, the out-of-plane stresses can be assumed to be equal to zero. Therefore, the plane stress approximation gives:

$$\sigma_x = -\frac{E}{(1-\nu^2)} [\Delta\varepsilon_{\infty}^x + \nu\Delta\varepsilon_{\infty}^y] \quad (2)$$

$$\sigma_y = -\frac{E}{(1-\nu^2)} [\Delta\varepsilon_{\infty}^y + \nu\Delta\varepsilon_{\infty}^x] \quad (3)$$

The term $\Delta\varepsilon_{\infty}$ represents the level of strain achieved at the milling depth of $h/D \geq 1$ (milling at full depth) and is usually evaluated by using the fitting the master function curve in Eq. (1) to the experimental DIC strain data.

Let the initial residual deformation state of the coating that arises due to its attachment to the substrate be described by an equibiaxial elastic strain ε . According to the above equation, this corresponds to the residual stress state:

$$\sigma_{xx}^0 = -\frac{E}{(1-\nu^2)} [\varepsilon + \nu\varepsilon] = -\frac{E\Delta\varepsilon}{(1-\nu)} \quad (4)$$

where $\sigma_{xx}^0 = \sigma_{yy}^0 = \sigma_R$ is the initial equibiaxial state of elastic residual stress.

The depth of the two slots should be larger than the distance between them and, if this is the case, the stress component along the x -direction will be completely relieved after milling. However, since the coating remains attached to the rest of the film in y -direction and to the substrate all along the length of the central strip, the y -strain component remains unchanged. The deformation state at the specimen surface after milling can therefore be assumed to be:

$$\sigma_{xx}^I = 0, \varepsilon_{yy}^I = e \quad (5)$$

A special case involving the milling of Four slots is discussed below; for purposes of clarification the superscript I is used for the results of the conventional Double slot milling process and superscript II the additional stage involved in the Four slot milling.

It is worth noting that the length of the two slots is assumed to be significantly larger than the distance between them. Otherwise an apparent strain increment along the y -direction would also be observed, due to edge effects.

Using Eq. (2) the new component of strain in the x -direction must be given by:

$$\varepsilon_{xx}^I = -ve \quad (6)$$

Meaning that the increment of strain in this direction is:

$$\Delta \varepsilon_{xx}^I = -(1 + \nu)e = -\frac{1 - \nu^2}{E} \sigma_R \quad (7)$$

Where E and ν are the elastic modulus and the Poisson's ratio of the material under consideration. The biaxial residual stress σ_R can therefore be directly calculated using Eq. (7).

Figure 65 shows a full set of relaxation strain data as a function of the normalised depth (h/d), where a close agreement with the predicted strain profile is observed. Note that these data can be also effectively used for residual stress depth-profiling, using the calculation algorithm that was previously developed for the Hole drilling [25], slot milling [9] and Ring-core geometries [11].

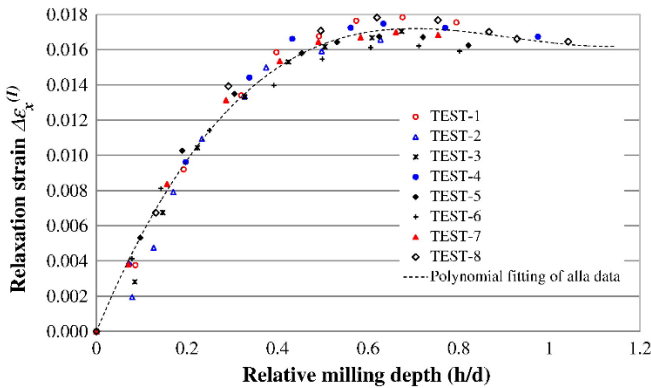


Figure 65. Complete strain data set as a function of milling depth during the two-slot milling sequence [28].

Four slot milling and the calculation of Poisson's ratio

A special case has been developed recently which uses an extension of the conventional Double slot milling to enable the calculation of Poisson's ratio [28]. The so-called "Four slot milling" initially follows the same steps as the Double slot or H-bar milling, but a second stage is used, whereby two additional slots are milled perpendicular to the first set to induce additional relaxation of the strain components (red arrows in Figure 66) and leads to full biaxial stress relief in the central island ($\Delta \varepsilon_{xx}^{(II)} = \Delta \varepsilon_{yy}^{(II)}$).

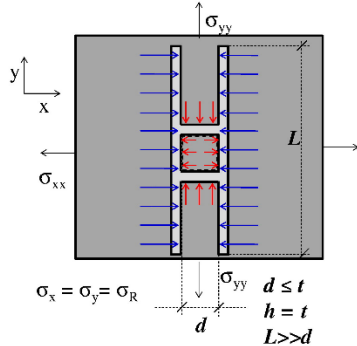


Figure 66. Milling of two additional perpendicular slots induces further relaxation strains that lead to a final biaxial full stress relief $\Delta\varepsilon_{xx}^{(II)} = \Delta\varepsilon_{yy}^{(II)}$ (additional strain components highlighted by red arrows)[28].

The general assumptions that the final depth of milling is larger than the characteristic distance between the slots and the requirement for the distance between the slots to be less than the film thickness still apply. Based on these assumptions, the key hypothesis is that the ratio between the two strain relief components (with respect to the initial state) in the x -direction ($\Delta\varepsilon_{xx}^{(II)} = \Delta\varepsilon_{yy}^{(II)}$) measured after Step-I (Original Double slot geometry) and Step-II (the perpendicular cuts), respectively, is a unique function of the Poisson's ratio of the sample volume.

After Step II milling, the in-plane stresses in the central square are completely relieved, i.e. $\sigma_{xx}^{II} = \sigma_{yy}^{II} = 0$, as are the final strains $\varepsilon_{xx}^{II} = \varepsilon_{yy}^{II} = 0$. Consequently:

$$\Delta\varepsilon_{xx}^{II} = -e = -\frac{1-\nu}{E}\sigma_R \quad (8)$$

Note that all strain increments are considered with respect to the initial equibiaxial stressed state. Finally, by computing the ratio of relaxation strain increments from Eqs. (7) and (8), it is possible to directly extract the Poisson's ratio as:

$$\nu = \frac{\Delta\varepsilon_{xx}^I}{\Delta\varepsilon_{xx}^{II}} - 1 \quad (9)$$

So Poisson's ratio can be directly evaluated using Eq. (9), on the basis of the two measured relaxation strains at the end of the two milling steps. It is worth noting that for cubic crystal structures, and in general for in-plane isotropic materials, the result is independent of the elastic constants, and does not rely on the prior knowledge of this parameter.

The FE results of the “Four slot” milling steps are shown in Figure 67. The plot of computed strain relief is shown for all material property combinations. The strain increment values are normalised by multiplication by the biaxial modulus, $M = E/(1 - \nu)$, and divided by the (unit) initial residual stress. These values are plotted against the normalised trench depth, h/d .

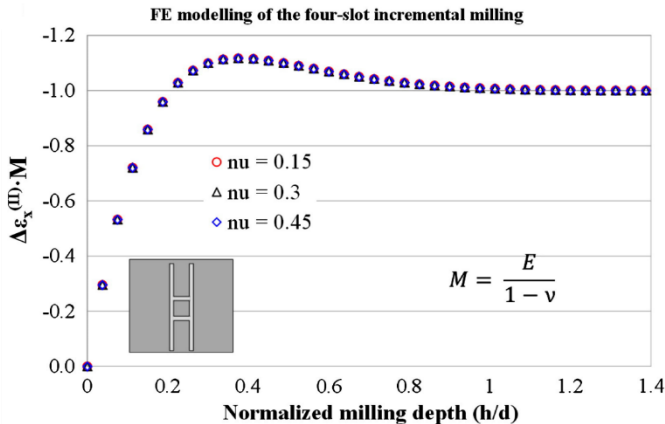


Figure 67. Results of the FE modelling of relaxation strain profiles for Four-slot geometry giving full biaxial stress relief for $h/d > 1$ [28].

In this case, biaxial stress relief occurs, and full saturation of the strain increments (i.e. complete biaxial stress relief) arises for the relative milling depths $h/d > 1$, which is in agreement with the prediction of Eq. (8). The FE simulations confirm that Eq. (9) can be applied for the evaluation of the Poisson's ratio for relative milling depths $h/d > 1.2$, which represents the minimum requirement for achieving full relief of both stress components within the square island at the specimen surface.

Figure 68 shows results from a four slot milling test on a CrN surface section. At Stage I, two parallel slots were milled incrementally at low ion current (48 pA) at 30 kV with depth increments of about 200 nm, and a series of SEM micrographs was acquired after each milling step (Figure 68b).

At Stage II, two additional slots aligned perpendicular to the existing slots were incrementally milled using the same incremental procedure and the same SEM image acquisition procedure. A full field analysis of the relaxation strain over the patterned area was performed after each milling step by a Matlab®-based DIC after averaging and noise filtering for each set of images.

Results are shown in Figure 68d, where the measured $\Delta\epsilon_x$ and $\Delta\epsilon_y$ of the whole two-step sequence are presented as a function of the incremental milling step number. The two-slot sequence comprises milling steps #1 to #14, whilst steps #15 to #27 correspond to the milling of the two additional perpendicular slots.

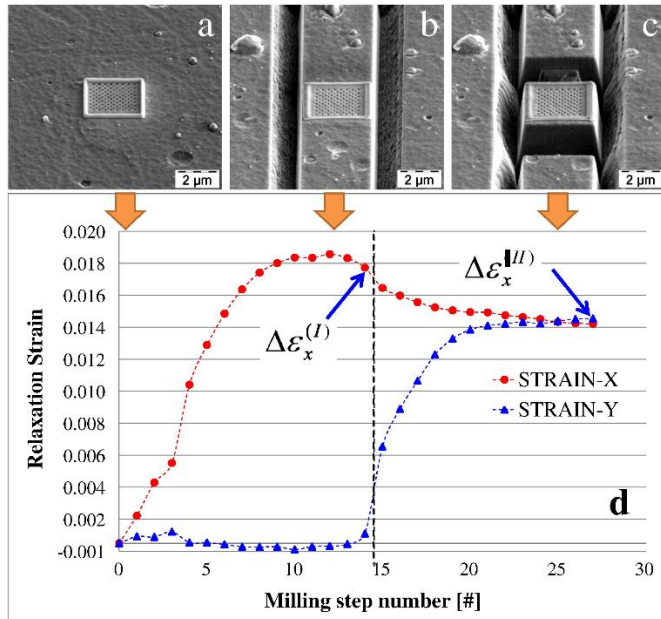


Figure 68. Example of a Four slot milling test on a CrN coating [28].

The data clearly show a steep increase of the strain relief $\Delta\epsilon_x$ during the two-slot sequence, where the $\Delta\epsilon_y$ is negligible as predicted by the model. The interpolated relaxation strain at the final depth during the two-slot sequence was then used to calculate the average residual stress in the coating, using Eq. (7) with the reduced modulus value obtained by nanoindentation. An average equibiaxial stress of -5509 ± 330 MPa was calculated for the CrN coatings and found to be in good agreement with results obtained by XRD.

As the milling of the two additional perpendicular slots begins (Stage II), a sharp increase of the strain relief $\Delta\epsilon_y$ is observed. This is accompanied by a gradual decrease of the $\Delta\epsilon_x$, due to the Poisson effect. At the end of the milling process, the two strain components are almost identical, as predicted by the model for the case of an equibiaxial stress state. The $\Delta\epsilon_x$ strain relief values at the end of each of the two milling stages are used to calculate a value for the Poisson's ratio using Eq. (9), which gives a value for the CrN coating of 0.248 in this case.

Residual stress determination from the Single slot geometry

As noted earlier, the determination of residual stress from strain relief caused by Single slot (or trench) milling is considerably different to the approach for the Ring-core and Double slot geometries. The main difference arises from the gauge volume being considered and the non-uniformity of the displacement and strain fields on both sides of the trench rim. Because the relief displacement and strain fields depend both on the slot/trench profile and the elastic material properties, an accompanying FE analysis is necessary, taking into account the parameters of the individual milling process.

FIB milling of the Single slot is followed by DIC analysis to obtain the displacement fields on both sides of the slot, following the procedures and protocols recommended in the GPG. Typical DIC displacement data is shown in Figure 69. **A detailed test protocol for the Single slot milling test has been developed by Fraunhofer ENAS, one of the iSTRESS partners, and is included in Appendix 2.**

Results from the FE analysis of the expected relaxation field are then scaled to match the DIC data to give the residual stress. Because of the assumption of linear elastic stress relief, the residual stress and the DIC displacements, both components perpendicular to the slot line, scale with the same factor B , giving:

$$\sigma_{xR} = B\sigma_x^{FE} \quad (10)$$

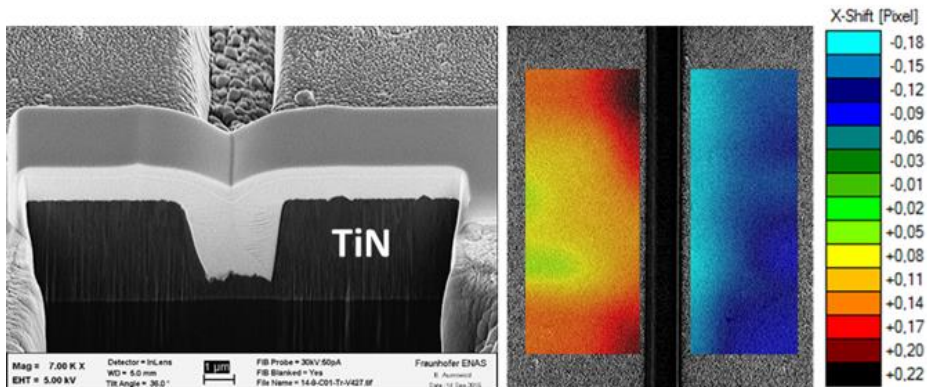


Figure 69. DIC displacement data from the Single slot milling.

Residual stress determination from the Ring-core geometry

Assuming that homogeneous and isotropic assumptions can be applied at the length scales under consideration, expressions for the non-equi-biaxial principal stresses in the surface (σ_x and σ_y) for the Ring-core FIB milling and DIC technique are [16]:

$$\sigma_x = -\frac{E}{(1-\nu^2)} [\Delta\varepsilon_{\infty}^x + \nu\Delta\varepsilon_{\infty}^y], \quad \sigma_y = -\frac{E}{(1-\nu^2)} [\Delta\varepsilon_{\infty}^y + \nu\Delta\varepsilon_{\infty}^x], \quad (11)$$

where E and ν are the Young's modulus and Poisson's ratio, respectively.

These are identical to those for the Double slot presented in the previous section and the basic procedures, assumptions and calculations are the same. However, unlike the Double slot geometry where only uniaxial strain relief is present, biaxial strain relief occurs during Ring-core milling.

The term $\Delta\varepsilon_{\infty}$ once again represents the level of strain achieved at the milling depth of $h/D \geq 1$ (milling at full depth) and is usually evaluated by using the fitting the master function curve in Eq. (1) to the experimental DIC strain data.

Figure 70 below shows the full strain relief analysis performed in three different directions from incremental Ring-core milling in a shot peened IN718 nickel-based superalloy. The core diameter was 5 μm , trench width was 1.5 μm and milling steps of 100 nm used. Milling was performed to a nominal depth of 5.3 μm to ensure that complete strain relief was achieved. Multiple images were taken at each step and DIC carried out on the averaged images using the iSTRESS DIC software. To quantify the specific estimates of $\Delta\varepsilon_{\infty}$, non-linear weighted least squares fitting of the expression in Eq. (1) were used, and the principal strain relief orientations and magnitudes were then determined from the 0°, 45° and 90° strain relief values.

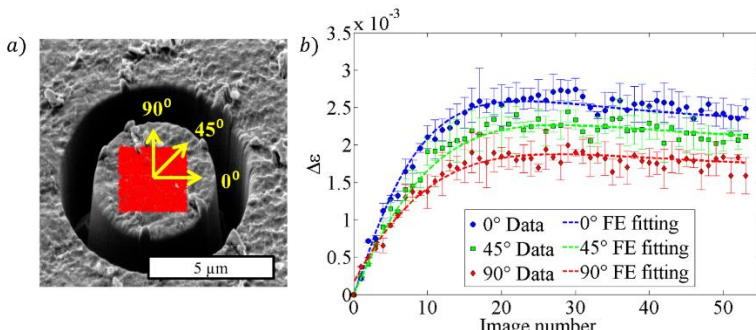


Figure 70. Example of Ring-core milling and associated strain relief profiles (with fit) in a shot peened nickel superalloy [73].

Methods for residual stress depth profiling

All of the examples and analyses presented in the GPG are based on calculating an average residual stress value in a shallow layer of material, but it is also possible to measure the variation of stress with depth using a more sophisticated depth profiling approach and analysis using the *Integral Method*, which was originally developed by Schajer [60] for macroscopic Hole drilling. The method is summarised in the NPL GPG No. 53 [6], a companion to this guide aimed at measuring residual stresses using the incremental centre Hole drilling technique.

During the FIB milling process, removal of material from the first increment results in surface strains that relate directly to the residual stresses relieved within that increment. Removal of material from the second milling step produces two effects. Firstly, the stiffness of the structure is changed such that there is further relief of stresses within the layer of material corresponding to the first increment, producing a strain change at surface, and secondly, the stresses relieved at the boundary of the second increment produce an additional strain change. Thus, even if the second increment contains no residual stress, any stress within the first increment will produce a change in strain at the surface as the second increment is milled.

The evaluation of the average residual stress and stress profile in the sample volume requires the solution of an inverse problem, which is usually in the form of an integral equation. The approach assumes that the total measured relaxation strain at a certain depth $\varepsilon(h)$ is given by the integral of the infinitesimal strain relief components due to the removal of tractions at all depths in the range $0 \leq H \leq h$, that is:

$$\varepsilon(h) = \int_0^h B(H, h) \cdot \sigma(H) \quad (12)$$

Here, $\sigma(H)$ is the local stress which was present before material removal at depth H , and $B(H, h)$ is the influence function (also called Kernel function) that describes the strain caused by a unit stress at depth H within a hole of depth h . Eq. (12) holds in case of an equi-biaxial stress state, which is the most representative situation for the case of thin coatings of interest in this GPG . An effective method for solving Eq. (12) is to divide the unknown stress profile into n discrete calculation points:

$$\varepsilon_i = \sum_{j=0}^{j=i} \sigma_j \cdot b_{ij} \quad 1 \leq j \leq i \leq n \quad (13)$$

where b_{ij} is a lower triangular matrix of calibration coefficients which relates the strains relaxed at the surface when the trench has j depth increments to the principal stresses acting

in the i layer, as shown schematically in Figure 71 and is usually obtained by FE modelling. This example is given for 4 calculation increments; coefficients a are arranged in a similar manner.

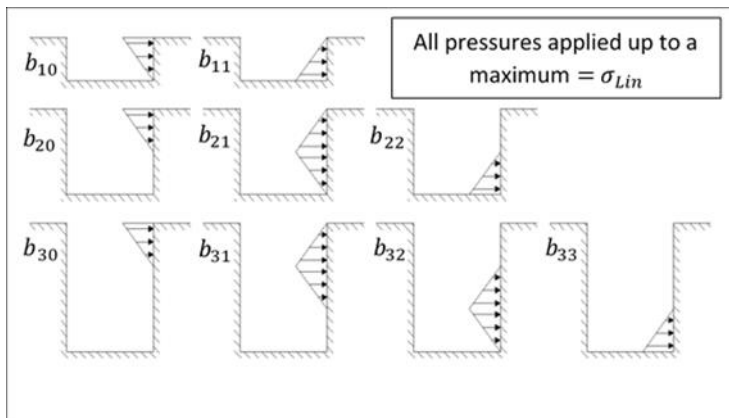


Figure 71. Milling and stress depths corresponding to the b_{ij} coefficients.

One of the main advantages of the *Integral Method* is the ability to decode relaxed strains that relate to highly non-uniform residual stress distributions. To calculate the residual stresses from the relaxed strains, Schajer proposes that the hole (or milled geometry in this case) should be produced using many small increments so that the resulting strain data can be smoothed or filtered to reduce noise. However, the number of calculation increments that can be supported depends on the quality of the experimental data. Five or six calculation increments yield a satisfactory level of detail for many stress distributions, but if this number is significantly increased, then the residual stresses between successive calculation increments may be seen to oscillate about the original stress level, and excessive ‘smoothing’ of strain data to reduce oscillation (to permit the use of smaller stress calculation increments) is unlikely to reveal a significant increase in the ‘true’ stress distribution detail, especially towards the full depth.

As shown previously in Figure 62, the sensitivity of the FIB method reduces with milling depth. This is not a feature of the *Integral Method*, but rather a reflection of the fact that, as the milling depth increases, the stress change caused by material removal is located further from the surface where the strain relief is being measured. This limitation is more severe for the a coefficients than for b coefficients so uncertainties in the average values of principal stresses are usually greater than uncertainties in differences between principal stresses.

The piecewise constant nature of the *Integral Method* means that an average stress value for each milled increment is produced as an output. This leads to a discrete estimate of the reconstructed stress averaged over the step size used. Steep gradients or sharp oscillations in

the stress cannot be represented accurately without the use of small step sizes which requires a more complex and time-consuming experiment. Also, the best possible estimate of the residual stress at the surface is actually half the step size away from this point (unless some form of extrapolation is used), so improvements to the technique have been proposed based on the regularisation algorithms described in the next section.

Regularisation algorithms

Tent functions

As with any system, a piecewise linear interpolation of an unknown quantity is known to be much more effective than a single constant estimation. One approach is to use a reconstruction based around “tent-functions”. In the formulation used, linear stress profiles can be applied within the FE model at different milling depths, and a matrix \mathbf{B} computed, so that:

$$\mathbf{B}\sigma = \boldsymbol{\varepsilon} \Rightarrow \begin{bmatrix} b_{10} & b_{11} & 0 & 0 \\ b_{20} & b_{21} & b_{22} & 0 \\ b_{30} & b_{31} & b_{32} & b_{33} \end{bmatrix} \begin{bmatrix} \sigma_0 \\ \sigma_1 \\ \sigma_2 \\ \sigma_3 \end{bmatrix} = \begin{bmatrix} \varepsilon_1 \\ \varepsilon_2 \\ \varepsilon_3 \end{bmatrix} \quad \text{or} \quad \varepsilon_i = \sum_{j=0}^{j=i} \sigma_j \cdot b_{ij} \quad 0 \leq j \leq i \leq 3 \quad (14)$$

where ε_i and σ_i have the same notation as above and b_{ij} relates to the milling increment at step i to the stress at step j . This process has the added advantage of producing an estimate of the surface stress σ_0 .

In order to implement this technique, an additional FE model is required at each milling depth and linear profiles of stress up to a pressure of σ_{Lin} were applied as shown in Chapters 10 and 11. A similar technique is then used to calculate the individual b_{ij} values from $b_{ij} = \varepsilon_{ij}/\sigma_{Lin}$ and these values are used to populate matrix \mathbf{B} .

Inversion techniques

Following the same procedure as used in the piecewise constant *Integral Method* technique, the $\boldsymbol{\varepsilon}$ vector is then measured experimentally. However, matrix \mathbf{B} is not square, meaning that it cannot be inverted simply in the form $\sigma = \mathbf{B}^{-1}\boldsymbol{\varepsilon}$. One possible solution to this problem is to use the pseudo-inverse of \mathbf{B} to find σ where $\sigma = \mathbf{B}_{Pseudo}^{-1}\boldsymbol{\varepsilon} = [\mathbf{B}^T \mathbf{B}]^{-1} \mathbf{B}^T \boldsymbol{\varepsilon}$ and \mathbf{B}^T is the transpose of \mathbf{B} . However, this inversion approach relies only upon the mathematical construct used to calculate \mathbf{B}_{Pseudo} , which is not based on a sound physical interpretation of the Hole-drilling process.

In order to introduce a physically-based inversion approach, an additional relationship between one or more σ_i values needed to be identified. The Hole drilling technique is known to become more limited in resolution and reliability at deeper cuts. Therefore to avoid instabilities and to obtain a reliable estimate of the deep stress, it is possible to assume that

the stress at the deepest cut (σ_n) is equal to the previous stress value (σ_{n-1}). Adding this additional equation to \mathbf{B} also requires the concatenation of a zero to the bottom of $\boldsymbol{\varepsilon}$:

$$\beta\sigma_n - \beta\sigma_{n-1} = 0 \Rightarrow \begin{bmatrix} b_{10} & b_{11} & 0 & 0 \\ b_{20} & b_{21} & b_{22} & 0 \\ b_{30} & b_{31} & b_{32} & b_{33} \\ 0 & 0 & -\beta & \beta \end{bmatrix} \begin{bmatrix} \sigma_0 \\ \sigma_1 \\ \sigma_2 \\ \sigma_3 \end{bmatrix} = \begin{bmatrix} \varepsilon_1 \\ \varepsilon_2 \\ \varepsilon_3 \\ 0 \end{bmatrix} \Rightarrow \bar{\mathbf{B}}\boldsymbol{\sigma} = \bar{\boldsymbol{\varepsilon}} \quad (15)$$

This allows $\boldsymbol{\sigma}$ to be calculated from $\bar{\mathbf{B}}^{-1}\bar{\boldsymbol{\varepsilon}}$. However, the stability of this technique requires further analysis. Careful selection of parameter β does allow a well-conditioned $\bar{\mathbf{B}}$ to be formed.

Comparison with the piecewise constant technique

In order to be able to make a direct comparison between the new linear interpolation technique and the piecewise constant approach, the original Schajer method was implemented. Modifications to the values and positions of the nodal forces were then made in order to develop the uniform stress profiles. Implementing both the piecewise constant and linear interpolation *Integral Method* techniques on the same strain vectors ($\boldsymbol{\varepsilon}$) meant that direct comparisons could be made between the accuracy of the two approaches.

The plots in Figure 72 show the reconstructed and implemented profiles for a Hole drilling model in a mild steel shot peened surface (Young's modulus 200 GPa, Poisson's ratio 0.3) in which cut step intervals of 0.1 mm were used

The results show that the fit produced by the piecewise linear technique is much more effective than the piecewise constant approach. This is especially true when considering the approximation of the surface stress value σ_0 ; the piecewise constant approach has an error of 43 % whereas the linear interpolation *Integral Method* technique gives an error of less than 1 %. This demonstrates that for the noise-free case the linear piecewise approach offers an improvement in accuracy and resolution without the need for more refined or complex experimentation.

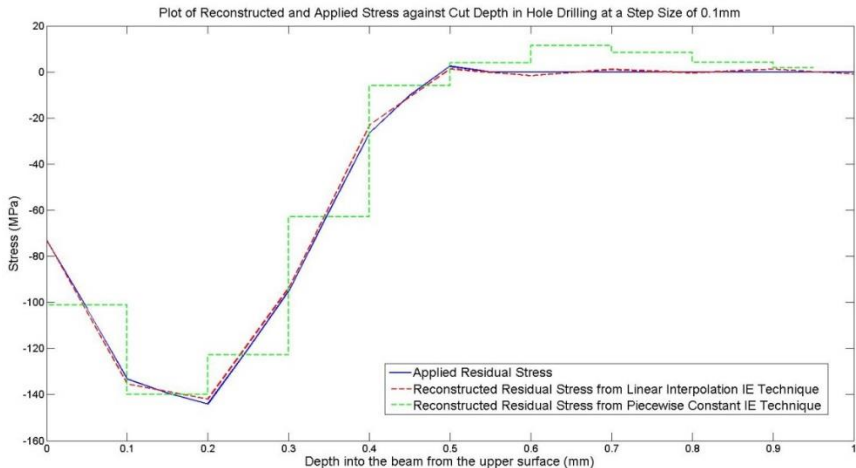


Figure 72. Plot of reconstructed and applied stress in a mild steel numerical Hole drilling analysis.

Alternative milling strategies

An alternative strategy for residual stress profiling is to mill a series of differently sized geometries and calculating the average stress from each test.

This could be achieved for example, by milling a series of scaled Ring-core geometries with core diameters and corresponding depths of 1, 3, 5, 10 and 15 μm to give a series of discrete average stress measurements covering the whole depth.

This is not a particularly practical solution, however, due to the number of milling experiments required and the time and costs involved. There are also difficulties associated with accurate milling of very small geometries (the 1 μm diameter Ring-core for example) because milling damage and deposition can completely obscure and mask the area required for the DIC strain measurement. Furthermore, any uncertainties associated with the smallest milling geometries are likely to have a large effect on the calculated stress values as they fall exactly where the strain relief gradient is steepest.



Chapter 12

Validation

- Reference materials and system checks
- Tests on standard materials
- In-situ testing

Reference materials and system checks

It is good practice with any measurement to check and validate the technique by carrying out tests using standard materials or agreed protocols. Comparisons with results from other techniques is also valuable. In the absence of a current International Standard for the FIB-DIC residual stress measurement technique a number of tests were carried out within the iSTRESS project to validate the results and test protocols being developed. These included checks using a stress-free Si wafer “reference material” to examine the stability and performance of the different FIB systems (Chapter 8), measurements using reference images to validate the DIC software (Chapter 9), and round robin tests on well characterised materials containing residual stress to develop the FIB-DIC procedures. Some of the other tests used to help validate the technique are discussed below.

Tests on standard materials

In the absence of relevant certified reference materials containing residual stresses, a series of test were carried out within the iSTRESS project using well characterised materials that were relevant to the project partners and the FIB-DIC approach. These included various TiN coatings, BMGs, nano-crystalline Ni and a single crystal Ni- superalloy. Some of the results are presented in the following sections.

TiN coatings

Titanium nitride (TiN) is one of the most widely used coatings in the industry and is a benchmark for wear resistance, diffusion barriers and decorative purposes. For the tests, two titanium nitride coatings with a thickness of 3.5 µm were deposited on a silicon (100) wafer by Montanuniversität, Leoben using different process parameters, and a set of identical samples produced from each batch. Figure 73 shows a representative sample prepared for the exercise and the area over which the FIB-DIC measurements were to be made. The average residual stresses were also evaluated using other benchmark techniques by wafer curvature and conventional X-ray diffraction $\sin^2 \psi$ method [5] and results are summarised in Table 4 below.

TiN Sample	Textured (Yes/No)	Curvature stress (MPa)	XRD stress (MPa)
C01	No	-650 ± 50	-660 ± 40
C02	Yes	-550 ± 50	-790 ± 30

Table 4. Average residual stress values on TiN samples using the benchmark techniques.

C01 sample

In order to validate the applicability of the FIB-DIC method, the C01 sample was tested for average residual stress using the dual beam instruments from four different manufacturers (FEI, Zeiss, Tescan and Jeol) at different locations across Europe. A range of milling geometries was used. Figure 74 compares the results of the average stress values measured using FIB-DIC, with those made using wafer curvature and XRD.

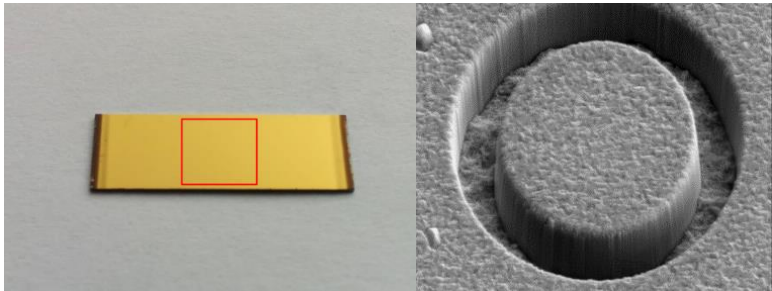


Figure 73. A TiN coating on Si substrate highlighting the area for FIB-DIC analysis, and (right) a Ring-core geometry (no additional pattern required).

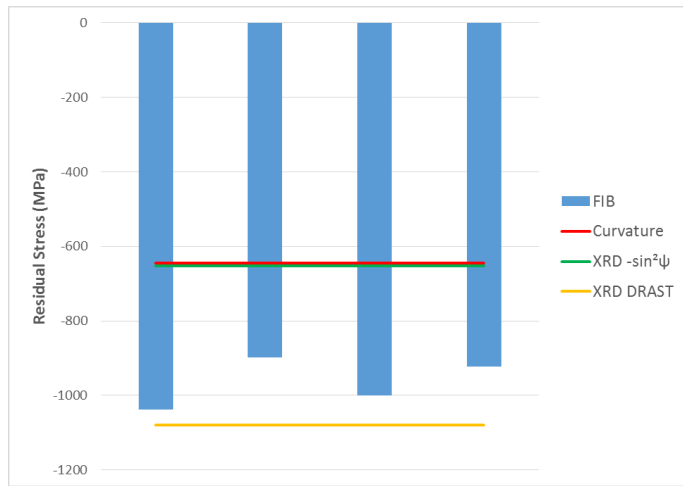


Figure 74. Average residual stresses in C01 TiN sample measured using different techniques and FIB-SEM instruments.

It is clear from Figure 74 that the results from the different partners and instruments are in good agreement. It also highlights that for low crystalline textured samples (i.e. isotropic distribution of crystal orientations); both XRD and curvature methods

give very similar results. This is not the case for the highly textured samples however, and the following section summarises the results for the C02 sample, which have highly developed crystalline texture.

C02 sample

Table 4 summarises the average residual stress values for the C01 and C02 TiN samples using the wafer curvature and standard X-ray diffraction $\sin^2 \psi$ methods. It is clear from the results that the average values for the C02 variant are different due to the presence of strong texture in the sample. In the case of anisotropic materials, the standard XRD procedure for evaluating stresses have to be improved, using texture data to provide reliable results. If the TiN sample is tested using a diffractometer capable of grazing angle diffraction, care must be taken in the interpretation of the results. For example using a *Rigaku D-Max RAPID* system with a modest 15° incidence angle gave results significantly different from the previous measurement techniques. In this case, the calculated compressive stress was more than -900 MPa, which was in good agreement with the values measured in a separate Synchrotron experiment (Figure 76).

Regarding the FIB measurements, contrary to the previous sample, the results are very close to those measured by curvature method. In this case the FIB measurement seems to be less affected by stress gradient, probably because it is less strong, as suggested by XRD results.

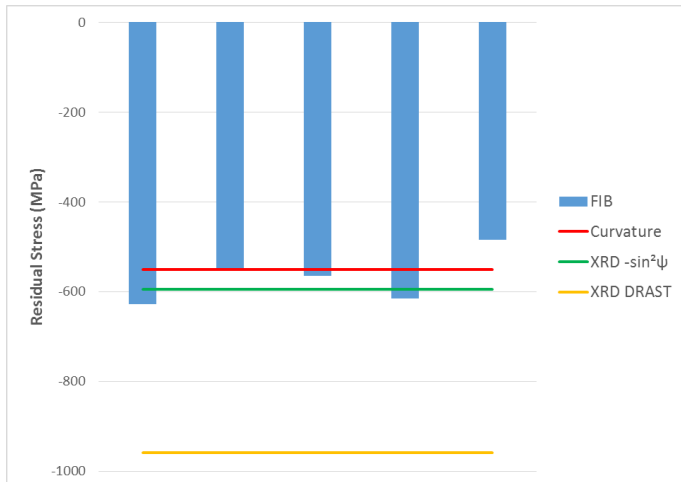


Figure 75. Average residual stresses in C02 TiN sample measured using different techniques and FIB-SEM instruments.

The C02 sample was then further tested with synchrotron nano-diffraction technique to evaluate the residual stress through the thickness. The technique is fully analogous to conventional stress measurement by XRD but uses a very fine (50 nm) X-ray pencil beam. For the C02 sample, a stress gradient across the thickness was measured, from a compressive stress of a -1 GPa on the surface to an approximate -200 MPa compressive stress close to the interface (Figure 76). The grazing incidence diffraction results from XRD (a value of -900 MPa) can only be considered as the average stress value from the top 1 μm of the coating.

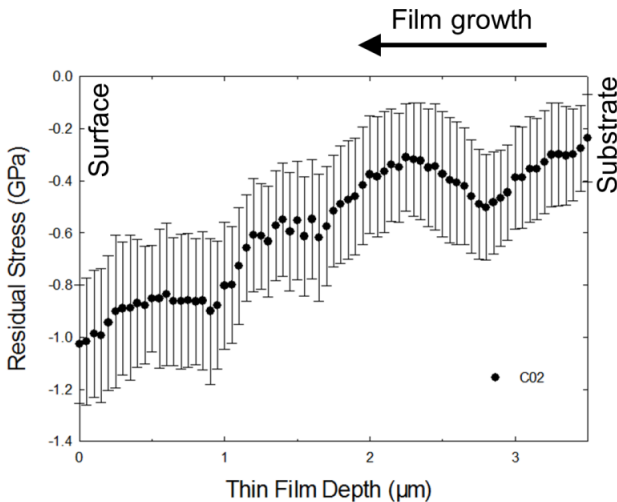


Figure 76. Synchrotron residual stress measurements through the thickness of the C02 sample.

In-situ testing

Another useful test for validating the experimental set up is to use in-situ loading, whereby an external stress is applied to the sample. The choice of test will depend both on the size and form of the sample and the in-situ loading rigs available to the FIB user.

The four-point bend test is particularly useful as the sample experiences both tensile and compressive stresses within the gauge volume. Within the iSTRESS project a series of bending experiments were performed on nanocrystalline nickel (isotropic) and a single crystalline nickel-based superalloy (anisotropic) to confirm the validity of this approach. The aim was to measure the bending stress gradient by FIB-DIC method in combination with the results from FE analysis and to compare the measured results with the theoretically calculated stress values from bending theory.

To achieve this, several Double slot/H-Bars geometries were milled into the surface at different positions across the loaded sample covering the full stress range. Figure 77a shows a close up of the sample in the miniature bend rig and Figure 77b an SEM image of a Double slot geometry milled into the CMSX-6 sample. Bending experiments on both samples were performed on different FIB instruments by the iSTRESS partners, providing a comparison of the FIB-DIC approach for different groups, using different microscopes and software packages.

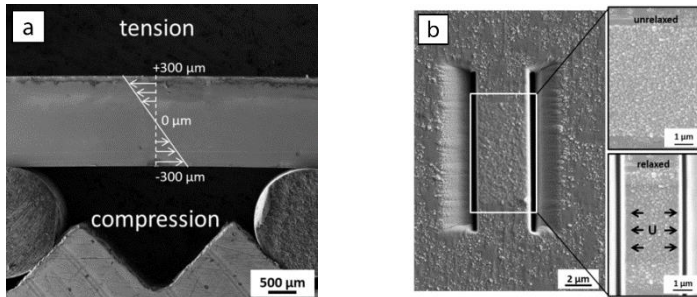


Figure 77. a) Experimental bending setup showing expected stress gradient from tension to compression and b) SEM image of H-Bar milled into CMSX-6 surface in unrelaxed and relaxed state [63].

After the milling process, the exact position of each Double slot milled section on the beam was measured and the corresponding stress level was calculated. The measured stress values are plotted against the expected stress levels from the Euler beam theory in Figure 78. For the nanocrystalline nickel the calculated stress gradient could be measured accurately in both systems on the compression as well as on the tension side of the bent sample. Small deviations from the expected values could be found close to the neutral axis. However, here the stresses are close to the noise level of the FIB-DIC method.

The stress values measured in the CMSX-6 sample also show good agreement with the expected stress gradient in the bent sample. However, an offset between the calculated and measured values is visible as well as a shift of the neutral axis in the Zeiss equipment. The offset in the Zeiss experiment is probably a result of plastic deformation as further investigations showed an indication of a small angle grain boundary.

The results of the experiments compared to the calculated stress values for both samples are also shown in Figure 78. For both samples, the bending stress gradient could be measured accurately, despite an offset in the gradient for the CMSX-6 sample in one of the tests, which can be explained by plastic deformation during sample preparation or the bending process.

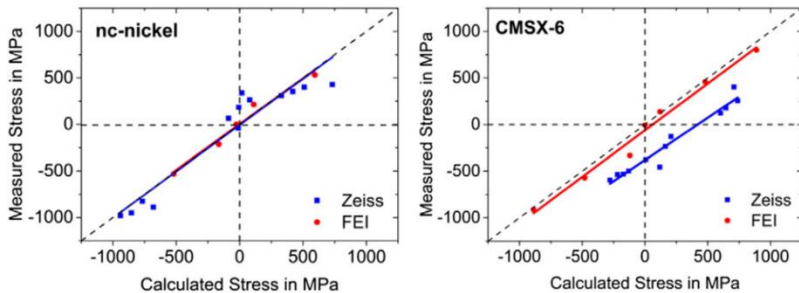
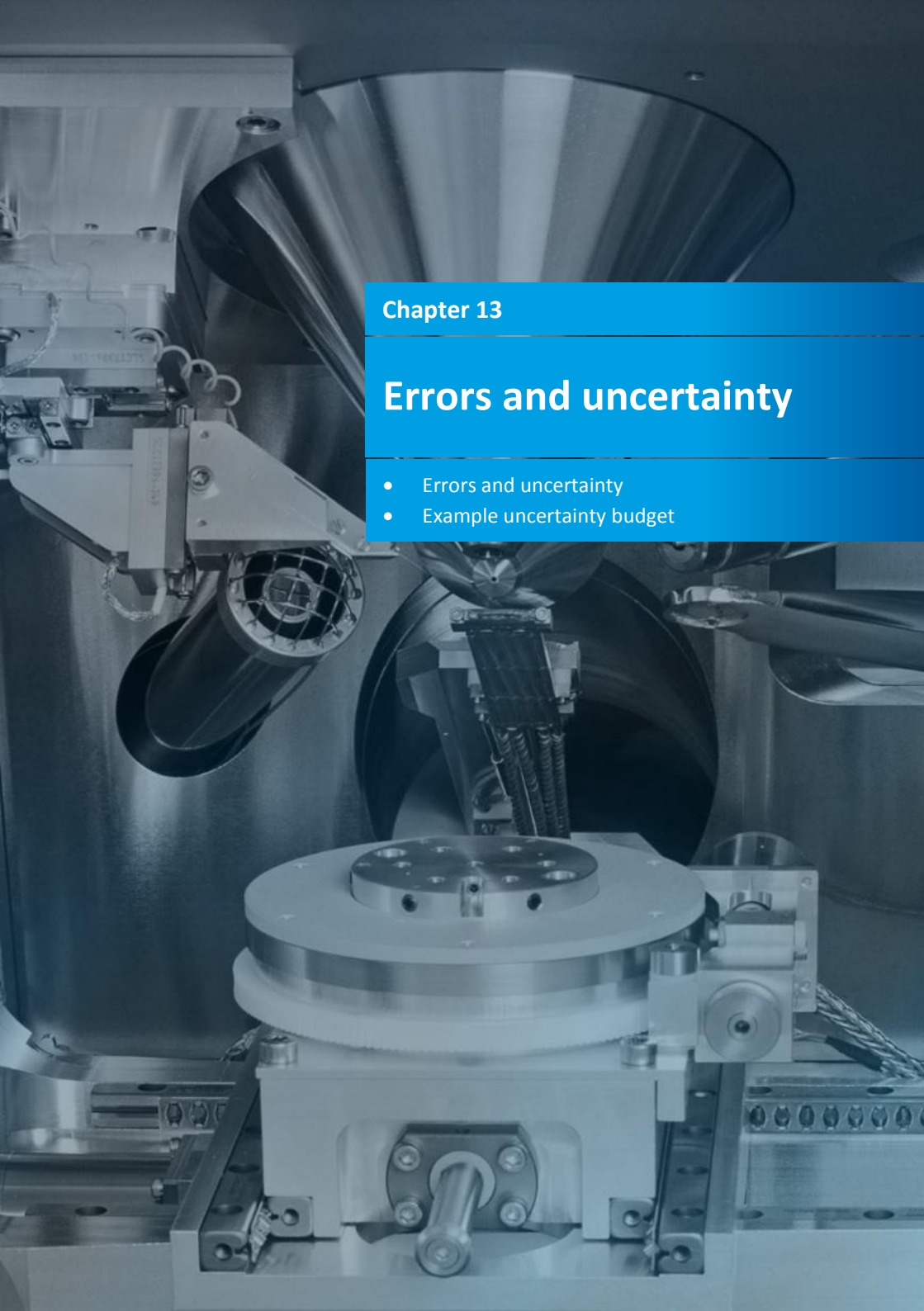


Figure 78. Measured stresses by FIB-DIC in-situ loading tests for 2 FIB systems on the nanocrystalline nickel and CMSX-6 samples under bending, compared to the calculated stress gradient from bending theory [63].

This page was intentionally left blank.



Chapter 13

Errors and uncertainty

- Errors and uncertainty
- Example uncertainty budget

Errors and uncertainty

It is good practice in any measurement to estimate the uncertainty associated with the measured value, but this is not always carried out and rarely reported, particularly in the materials testing community. It is, however, a valuable activity that can help to identify which experimental factors or aspects of the test are likely to contribute most to the uncertainty and errors in the measurement and can also be used to benchmark measurements made with different setups or at different laboratories.

At all stages of the measurement and the analysis of the data there exists potential sources of error, but it is important to distinguish the term “error” from the term “uncertainty”.

Error is the measured value minus the true value of the quantity being measured.

Uncertainty is the amount of doubt in the measured value and is usually described by a parameter that defines the interval within which the value of the quantity being measured (the residual stress in this case) is expected to fall with a stated confidence.

Several documents are available to help develop an understanding of uncertainty, providing guidance and advice. The key document is the ISO TAG4 guide, the “Guide to the Expression of Uncertainty in Measurement”, or “GUM” [100], but this can be a little overcomplicated so the reader is advised to look at some of the other publications available [101-104]. In all the documents, the basic procedure for estimating uncertainty can be broken down into the following steps:

1. Identifying the parameters for which the uncertainty is to be estimated
2. Identifying all sources of uncertainty in the test
3. Classifying the type of uncertainty, *Type A* or *Type B*
4. Estimating the sensitivity coefficient c_i and standard uncertainty for each major source
5. Computing the combined standard uncertainty
6. Computing the expanded uncertainty
7. Reporting of results

The key issue is to identify the major factors that contribute to the uncertainty in the measured value. Many of the factors associated with the errors and uncertainties at the different stages of the FIB-DIC process have been covered in previous sections, and can be grouped, and are associated with:

- Sample preparation, surface patterning (Chapters 4, 5)
- The FIB-SEM instrument and imaging (Chapters 3, 8)
- FIB milling (Chapters 6, 7)
- DIC analysis (Chapter 9)
- Calculation of residual stress from the surface strain relief (Chapters 10, 11)

The next step is to identify which are most important, and develop an approach for quantifying them through the development of an uncertainty budget. Table 5 lists some of the important factors affecting the FIB-DIC residual stress measurement procedure. An assessment of their likely contribution to the uncertainty in the residual stress measurement is also included.

It is important to note that this list is not exhaustive and the user is encouraged to consider their own experimental set up, application and data analysis procedures and update the list accordingly.

Source of Uncertainty	Likely contribution *	Comments
Test sample		
Material properties E, v etc.	1	Need accurate values, particularly modulus
Isotropy	2	May be important in some cases
Surface condition (texture, roughness, flatness, oxidation etc.)	2	Can affect the early stages of milling
Sample geometry		Will it fit in the FIB chamber? If tilted?
FIB-SEM Instrument		
Stability and drift		Can be an issue for some systems, but can usually be compensated for in the DIC calculations
User expertise	1	Very important, but difficult to quantify
Image quality and noise	1	Probably the most important factor
SEM Imaging artefacts	2	Can be an issue for some systems, but are generally only a minor contribution
Image resolution		High resolution can cause problems; a resolution 1024 x 800 (or equivalent) is sufficient
Milling		
Choice of milling geometry		Will depend on the stress state in the sample, and on system capability
Accuracy of milling geometry	2	Minor if it doesn't affect the gauge volume and DIC displacement field
Changes of geometry during milling		Not too critical, provided gauge volume is not significantly affected
Accuracy of milling depth	2	Important for depth resolved measurements. Full depth is not always reached – particularly with the Ring-core

Redeposition issues		Shouldn't affect the results if the gauge volume is not affected
DIC Analysis		
Identification of "zero" reference images	2	Minor if multiple images are taken at each milling increment
DIC parameters – window size,etc.	1	Will influence the accuracy and resolution of the displacement and strain data
Uniformity of displacement/strain field	1	Assumption in most cases is for uniform displacement or strain fields
Presence of milling/DIC processing artefacts in the gauge volume	2	Should be minimised by suitable choice of milling and DIC parameters Avoid data from close to edges
Strain calculations	2	May be affected by area over which it is calculated and DIC analysis Assumption of uniform strain may not be true
Incomplete strain relief	1	Extrapolation will be required to predict full extent of strain relief
Pre- and post- processing of images and DIC data	2	Multiple images are recommended to reduce noise
Calculation of Residual Stress		
Fitting to strain relief profile	2	Important to identify full strain relief
Accuracy of FE modelling	1	Will affect the validation of the experimental data and the calculation of residual stress
Anisotropy effects	2	Knowledge of grain orientation is required for highly anisotropic materials

Key *: 1 = Major contribution, 2 = minor contribution, blank = negligible contribution

Table 5. Potential sources of uncertainty in the FIB-DIC residual stress measurement.

Once the major sources of uncertainty have been identified they must be classified according to type (A or B), and an estimate made of their contribution to the overall uncertainty of the parameter being investigated. This may involve sensitivity analyses or a direct calculation of their contribution.

Type A uncertainties are associated with a series of observations and evaluated using statistical methods associated with the analysis of variance; Type B uncertainties are those associated with data calculated by any other means – such as previous measurements, manufacturer's specifications, datasheets, standard procedures, journal articles, conference

papers and other available information. In most cases for Type B uncertainties, a rectangular distribution will be assigned to the uncertainty component using a $\sqrt{3}$ divisor to convert the quantities to a standard uncertainty.

The combined standard uncertainty is then calculated by the root sum squares approach, from which an expanded uncertainty can be determined. This is obtained by multiplying by a coverage factor, k , which is selected based on the confidence level required. For a normal probability distribution, a coverage factor, $k = 2$, corresponds to a confidence interval of 95 %.
The result should then be reported as the measured value \pm expanded uncertainty.

The sources of the uncertainty are not necessarily independent and unrecognised systematic effects may still exist that cannot be taken into account but contribute to errors in the measurement. For this reason, the use of reference materials or tests, participation in inter-laboratory studies or comparative measurements using other techniques are recommended. Assessments based on repeat measurements are also useful, but are not so easy with the FIB-DIC approach due to the time and cost of each milling measurement, and a single experiment generally provides only one result. **Extra care should therefore be taken to ensure that the measurements are of the highest quality and accuracy.**

Example uncertainty budget

Table 6 shows an example uncertainty budget that has been developed for one of the iSTRESS tests, based on some of the major contributions identified in Table 5 above. The test was used for measuring residual stress in a TiN coating using the **Ring-core geometry** and FIB-DIC analysis procedures.

During milling the Ring-core geometry a biaxial stress develops in the central core. For simplicity, consider only the stress in the x -direction, which is given by:

$$\sigma_x = -\frac{E}{(1-\nu^2)} [\Delta\varepsilon_{\infty}^x + \nu\Delta\varepsilon_{\infty}^y] \quad \text{or} \quad \sigma_x = -\frac{E[\varepsilon^x + \nu\varepsilon^y]}{(1-\nu^2)} \quad (16)$$

The sensitivity coefficients are obtained by evaluating the partial derivatives for the values of the various quantities. In this case the corresponding partial derivatives are:

$$\frac{\partial\sigma}{\partial E} = -\frac{(\varepsilon^x + \nu\varepsilon^y)}{(1-\nu^2)}, \quad \frac{\partial\sigma}{\partial\varepsilon^x} = -\frac{E}{(1-\nu^2)} \quad (17)$$

$$\frac{\partial\sigma}{\partial\varepsilon^y} = -\frac{Ev}{(1-\nu^2)} \quad \text{and} \quad \frac{\partial\sigma}{\partial\nu} = -\frac{E(v^2\varepsilon^y + 2\nu\varepsilon^x + \varepsilon^y)}{(1-\nu^2)^2} \quad (18)$$

The relevant material parameters used for the calculation of the residual stress σ_{Rx} and uncertainties are: $E = 485$ GPa, $\nu = 0.2$, and the relief strains from milling to full depth

estimated to be $e^x = 0.0025$ and $e^y = 0.0038$. In Table 6, the standard uncertainties for each source that contribute to the uncertainty in residual stress are calculated from:
 $(\text{Uncertainty}/\text{Divisor}) * C_i$.

For this test three independent contributions associated with the calculation of strain relief have been included covering the uncertainties associated with the selection of DIC parameters, the strain resolution and the fitting to the strain relief profile. Some of the factors contributing to the uncertainties in DIC processing and the strain measurement have been discussed and presented previously in Chapter 9, and the various uncertainty contributions have been estimated from a combination of user experience, observations and many tests. The noise or scatter in the strain has been estimated from the variation in the calculated strains at each depth increment (Figure 36 or Figure 79b below) to be ± 0.0001 . Based on the DIC parameters used, the contribution to uncertainty is estimated to be $\pm 5\%$ of the measured strain value in the x -direction or ± 0.000125 . Finally the fit to the strain relief profile will also contribute, particularly in this case where full strain relief in the y -direction has not been achieved. An estimate of ± 0.0001 is included in the calculation, but more rigorous approach could be used by examining the curve fitting parameters in more detail. The contributions associated with the DIC accuracy and fitting to the strain relief profile are associated with the calculation of e^x and therefore have the same sensitivity coefficient.

Source of Uncertainty	Uncertainty	Measured Value	U (%)	Prob distrib	Divisor	C_i	$U(\sigma_R)$ GPa
Modulus, E	± 40 GPa	485 GPa	8.2	Rect	$\sqrt{3}$	0.0034	0.08
Poisson's ratio, ν	± 0.02	0.2	10.0	Rect	$\sqrt{3}$	2.61	0.03
Strain e^x	± 0.0001	0.0025	4.0	Rect	$\sqrt{3}$	505	0.03
Strain e^y	± 0.0001	0.0038	2.6	Rect	$\sqrt{3}$	101	0.01
DIC accuracy	± 0.000125	0.0025	5.0	Rect	$\sqrt{3}$	505	0.04
Fit to relief strain at full depth	± 0.0001	0.0025	4.0	Rect	$\sqrt{3}$	505	0.03
Combined Standard Uncertainty							0.10
Expanded Uncertainty ($k = 2$, 95 %)							0.20

Table 6. Example Uncertainty budget for FIB-DIC residual stress measurement on a TiN coating using the ring core geometry ($E = 485$ GPa, $\nu = 0.2$, $e^x = 0.0025$ and $e^y = 0.0038$)

According to this analysis the residual stress value should be reported as $\sigma_{Rx} = -1.65 \pm 0.20$ GPa with a confidence level of 95 %.

This uncertainty is probably much greater than expected, as a detailed assessment of the uncertainty is rarely carried out. A significant benefit of developing an uncertainty budget is the identification and realisation of the importance of certain factors. In the above analysis the

potential uncertainty in modulus, cited as 40 GPa, which is an estimate from measurements and handbook value, contributes most to the uncertainty in residual stress, perhaps not surprisingly as the residual stress is calculated directly from the elastic relaxation. If more accurate values for the material properties could be measured this will have a significant influence on the overall uncertainty.

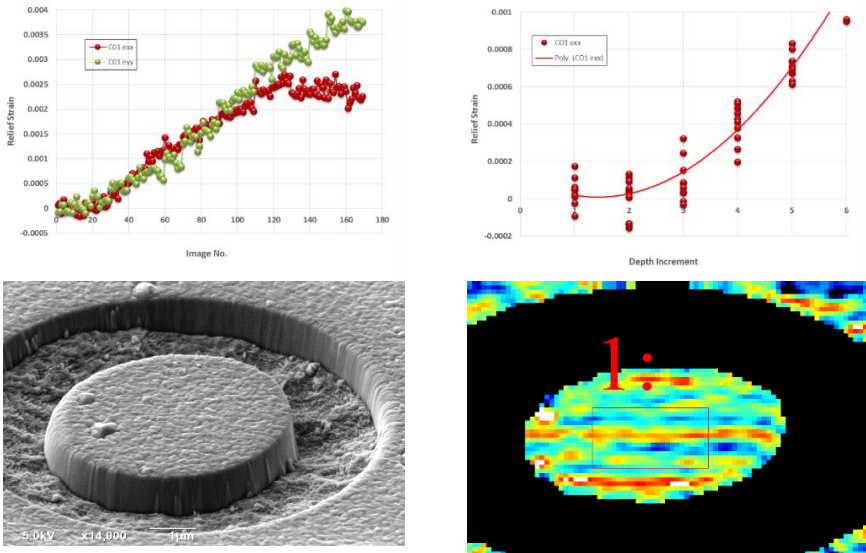


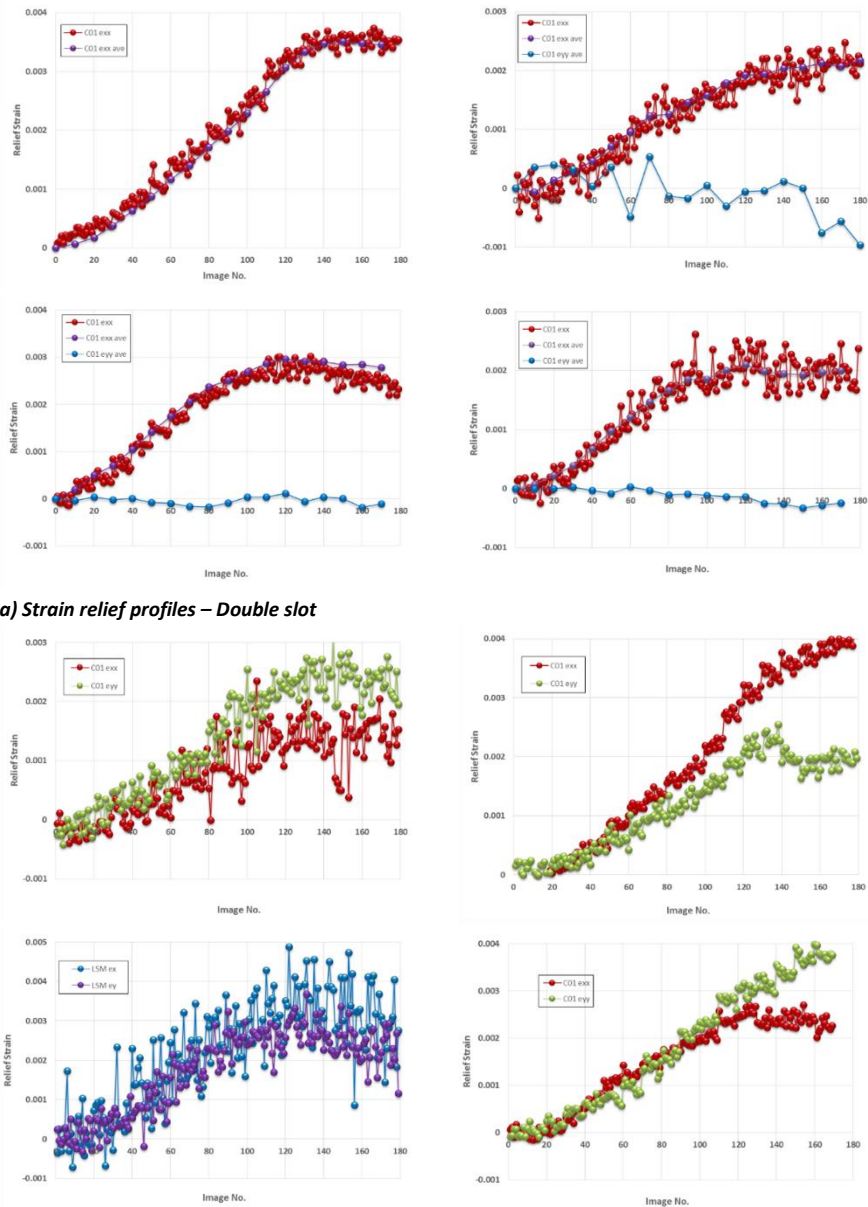
Figure 79. Representative data from Ring-core milling test on a TiN coating.

The uncertainty budget shows that improvements in the accuracy of the strain measurement would significantly reduce the overall uncertainty in the residual stress measurement. Even if the additional contributions associated with the DIC parameters, strain resolution and strain fitting are ignored, there would still be an uncertainty of ± 178 MPa in the result.

Clearly the uncertainty in the measurements will vary due to the quality of the results. Consider now the data in Figure 80, which shows a set of strain relief curves from measurements made by different partners on the same TiN coating in iSTRESS round robin exercise. All partners milled the Ring-core and Double slot geometries and the images were analysed using identical DIC processing conditions in all cases. The large scatter and variation in the calculated strain profiles in some cases is significantly greater than the data used in the calculations above, so these results are likely to have even greater uncertainties in the measured value.

In practice with the Ring-core geometry full strain relief is not always achieved so some extrapolation of the fit to the strain relief profile may be necessary to estimate the plateau strain, inevitably leading to greater uncertainty in this value.

A similar approach can be taken for the other milling geometries.



a) Strain relief profiles – Double slot

b) Strain relief profiles – Ring-core

Figure 80. Representative strain relief profiles from measurements in a TiN coating.

A large industrial machine, likely a vacuum chamber or reactor, with various ports, flanges, and a central vertical tube.

Reporting of results

- Reporting of results

Reporting of results

It is recommended that users develop a standard proforma/file to record the relevant details of the FIB-DIC process. This will provide traceability and can be used to develop and identify optimum reference conditions for further tests on the same material or repeat tests for a customer.

The file could be split into 3 sections to cover the actual milling and images, DIC processing and analysis and reporting of the residual stress value. Representative images should be included. The level of detail is at the discretion of the individual user, but should include at least the following:

Milling and Imaging

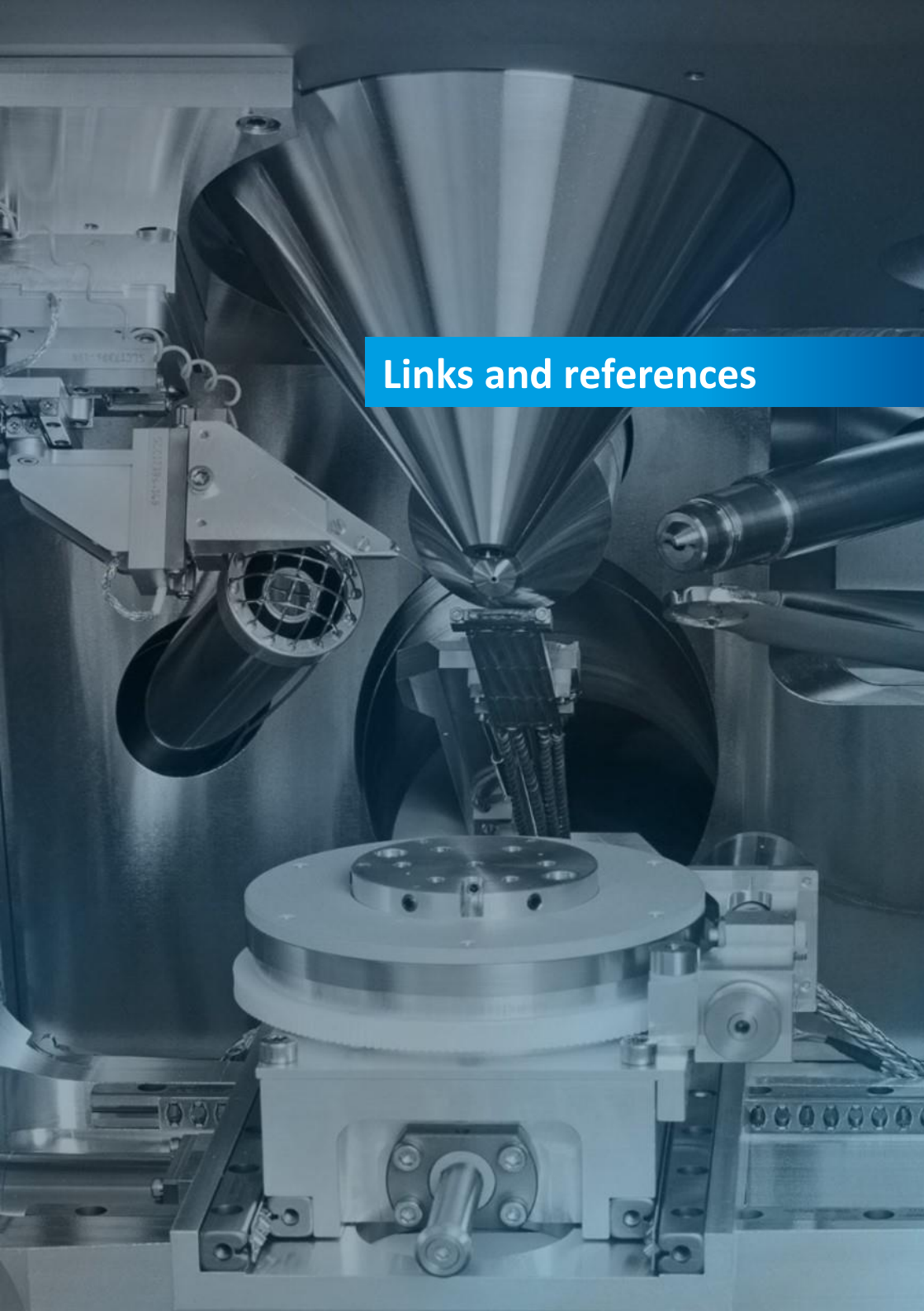
- Machine type, Operator, date of test
- Details of material being tested
- Surface preparation – including details of any external patterning
- Milling geometry
- Milling conditions
- Milling rate and the number of depth increments (and images taken)
- Details of Auto milling scripts used
- Imaging conditions – bit depth, resolution, brightness and contrast etc.
- Tilt correction and drift correction

DIC analysis

- Reference state images and condition
- Details of DIC software used
- DIC processing conditions – window size, thresholding
- Include images – of milled geometry and DIC displacement field, including the area where the displacement and strain was calculated

Residual stress calculations

- Details of the strain calculation – area average, fit to displacement data
- Any pre-processing or post processing of images or data
- Strain relief curve – and details of fit
- Material properties used to convert strain to stress
- Stress calculation
- Results including uncertainty
- Comments as necessary



Links and references

Links and references

Useful websites for FIB manufacturers

TESCAN	http://www.tescan.com/en-us/technology/fib-sem
FEI	https://www.fei.com/products/fib
Zeiss	https://www.zeiss.com/microscopy/int/products/fib-sem-instruments.html
Jeol	http://www.jeolusa.com/PRODUCTS/Scanning-Electron-Microscopes-SEM/SEM-FIB

Useful websites for DIC software and reference images

iSTRESS DIC	http://www.istress.eu
Freeware DIC	http://uk.mathworks.com/matlabcentral/fileexchange/50994-digital-image-correlation-and-tracking
LaVision	http://www.lavision.de/en/products/strainmaster/
Match ID	http://matchidmbc.be/
Correlated Solutions	http://correlatedsolutions.com/
GOM Correlate	http://www.gom.com/3d-software/gom-correlate.html
Fraunhofer VEDDAC	http://www.cwm-chemnitz.de/produkte/software
SEM Challenge	http://sem.org/dic-challenge/

Relevant iSTRESS reports

(Available to download from <http://www.stm.uniroma3.it/iSTRESS/>)

- D2.1 Assessment of Milling Geometries and preliminary FIB-SEM protocols
- D2.2 Delivery of FIB-SEM Protocols
- D2.4 Calibration process for the characteristic SEM optical errors
- D2.6 Stable Matlab routine with a graphical user interface
- D3.2 Completion of RR1 – 1st iteration
- D3.3 Delivery of specimens for RR2
- D3.5 Completion of RR2 – 2nd iteration
- D3.8 Completion of DIC software validation and input to Good Practice Guide

iSTRESS Report Summary

(Available to download from http://cordis.europa.eu/project/rcn/110690_en.html)

References

- 1 Withers, P. J., Bhadeshia, H. K. D. H., Residual stress part 1 – Measurement techniques, Materials Science and Technology, Vol. 17, 2001, pp 355-365, 2013
- 2 Withers, P. J., Bhadeshia, H. K. D. H. Residual stress part 2 - Nature and Origins. Materials Science and Technology, Vol. 17, 2001, pp 366-375, 2013
- 3 Kandil, F.A, Lord J. D. et al., A review of residual stress measurement methods – a guide to technique selection, NPL Report MATC(A)04, 2001
- 4 Lu, J. (Ed), Handbook on residual stress, Society for Experimental Mechanics, ISBN 9780912053912, 2005
- 5 Fitzpatrick, M.E, Fry, A.T., Holdway P. et al., Determination of residual stresses by X-ray diffraction, NPL Measurement Good Practice Guide no. 52, 2005
- 6 Grant, P.V., Lord, J.D., Whitehead, P. S., The measurement of residual stresses by the incremental hole drilling technique, NPL Measurement Good Practice Guide no. 53, 2006
- 7 Buttle, D. J., Moorthy, V., Shaw, B., Lord, J. D. (Ed), Determination of residual stresses by magnetic methods. NPL Measurement Good Practice Guide no. 88, 2006
- 8 Kang, K.J., Yao, N., He, M.Y., Evans, A.G., A method for in situ measurement of the residual stress in thin films by using the focused ion beam, Thin Solid Films, 443 (1-2), pp 71-77, 2003
- 9 Sabaté, N., Vogel, D., Gollhardt, A., Keller, J., Cané, C., Gràcia, I., Morante, J.R., Michel, B., Measurement of residual stress by slot milling with focused ion-beam equipment, Journal of Micromechanics and Microengineering, 16 (2), pp 254-259, 2006
- 10 Kang, K.-J., Darzens, S., Choi, G.-S., Effect of geometry and materials on residual stress measurement in thin films by using the focused ion beam, Journal of Engineering Materials and Technology, Transactions of the ASME, 126 (4), pp 457-464, 2004
- 11 Korsunsky, A.M., Sebastiani, M., Bemporad, E., Focused ion beam ring drilling for residual stress evaluation, Materials Letters, 63 (22), pp 1961-1963, 2009
- 12 Massl, S., Keckes, J., Pippan, R., A direct method of determining complex depth profiles of residual stresses in thin films on a nanoscale, Acta Materialia, 55 (14), pp 4835-4844, 2007
- 13 Sabaté, N., Vogel, D., Keller, J., Gollhardt, A., Marcos, J., Gràcia, I., Cané, C., Michel, B., FIB-based technique for stress characterization on thin films for reliability purposes, Microelectronic Engineering, 84 (5-8), pp 1783-1787, 2007

- 14 Sabaté, N., Vogel, D., Gollhardt, A., Keller, J., Cané, C., Gràcia, I., Morante, J.R., Michel, B., Residual stress measurement on a MEMS structure with high-spatial resolution, *Journal of Microelectromechanical Systems*, 16 (2), pp 365-372, 2007
- 15 Sabaté, N., Vogel, D., Gollhardt, A., Keller, J., Michel, B., Cané, C., Gràcia, I., Morante, J.R., Measurement of residual stresses in micromachined structures in a microregion, *Applied Physics Letters*, 88 (7), art. no. 071910, 2006
- 16 Korsunsky, A.M., Sebastiani, M., Bemporad, E., Residual stress evaluation at the micrometer scale: Analysis of thin coatings by FIB milling and digital image correlation, *Surface and Coatings Technology*, 205 (7), pp 2393-2403, 2010
- 17 Winiarski, B., Langford, R.M., Tian, J., Yokoyama, Y., Liaw, P.K., Withers, P.J., Mapping residual stress distributions at the micron scale in amorphous materials, *Metallurgical and Materials Transactions A: Physical Metallurgy and Materials Science*, 41 (7), pp 1743-1751, 2010
- 18 Massl, S., Keckes, J., Pippan, R., A new cantilever technique reveals spatial distributions of residual stresses in near-surface structures, *Scripta Materialia*, 59 (5), pp 503-506, 2008
- 19 Sebastiani, M., Eberl, C., Bemporad, E., Pharr, G.M., Depth-resolved residual stress analysis of thin coatings by a new FIB-DIC method, *Materials Science and Engineering A*, 528 (27), pp 7901-7908, 2011
- 20 Sebastiani, M., Bemporad, E., Carassiti, F., Schwarzer, N., Residual stress measurement at the micrometer scale: Focused ion beam (FIB) milling and nanoindentation testing, *Philosophical Magazine*, 91 (7-9), pp 1121-1136, 2011
- 21 Sebastiani, M., Bemporad, E., Melone, G., Rizzi, L., Korsunsky, A.M., A new methodology for in-situ residual stress measurement in MEMS structures, *AIP Conference Proceedings*, 1300, pp. 120-126, 2010
- 22 Korsunsky, A.M., Bemporad, E., Sebastiani, M., Hofmann, F., Dave, S., On the measurement and interpretation of residual stress at the micro-scale, *International Journal of Modern Physics B*, 24 (1-2), pp 1-9, 2010
- 23 Keller, J., Gollhard, A., Vogel, D., Auerswald, E., Sabate, N., Auersperg, J., Michel, B., FibDAC - residual stress determination by combination of focused ion beam technique and digital image correlation, *Materials Science Forum*, 524-525, pp 121-126. 102, 2006
- 24 Sebastiani, M., Bolelli, G., Lusvarghi, L., Bandyopadhyay, P.P., Bemporad, E., High resolution residual stress measurement on amorphous and crystalline plasma-sprayed single-splats, *Surface and Coatings Technology*, 206 (23), pp 4872-4880, 2012
- 25 Winiarski, B., Withers, P.J., Micron-Scale Residual Stress Measurement by Micro-Hole Drilling and Digital Image Correlation, *Experimental Mechanics*, 52 (4), pp 417-428, 2012

- 26 Winiarski, B., Gholinia, A., Tian, J., Yokoyama, Y., Liaw, P.K., Withers, P.J., Submicron-scale depth profiling of residual stress in amorphous materials by incremental focused ion beam slotting (2012) *Acta Materialia*, 60 (5), pp 2337-2349, 2012
- 27 Song, X., Yeap, K.B., Zhu, J., Belnoue, J., Sebastiani, M., Bemporad, E., Zeng, K., Korsunsky, A.M., Residual stress measurement in thin films at sub-micron scale using Focused Ion Beam milling and imaging, *Thin Solid Films*, 520 (6), pp 2073-2076, 2012
- 28 Sebastiani, M., Eberl, C., Bemporad, E., Korsunsky, A. M., Carassiti, F., Focused ion beam four-slot milling for Poisson's ratio and residual stress evaluation at the micron scale, *Surface and Coatings Technology*, 2014
- 29 Vogel, D., Rzepka, S., Michel, B., Gollhardt, A., Local stress measurement on metal lines and dielectrics of BEoL pattern by stress relief technique, *IEEE - 2011 Semiconductor Conference Dresden: Technology, Design, Packaging, Simulation and Test, SCD 2011 - International Conference, Workshop and Table-Top Exhibition, 2011*
- 30 Vogel, D., Michel, B., FibDAC stress relief – a novel stress measurement approach for BEoL structures, *Conf. on Stress-Induced Phenomena, Dresden/Bad Schandau, AIP Conference Proceedings*, vol. 1300, Melville, N.Y., pp 127-132, 2010
- 31 Vogel, D., Gollhardt, A., Michel, B., Localized high-resolution stress measurements on MEMS structures, *InterPACK '09, San Francisco*, 2009
- 32 Vogel D., Gollhardt A., Michel B., Micro- and nanomaterials characterization by image correlation methods, *Sensors and Actuators, A: Physical*, (1-2), pp 165-171, 2002
- 33 Krottenthaler, M., Schmid, C., Schaufler, J., Durst, K., Göken, M., A simple method for residual stress measurements in thin films by means of focused ion beam milling and digital image correlation, *Surface and Coatings Technology*, accepted, 215, pp 247-252, 2013
- 34 Yoneyama, S., Basic principle of digital image correlation for in-plane displacement and strain measurement, *Advanced Composite Materials*, Volume25, Issue 2, 2016
- 35 Cox, D. C., Introduction to Focused Ion Beam Nanometrology, Morgan & Claypool, 2015
- 36 Winiarski, B., Schajer, G. S., Withers, P. J., Surface decoration for improving the accuracy of displacement measurements by digital image correlation, *Experimental Mechanics* 52, pp 793-804, 2012
- 37 Gioacchino, F.Di., Quinta da Fonseca, J., Plastic strain mapping with sub-micron resolution using digital image correlation, *Experimental Mechanics*, 53(2), pp 743-754, 2013
- 38 Luo, Y., Ruff, J., Ray, R. et al., Vapour-assisted remodelling of thin gold films, *Chemistry of Materials*, 13, pp 5014-5023, 2005

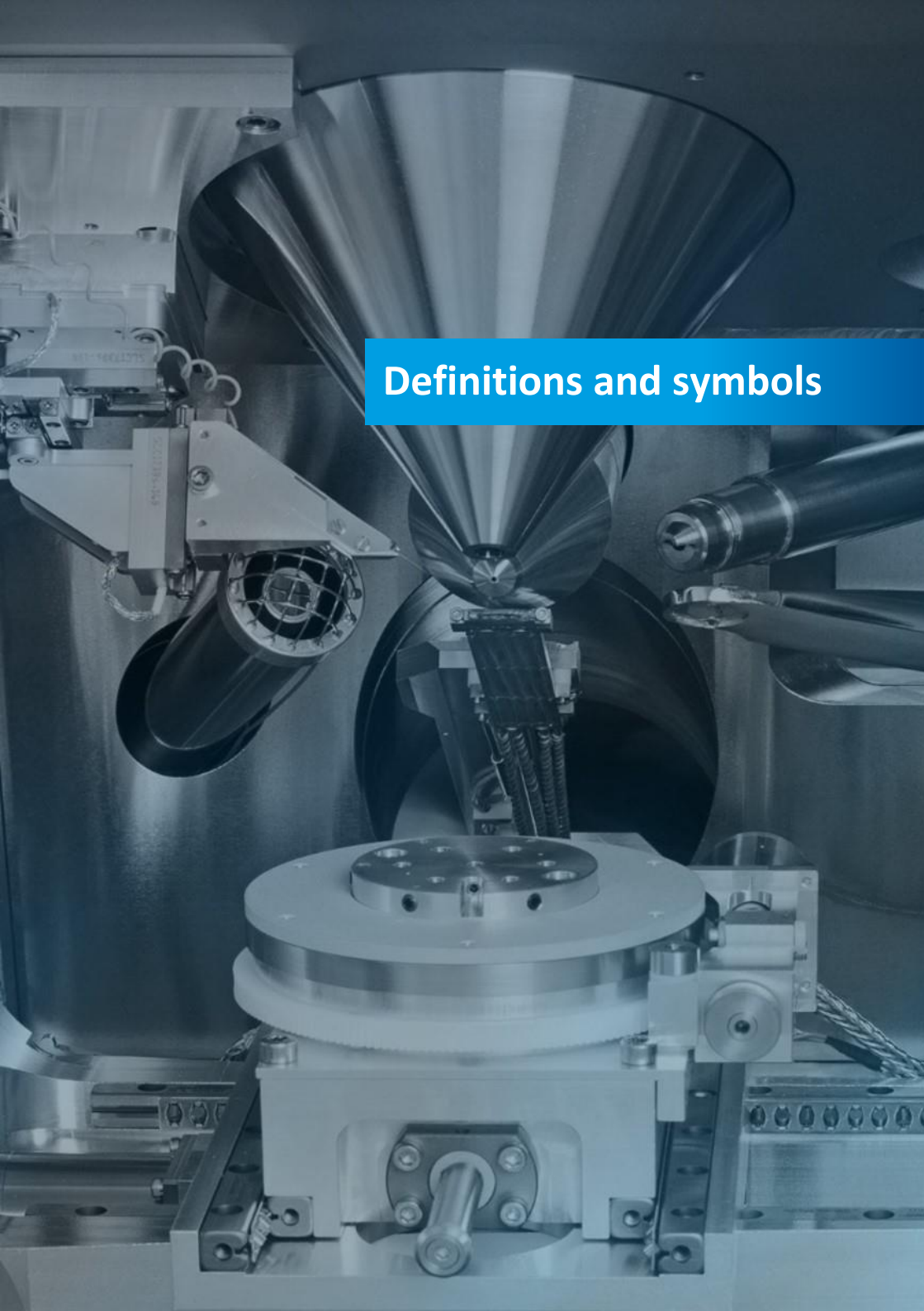
- 39 Scrivens, W. A., Luo, Y., Sutton, M. A. et al., Development of patterns for digital image correlation, Experimental mechanics, 47, pp 63-77, 2007
- 40 Lunt, A. J. G., Baimpas, N., Salvati, E., Dolbyna, I., Sui, T., Ying, S., Zhang, H., Kleppe, A., Dluhos, J., Korsunsky, A. M. , A state-of-the-art review of micron scale spatially resolved residual stress analysis by ring-core milling and other techniques, The Journal of Strain Analysisfor Engineering Design, 2015
- 41 Song, X., Liu, W., Belnoue, J., Dong, J., Wu, G., Ding, W., Kimber, S., Buslaps, T., Lunt, A. J. G., Korsunsky, A. M., An eigenstrain-based finite element model and the evolution of shot peening residual stresses during fatigue of GW103 magnesium alloy, Int J Fatigue, 42, pp 284-295, 2012
- 42 Korsunsky, A. M., Regino, G. M., Nowell, D., Variational eigenstrain analysis of residual stresses in a welded plate, Int J Solids Struct, 44, pp 4574-4591, 2007
- 43 Jameson, E. C., Electrical discharge machining, Society of Manufacturing Engineers, 2001
- 44 Bravman, J.C., Sinclair, R., The preparation of cross-section samples for transmission electron microscopy, J Electron Micro Tech, 1, pp 53-61, 1984
- 45 Grogan, D. F., Zhao, T., Bovard, B. G., Macleod, H. A., Planarizing technique for ion-beam polishing of diamond films, Appl Opt, 31, pp 1483-1487, 1992
- 46 Landolt, D., Fundamental aspects of electropolishing, Electrochim Acta, 32, pp 1-11, 1987
- 47 Glasko, J. M., Elliman, R. G., Zou, J., Cockayne, D. J. H., Fitz Gerald, J. D., Strain and defect microstructure in ion-irradiated GeSi/Si strained layers as a function of annealing temperature. Applied Physics Letters Vol 73, Number 6 ,1998
- 48 Decoster, S., Vantomme, A., Implantation-induced damage in Ge: strain and disorder profiles during defect accumulation and recovery. J. Phys. D: Appl. Phys. 42 165404, pp 10, 2009
- 49 Prime, M. B., Residual stress measurement by successive extension of a slot: the crack compliance method, Appl Mech Rev, 52, pp 75-96, 1999
- 50 Vogel, D., Auersperg, J., Michel, B., Advanced experimental and simulation approaches to meet reliability challenges of new electronics systems: Advanced Engineering Materials, Vol. 11, No. 4, pp 309-1315, 2009
- 51 Vogel, D., Auerswald, E., Rzepka, S., Michel, B., Stress measurement in thin multilayer systems by stress relief, Proc. of microCar , Leipzig, in "Micromaterials and Nanomaterials", Vol. 15, pp 244-247, 2013
- 52 Vogel, D., Ecke, R., Schulz, S., Rzepka, S., Michel, B., Experimental determination of the mechanical stresses in films and structures on Si wafers by fibDAC, Proc. of Smart Systems Integration, Dresden, 2011.

- 53 Mansilla, C., Martínez-Martínez, D., Ocelík, V., De Hosson, J.T.M., On the determination of local residual stress gradients by the slit milling method, *J Mater Sci*, 50, pp 3646-3655, 2015
- 54 Vogel, D., Maus, I., Michel, B., FibDAC stress relief – a novel stress measurement approach with high spatial resolution, Proc. of 3rd Electronics System Integration Technology Conferences ESTC 2010, Berlin, pp 1-5, 2010
- 55 Vogel, D., Auerswald, E., Gadhiya, Gh., Rzepka, S., Fast and trusted intrinsic stress measurement to facilitate improved reliability assessments, *Microelectronics Reliability* 64, pp 276–280, 2016
- 56 Keil, S., Experimental determination of residual stresses with the ring-core method and an on-line measuring system, *Exp Techniques*, 16, pp 17-24, 1992
- 57 Salvati, E., Sui, T., Ying, S., Lunt, A. J. G., Korsunsky, A. M., On the accuracy of residual stress evaluation from focused ion beam DIC (FIB-DIC) ring-core milling experiments, Proc ICNFA'15 265 ,2014
- 58 Bemporad, E., Brisotto, M., Depero, L. E., Gelfi, M., Korsunsky, A. M., Lunt, A. J. G., Sebastiani, M., A critical comparison between XRD and FIB residual stress measurement techniques in thin films, *Thin Solid Films*, 572, pp 224-231, 2014
- 59 Song, X., Yeap, K. B., Zhu, J., Belnoue, J., Sebastiani, M., Bemporad, E., Zeng, K. Y., Korsunsky, A. M., Residual stress measurement in thin films using the semi-destructive ring-core drilling method using Focused Ion Beam, *Procedia Engineering*, 10 , pp 2190-2195, 2011
- 60 Schajer, G. S., Measurement of non-uniform residual stresses using the hole-drilling method. Part I—Stress calculation procedures, *J Engin Mater Technol*, 110, pp 338-343, 1988
- 61 Freund, L. B., Suresh, S., *Thin film materials: stress, defect formation and surface evolution*, Cambridge University Press, pp 750, 2004
- 62 Salvati, E., Sui, T., Korsunsky, A. M., Uncertainty quantification of residual stress evaluation by the FIB-DIC ring-core method due to elastic anisotropy effects. *International Journal of Solids and Structures*, Volume 87, pp 61-69, 2016
- 63 Krottenthaler, M., Benker, L., Mughal, M. Z., Sebastiani, M., Durst, K., Göken, M., Effect of elastic anisotropy on strain relief and residual stress determination in cubic systems by FIB-DIC experiments *Material and Design*, Volume 112, pp 505-511, 2016
- 64 Sutton, M. A., Li, N., et al., Scanning electron microscopy for quantitative small and large deformation measurements. Part I: SEM imaging at magnifications from 200 to 10,000. *Experimental Mechanics* Vol 47, Issue 6, pp 775-787, 2007
- 65 Sutton, A. M., Li, N., et al. Scanning electron microscopy for quantitative small and large deformation measurements Part II: Experimental validation for magnifications from 200 to 10,000. *Experimental Mechanics*, Vol 47, Issue 6, pp 789-804, 2007

- 66 Mansilla, C., Ocelik, V., De Hosson, J. T. M., A New Methodology to Analyse Instabilities in SEM Imaging. *Microsc. Microanal.*, pp 1-13, 2014
- 67 Sutton, M. A., Wolters, W. J., Determination of displacement using an improved digital image correlation method, *Image Vision Computing* 1 (3) , pp 133-139, 1983
- 68 Chu, T. C., Ranson, W. F., Sutton, M. A., Peters, W. H., Applications of digital image correlation techniques to experimental mechanics, *Exp Mech* 25 (3), pp 232-244, 1985
- 69 Sutton, M. A., Orteu, J-J., Schreier, H. W., *Image correlation for shape, motion and deformation measurements. Basic concepts, theory and applications.* Springer. ISBN: 978-0-387-78746-6, 2009
- 70 Bing, P., Hui-min, X., Bo-qin, X., Fu-long, D., Performance of sub-pixel registration algorithms in digital image correlation, *Meas. Sci. Technol.* 17(6), 2006
- 71 <http://sem.org/dic-challenge/>
- 72 LaVision manual
- 73 Lunt, A. J. G., Korsunsky, A. M., A review of micro-scale focused ion beam milling and digital image correlation analysis for residual stress evaluation and error estimation, *Surface and coatings technology*, 283, pp 373-388, 2015
- 74 Sharpe, W. N., Jr, Yuan, B., Edwards, R. L., A new technique for measuring the mechanical properties of thin films, *J Microelectromech Syst.* 6, pp 193-198, 1997
- 75 Read, D. T., Cheng, Y.-W., Keller, R. R., McColskey, J. D., Tensile properties of free-standing aluminum thin films, *Scrip Mater*, 45, pp 583-589, 2001
- 76 Hoffmann, M., Birringer, R., Quantitative measurements of Young's modulus using the miniaturized disk-bend test, *Mater Sci Eng A*, 202, pp 18-25, 1995
- 77 Tomioka, Y., Yuki, N., Bend stiffness of copper and copper alloy foils, *J Mater Process Tech*, 146, pp 228-233, 2004
- 78 Korsunsky, A. M., Constantinescu, A., The influence of indenter bluntness on the apparent contact stiffness of thin coatings, *Thin Solid Films*, 517, pp 4835-4844, 2009
- 79 Korsunsky, A. M., Constantinescu, A., Work of indentation approach to the analysis of hardness and modulus of thin coatings, *Mat Sci Eng a-Struct*, 423, pp 28-35, 2006
- 80 Tricoteaux, A., Duarte, G., Chicot, D., Le Bourhis, E., Bemporad, E., Lesage, J., Depth-sensing indentation modeling for determination of elastic modulus of thin films, *Mech Mater*, 42, pp 166-174, 2010
- 81 Antunes, J. M., Fernandes, J. V., Sakharova, N. A., Oliveira, M. C., Menezes, L. F., On the determination of the Young's modulus of thin films using indentation tests, *Int J Solids and Struct*, 44, pp 8313-8334, 2007

- 82 Jennett, N. M., Aldrich-Smith, G., Maxwell, A. S., Validated measurement of Young's modulus, Poisson ratio, and thickness for thin coatings by combining instrumented nanoindentation and acoustical measurements, *J Mater Res*, 19, pp 143-148, 2004
- 83 Cho, S., Chasiotis, I., Friedmann, T. A., Sullivan, J. P., Young's modulus, Poisson's ratio and failure properties of tetrahedral amorphous diamond-like carbon for MEMS devices, *J Micromech Microeng*, 15, pp 728-735, 2005
- 84 Vlassak, J. J., Nix, W. D., New bulge test technique for the determination of Young's modulus and Poisson's ratio of thin films, *J Mater Res*, 7, pp 3242-3249, 1992
- 85 Kalkman, A. J., Verbruggen, A. H., Janssen, G. C. A. M., High-temperature bulge-test setup for mechanical testing of free-standing thin films, *Rev Sci Instrum*, 74, pp 1383-1385, 2003
- 86 Lunt, A. J. G., Mohanty, G., Ying, S., Dluhoš, J., Sui, T., Neo, T. K., Michler, J., Korsunsky, A. M., A correlative microscopy study of the zirconia - porcelain Interface in dental prostheses: TEM, EDS and Micro-pillar compression, *Surf Coat Tech*, 2015
- 87 Mohanty, G., Wheeler, J. M., Raghavan, R., Wehrs, J., Hasegawa, M., Mischler, S., Philippe, L., Michler, J., Elevated temperature, strain rate jump microcompression of nanocrystalline nickel, *Philos Mag*, pp 1-18, 2014
- 88 Wang, L., Rokhlin, S. I., Recursive asymptotic stiffness matrix method for analysis of surface acoustic wave devices on layered piezoelectric media, *Appl Phys Lett*, 81, pp 4049-4051, 2002
- 89 Flannery, C. M., Murray, C., Streiter, I., Schulz, S. E., Characterization of thin-film aerogel porosity and stiffness with laser-generated surface acoustic waves, *Thin Solid Films*, 388, pp 1-4, 2001
- 90 Shan, X., Xiao, X., Liu, Y., Determination of young's modulus and Poisson's ratio of nanoporous low-k thin film by laser-generated surface acoustic waves, *Adv Sci Lett*, 4, pp 1230-1234, 2011
- 91 Liang, C., Prorok, B. C., Measuring the thin film elastic modulus with a magnetostrictive sensor, *J Micromechanics Microengineering*, 17, pp 709-716, 2007
- 92 Pestka, K. A., Maynard, J. D., Gao, D., Carraro, C., Measurement of the Elastic Constants of a Columnar SiC Thin Film, *Phys Rev Lett*, 100, 055503, 2008
- 93 Chang, J.-Y., Yu, G.-P., Huang, J.-H., Determination of Young's modulus and Poisson's ratio of thin films by combining $\sin 2\psi$ X-ray diffraction and laser curvature methods, *Thin Solid Films*, 517, pp 6759-6766, 2009
- 94 Lunt, A. J. G., Xie, M., Baimpas, N., Zhang, S., Kabra, S., Kelleher, J., Neo, T., Korsunsky, A. M., Calculations of single crystal elastic constants for yttria partially stabilised zirconia from powder diffraction data, *J Appl Phys*, 116, 053509, 2014

- 95 Renault, P. O., Badawi, K. F., Bimbault, I., Goudeau, P., Elkaïm, E., Lauriat, J.P., Poisson's ratio measurement in tungsten thin films combining an x-ray diffractometer with in situ tensile tester, *Appl Phys Lett*, 73, pp 1952-1954, 1998
- 96 Ye, J., Shimizu, S., Sato, S., Kojima, N., Noro, J., Bidirectional thermal expansion measurement for evaluating Poisson's ratio of thin films, *Appl Phys Lett*, 89, 031913, 2006
- 97 Ying, S., Sui, T., Lunt, A. J. G., Reed, R. C., On the cyclic deformation and residual stress in Ni-base single crystal superalloys, *Proceedings of the World Congress on Engineering*, 2 ,2014
- 98 Khyzhun, O. Y., Bekenev, V. L., Parasyuk, O. V., Danylchuk, S.P., Denysyuk, N. M., Fedorchuk, A. O., AlZayed, N., Kityk, I. V., Single crystal growth and the electronic structure of orthorhombic Ti₃PbBr₅: A novel material for non-linear optics, *Opt Mate*, 35, pp 1081-1089, 2013
- 99 Sebastiani, M., Eberl, C., Bemporad, E., Pharr, G. M., Depth- resolved residual analysis of thin coatings by a new FIB-DIC method.
- 100 International Organization for Standardization. TAG 4 Guide to the Expression of Uncertainty in Measurement, Oct 1993.
- 101 Bell, S., A beginner's guide to uncertainty, NPL Measurement Good Practice Guide no. 11, August 1999
- 102 K. Birch. Estimating uncertainties in testing, NPL Measurement Good Practice Guide no. 36, March 2001
- 103 NAMAS M3003. The Expression of uncertainty and confidence in measurement, UKAS, Dec 1997
- 104 F.A. Kandil et al. UNCERT Manual. Manual of Codes of practice for the determination of uncertainties in mechanical tests, National Physical Laboratory, Sept 2000
- 105 <http://www.cwm-chemnitz.de/produkte/software>

A high-end scientific or industrial machine, likely a vacuum chamber or particle accelerator, featuring large cylindrical components and complex mechanical arms.

Definitions and symbols

Definitions and symbols

Term or Symbol	Description or Definition	Units
BMG	Bulk metallic glass	
BSE	Back scattered electron (image)	
CCD	Charge-coupled device	
DAC	Digital to analogue converter	
DIC	Digital image correlation	
DLC	Diamond-like carbon	
EBSD	Electron backscatter diffraction	
EDS	Energy-dispersive X-ray spectroscopy	
FE	Finite element (analysis or modelling)	
FIB	Focused ion beam	
FIB-DIC	Focused ion beam-digital image correlation	
FOV	Field of view	
FWHM	Full Width at Half Maximum	
GIS	Gas injection system	
PGP	Good Practice Guide	
LMIS	Liquid metal ion source	
MEMS	Microelectro-mechanical systems	
NEMS	Nanoelectro-mechanical systems	
NPL	National Physical Laboratory	
PECVD	Plasma-enhanced chemical vapor deposition	
RVE	Representative volume element	
RS	Residual Stress	
SE	Secondary electron (image)	
SEM	Scanning electron microscope	
SI	Secondary ion	
TSV	Through-silicon vias	
ULK	Ultra-low-k	
WDS	Wavelength-dispersive X-ray spectroscopy	
XRD	X-ray diffraction	
YSZ	Yttria Stabilised Zirconium	
C_i	Sensitivity coefficient	
E	Young's or Elastic modulus	GPa
σ	Stress	MPa
ε	Strain (Dimensionless or strain %)	
ν	Poisson's ratio	
u, v	DIC Displacement (in x or y)	Pixels or nm
h	Milling depth	nm or μm
d	Core diameter, trench diameter or distance between two slots	nm or μm
L	Slot/Slots length	nm or μm
t	Thickness of the coating	nm or μm
$B(H, h)$	Kernel function	



Appendix 1

General procedure for FIB-DIC milling

General procedure for FIB-DIC milling

The aim of this procedure is to produce a systematic method that can be carried out by an experienced FIB user, but not one necessarily fully familiar with milling for DIC in the FIB. Assumptions are made that the user is familiar with the FIB instrument, the functions of microscope software and any FIB specific terminology. Also it is assumed the user is aware of the outline methodology of the hole milling process and the specific requirements for the sample being studied.

Section 1: Basic housekeeping

1. Ensure the system is operational and logged on and open any third-party patterning software (such as the NanoPatterning and Visualization Engine, NPVE) if available and check communication with the instrument is functioning correctly.
2. If the sample is unlikely to have sufficient surface texture for the digital image correlation, for example a highly polished surface, or if you are unsure of the surface, ensure the Pt GIS is heated and if not switch on and leave to stabilise for at least an hour, preferably longer.
3. Load the sample in the chamber and ensure the vacuum is in the normal operating range.
4. Turn on the EHT. Use 3 kV typically, and an aperture or spot size at the smaller end of the available range. In some cases there may be advantages by changing these settings, for example higher accelerating voltage may be beneficial for some samples.
5. Turn on FIB source, and set beam current for imaging and milling to the closest value to 100 pA by selecting a suitable aperture and/or condenser voltage. This value is for general guidance only and in slower milling samples and/or larger milled volumes this may need to be increased significantly to enable milling in a reasonable time.
6. Move the sample to a suitable position, but away from the immediate area of interest, to do a dummy hole/milling step.
7. Find sample eucentric tilt height. Once eucentric has been found tilt the sample so that its surface is 90 degrees to the ion beam. These values will vary with different manufacturer, with for example 54° tilt on a Zeiss, 52° for FEI and 55° for Tescan. Raise the sample to the coincident point (\approx 5 mm SEM working distance on most machines, but may be different for your particular instrument).
8. Check alignment of electron and ion beams and correct astigmatism, focus and beam shift. If necessary put ion beam in spot mode for a few seconds and use milled hole to align image centres using beam shifts and check astigmatism of ion beam.
9. Move the sample a short distance from the recently imaged region and using e-beam only check the region is clear from debris and damage and representative of the sample as whole.

Section 2: Establish milling rate for the material

All materials will have their own unique milling rate. If the material you are working with has a known milling rate then this step can be skipped, but good practice dictates the rate should be checked as aperture wear will increase the ion beam current over time.

1. Using the microscope patterning software create a set of 4 holes, separated by at least two hole diameters and ion mill them using close to the following conditions:
 - Diameter if a circle or side length if a square = $2 \mu\text{m}$
 - Beam dwell = $1 \mu\text{s}$
 - Spacing (i.e. beam spot overlap) = 50 %
 - Doses = $1/1.5/2/2.5 \text{nC}/\mu\text{m}^2$ for the four holes respectively
2. Under these conditions each hole should take a few minutes to complete getting progressively longer.
3. Now switch the instrument back to electron imaging mode to establish the four hole depths. Use the SEM to capture a high-resolution image of each and use the measurement tools on the instrument to establish the milled depth of the four holes, ensuring the measurement is tilt corrected.

Several results are possible at this stage:

- The holes have milled well and the measurement is well defined (you may wish to carry out at least two repeats and average the depths). Create a plot and establish the milling rate expressed as nm depth per $\text{nC}/\mu\text{m}^2$ dose. *It should be noted that this milling rate is hole-shape invariant and the rate can be applied to other geometries.*
- The holes are either very shallow (i.e. very low milling rate) or very deep (i.e. very high milling rate). In which case adjust the doses and/or beam current to mill either deeper or shallower and repeat Step 3.
- The material is polycrystalline or multiphase and there is no clear measurement of the depth. This is due to different orientation grains or phases within the hole milling at different rates. In this case establishing an accurate milling rate is almost impossible and the holes should be repeated as many times as is deemed prudent to establish an approximate milling rate.

Section 3: Does the sample need some surface texture?

With a milling rate established it is now possible to mill a series of holes for residual stress measurement. However, in the first instance a decision needs to be made as to whether the sample surface requires additional markers for the DIC analysis. Consider the field of view of the area that the analysis will be carried out over (this is typically a few square μm). Is there sufficient texture for the DIC to track? Or maybe the sample is polished? If in doubt capture a high-resolution image of the sample at the magnification you will use and then move the

sample by a small amount (few % of field of view) in any direction and capture a second image. Process these with the DIC software and see if it can track the displacement from first to second image.

If additional markers are required a simple solution is to create a dot pattern on the sample using the Pt GIS, if available, preferably with the electron beam. Alternative methods are given in the guide, but we have found the following method to be effective for most samples.

1. Tilt the sample back to 0°, ensure the tilt correction is disabled, and ensure the electron beam is in focus and aberration free.
2. Locate the region you wish to pattern and centre it in the field of view and at a suitable magnification.
3. **IT IS VITALLY IMPORTANT THE NEXT STEP IS CARRIED OUT CORRECTLY – TAKE GREAT CARE - INCORRECT APPLICATION WILL RESULT IN DAMAGE TO THE INSTRUMENT.** Check the working distance. With the sample in focus it should be at the beam coincident point. Lower the z-axis on the stage so that working distance is at least **200 µm below the normal height for GIS needle insertion with the sample in focus**. This is to prevent GIS needle damage on insertion as some manufacturers do not recommend GIS needle insertion at 0° tilt with the sample at coincidence. As we will be depositing with electron beam we need the sample at 0° tilt. The implication of this is that there is very little clearance for the GIS needle.
4. Select the Pt GIS and insert the needle.
5. Load the appropriate dot pattern in the instrument patterning software. In many cases this will be a binary bitmap pattern but could be a list of coordinates, known as a deflection list file on some Zeiss systems. For the patterning use a low (3-5) kV for the electron beam along with long beam dwell times of typically 50 ms per point. A ten micrometre square with several thousand points should take no longer than a few minutes to complete.
6. Place the region of interest in the centre of the field of view and change the magnification so that the dot pattern largely fills the field of view. Once aligned stop the scan.
7. If not automatic open the Pt GIS and then run the pattern.
8. On completion close the GIS if not done automatically. At this stage do not image the sample as some Pt gas will still be present.
9. If any further dot patterns are required reduce the magnification before imaging and then move to the next region and repeat the deposition process, but try and avoid long exposures of the sample with the electron beam as some Pt will still be present.
10. Following patterning wait at least 10 minutes, preferably longer, before imaging. We find it most efficient to create several patterns on an afternoon, leave overnight to ensure all gas is cleared and then carry out the hole milling and imaging the next morning. Also If you are planning to deposit more than one pattern, then after every 3rd or 4th you should take a

10-15 minute break to allow the gas to recover as it can become exhausted from continuous running resulting in reduced quality patterns over time.

11. When the gas has dissipated the quality of the pattern can be determined. Firstly remove the GIS needle. For most instances we use a dot pattern with 12000 dots in a 10 µm square. The pattern should be bright, offering significant contrast difference to the substrate with little or no deviation from square. On occasion the pattern may not be sharp, probably due to some sample charge, but it is still unlikely the pattern will be unusable. For samples with non-conductive thin coatings such as silicon nitride films charge effects can be significantly reduced by increasing the accelerating voltage of the electron beam, which also tends to result in smaller individual dots. For highly charging samples it may be that a different approach will be required.

Section 4: FIB milling and image capture

If no dot patterns are required and the sample has sufficient texture, or if dot patterns are now present, proceed as follows:

1. Decide if the processing will be done manually or semi-automatically – on some instruments it is possible to largely automate this process.
2. In all cases the sample should be tilted to normal incidence to the ion beam with the two beams aligned on a sacrificial region of the sample near to where the hole milling will be carried out. It has been found that instabilities in the electron beam scan on many instruments cause significant imaging artefacts if the sample is moved between the image capture and the hole milling process and all should be carried out with the sample tilted normal to the ion beam and without further moves if at all possible.
3. Check focus and astigmatism and adjust the following parameters with typical values shown, but will need some adjustment for different samples. Contrast and brightness in particular will be very sample dependent.
 - SE detector
 - Scan speed = should be 0.5 seconds per frame maximum or can be faster with a higher frame integration number
 - Resolution = 1024 pixels frame width
 - Frame Integration (frame averaging) number = 16 (could be higher if the frame rate is faster but should take less than 10 s for a complete image capture)
 - Mag as required, but the region of interest should be close to filling the sample image
 - Tilt correction ON
 - Specimen current monitor ON if available (we have found better stability with this)

4. Set up a folder where the images will be captured (remember to enable automatic numbering of the images to simplify ease of use with the DIC and keep track of the process).
5. In the instrument patterning software select FIB and then create/load one of the pattern geometries (e.g. Ring-core, Double slot, Single slot).
6. In the dose box enter the dose you require for an individual depth increment. Note: this may be for a single hole to full depth, or an increment for depth profiling of the stress and use the same FIB beam parameters used for the depth calibration.
7. With all of the parameters set a small distance away from the pattern (or area of interest) move the pattern to the centre of field of view and if running manually capture a number of electron beam images with the chosen beam parameters (a minimum of two and maximum of ten is recommended).
8. If running semi-automatically with a live SEM image wait for 30 s to allow everything to stabilise before and then run your macro/script to capture ten images in frame integration mode. You can check in the destination folder in real time and see the images arriving there.
9. Switch to the ion beam and mill the desired geometry.
10. Once milling is complete switch the instrument back to SEM mode and again capture the desired number of images.
11. Providing the beams are well aligned the sample should now appear with a milled hole in the centre of the field of view in the images. If the beams are misaligned and the hole is too far from the centre of the field of view realign the beams on the newly milled hole create a new dot pattern if needed and go back to point 7, remembering to set a new file name if necessary (it is always prudent to do this).
12. If this initial hole has gone satisfactorily then either repeat from point 9 for depth profiling, point 7 for a new region, or move to the next sample if required.
13. Once complete shut down the FIB gun remove the sample. You may want to leave the Pt GIS heated if it will be used again soon.

An example of creation of dot patterns for stress measurement via Hole drilling

Using Matlab a small script was created to generate a random dot pattern over an area of our choice. The script requests that we state an area (always square in shape) and the proximity we allow for nearest neighbour dots. A simple calculation is then performed that gives the maximum number of permissible dots in the area. We then request how many dots should be

created up to this maximum. Once we have specified these, another simple routine in the script creates the required number of dots as random pairs of x , y coordinates, where the 0,0 position corresponds to the centre of the field of view. The routine checks that no dots are too close to each other based on our minimum specified distance and if necessary deletes them and then generates additional coordinate pairs to enable the full number of random dots to be created. A comma delimited text file is also created containing the pairs of coordinates that can be used as input to a deflection list file when available. If no deflection list option is available on the instrument the dots can be plotted from the text file in any appropriate software with square axes and no axes markers and then converted to a simple binary bitmap image for input as patterning option.

Shown below (Figure 81) is one of the text file outputs plotted as a series of points. This dot pattern corresponds to 5000 random points in a $10 \times 10 \mu\text{m}$ square area with no points closer than 50 nm to their nearest neighbour. By creating the points in this manner it is very simple to check the plotted data to an image of the deposited Pt with quite high accuracy.

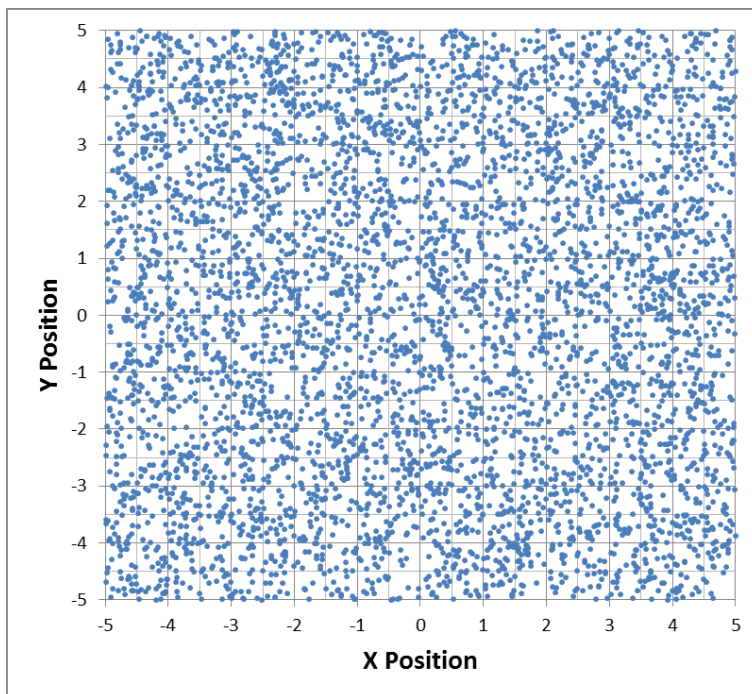


Figure 81. Example of random dot pattern.

This page was intentionally left blank.



Appendix 2

Detailed procedure for determining residual stresses from Single slot milling

Detailed procedure for determining residual stresses from Single slot milling

The approach described here is based on the test protocol developed by one of the iSTRESS partners (Fraunhofer ENAS) using a Zeiss FIB-SEM, proprietary DIC software, FE code and application software, but tests can be made using other FIB systems and DIC software by following the same methodology.

In order to make the stress determination cost and time efficient, as well as reliable, a methodical and automated approach has been developed. This was developed for the single slot measurements with one pre-selected milling depth, and is described in this below.

Figure 82 shows the steps in the process for making stress measurement by the trench approach. The measurements consist of:

- **FIB** based trench milling, including SEM image capture and trench cross sectioning to acquire the trench profile and depth
- **DIC** analysis to obtain the displacement fields on both sides of the trench (in Figure 82, by the commercial software VEDDAC)
- **FE** analysis to provide the expected relaxation field, which is then matched to the DIC field (in Figure 82 using the in-house software code *fibDAC stress relief* [105])

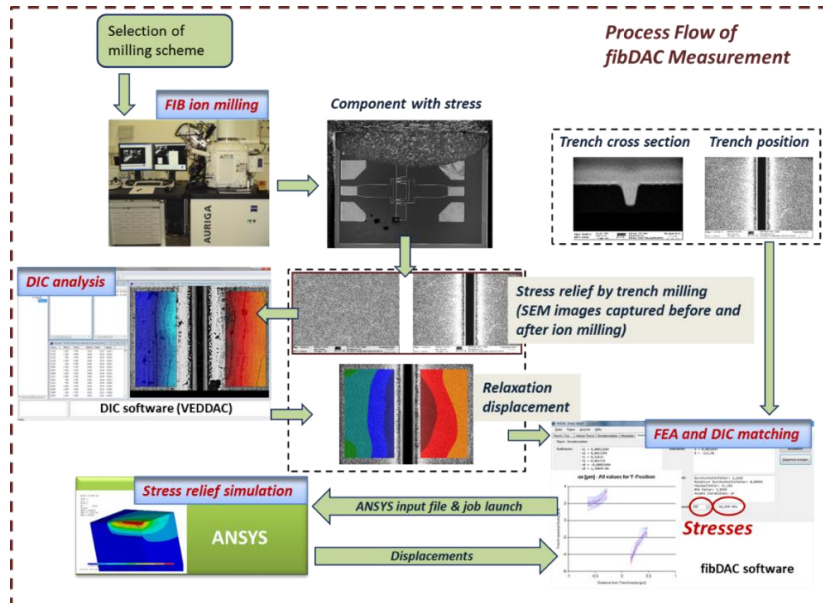


Figure 82. Schematic of the fibDAC trench milling approach.

FIB procedures

The FIB process described below has been developed for a ZEISS AURIGA60 FIB-SEM, but a similar approach could be taken for other FIB systems. The process flow is characterised by the following steps:

- Carry out pre-processing operations including compucentric tilt alignment for the FIB/SEM columns, sample surface preparation to provide appropriate DIC pattern (see also Chapter 5 of this GPG), and selection of the milling position and milling depth t (measured stress σ_{xx} is an average value over t). The SEM column is adjusted normal to the sample surface
- Capture the SEM reference image before ion milling (including at least two repeat images) with the parameters Frame Average 1, Scan Speed 8, Capture Time 10 sec.
- Ion milling of trench with the parameters Aspect Ratio $t/w \approx 1$ (trench depth t to width w), Trench Length $L = 20w$, $w > 80$ pixel. If the whole layer depth is to be sampled, t is selected as 90 % of the layer thickness. The FIB column is kept adjusted 54° or 0° to the sample surface
- Capture the SEM image after ion milling with the same parameters used above.
- Sectioning of the trench in its middle position to capture the trench profile image and measure the trench geometry. If necessary Pt deposition on top to enhance contrast of the profile image

Examples of the supplied three image types (sample image before and after ion milling, trench profile) are shown Figure 83.

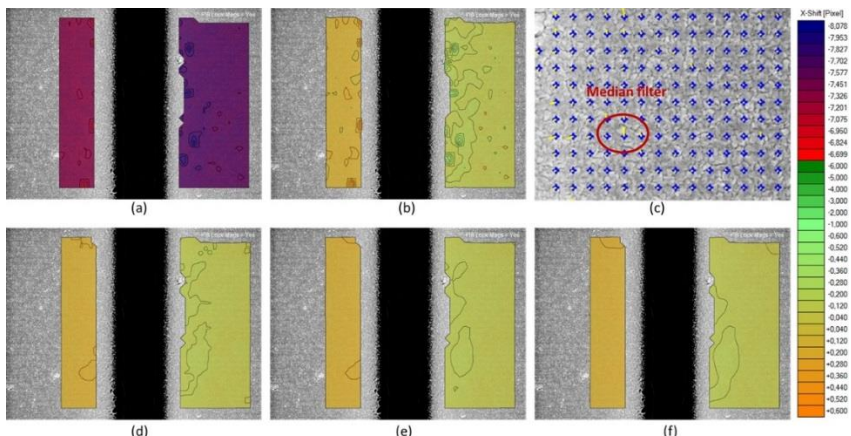


Figure 83. DIC analysis. u_x - horizontal displacement field in the middle of a trench. (a) field as derived from images captured before and after ion milling, (b) field after compensation of rigid body drift, (c) vector field presentation of (b) with outlier vectors, (d) field in (b,c) after median filter for removing outlier values, (e) field in (d) after Gaussian smoothing, (f) final field as in (e) after compensation of rigid body rotation.

DIC analysis

DIC analysis of the example has been performed with the commercially available VEDDAC software [105], but other DIC software can be used. The SEM images are imported into the software and processed using the following steps:

- Marking of rectangular areas to the left and right of the trench for displacement calculation within an equidistant point grid. For the left hand side, the first 200 pixels in a 1024x768 image are not used to avoid artefacts from image distortions due to the image build-up process (see also Chapter 8), which seem quite prevalent ZEISS machines. The areas very close to the trench rim are also skipped, if they exhibit severe pattern de-correlation, which also appear as outlier displacement vectors.
- Selection of an optimised local pattern size tracking window for the DIC, which for most cases range between 40 x 40 to 60 x 60 pixels. These pixel areas must contain unique and distinguishable patterns, but should be kept as small as possible to reduce smoothing of the displacement gradient.
- Automated image DIC processing to compute displacement vector fields.
- Refinement of the derived vector field (see Figure 83), including compensations for rigid body translations and rotations due to FIB drifts between image captures, the removal of outlier vectors by median filtering and smoothing of the data field (as discussed in Chapter 9).

The VEDDAC DIC procedures are based on wavelet algorithms with a low susceptibility to outlier values of displacement vectors, and the sub-pixel algorithm has been proven to generate minimal systematic sub-pixel errors. The standard output files of displacement vectors obtained from the processing can be used for further stress evaluation without any additional conversion procedures.

Finite element analysis to simulate the stress relief process

The stress relief process is presumed linear elastic, which in most of cases is valid. For standard procedures the relevant relief volume is considered to show lateral and in-depth homogeneous normal stress components, in-plane to the sample surface and directed along the applied Cartesian coordinate system. Numerical simulations are carried out under ANSYS FE code. A fixed, parameterised FE input model is used, which allows the definition of an optional number of surface layers with a substrate beneath. Residual bi-axial normal stresses of each separate layer can be user-defined, and all the relevant geometrical, elastic material and pre-defined stress data is given by a separate data input file. This data file is generated from the graphical user interface (GUI) of the *fibDAC Stress Relief* software, which also executes the stress extraction from the DIC and finite element analysis (FEA) displacement fields. This approach takes advantage of fast and simple interactive actions to define necessary dimensional properties.

The *fibDAC Stress Relief* software needs as prerequisite:

- The SEM image captured after trench milling for DIC analysis
- A cross section SEM image showing the trench profile
- An SEM image showing the milled slot from top
- A standard file with the final DIC displacement field in pixel units and coordinates
- If needed for thickness determination, separately an SEM image with the sample layer stack

In order to prepare and export the above mentioned data input file for the FEA, the sample and trench dimensions are edited by marking the respective features on the SEM images, using the pixel scaling from the SEM image headers. Material data or geometrical data without background images (e.g. for lateral sample dimensions and substrate thickness) can be written directly into the default input masks. Figure 84 shows the interface and input parameters before the FEA job is launched.

Once the ANSYS input files have been generated, a 2D or 3D simulation of the stress release process due to slot milling can be started directly from the *fibDAC Stress Relief* software.

Experience shows that a 2D model simulation is sufficient, if a minor imprecision of less than 3 % for extracted stress values is acceptable. The relief displacement fields on both sides of the trench can be computed by ANSYS within a few seconds on a standard notebook, and a datafile of the exported results read by *fibDAC Stress Relief* and compared with the DIC displacement data.

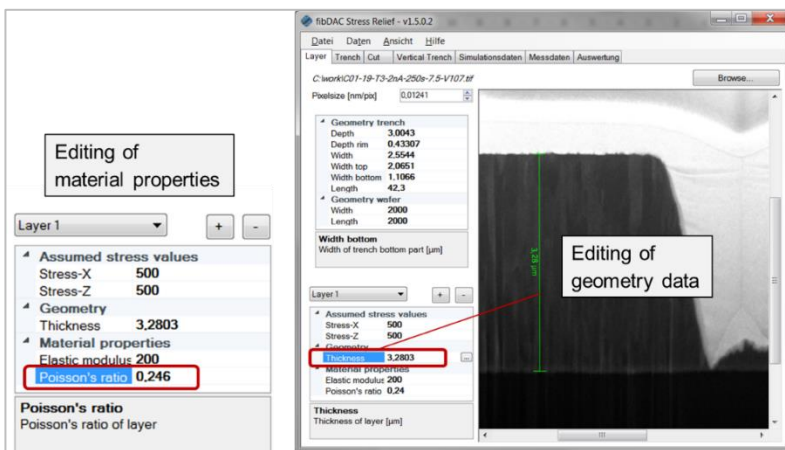


Figure 84. GUI of the *fibDAC* software editing mode. All relevant geometry and material property data can be easily edited and exported as ANSYS data file. Geometrical dimensions are measured by examination of the SEM images.

Stress computation by matching DIC and FEA displacement fields

The trench geometry used for the standard stress measurements have an aspect ratio (length: width) of ≥ 20 at the sample surface. At the magnifications used the field of view in the SEM image only covers 10-40 % of the trench length, but the slot opening/closing displacements (perpendicular to the trench line) are relatively uniform and depend only slightly on the position along the trench. Comparison of the DIC displacements is carried out against simulation data at the centre of the trench (see Figure 85). The inclusion of DIC data sidelong of the trench middle is indicated, because of the better averaging statistics for DIC data, i.e. the better suppression of random errors. Figure 85 gives a typical example of DIC vs. FEA data fitting.

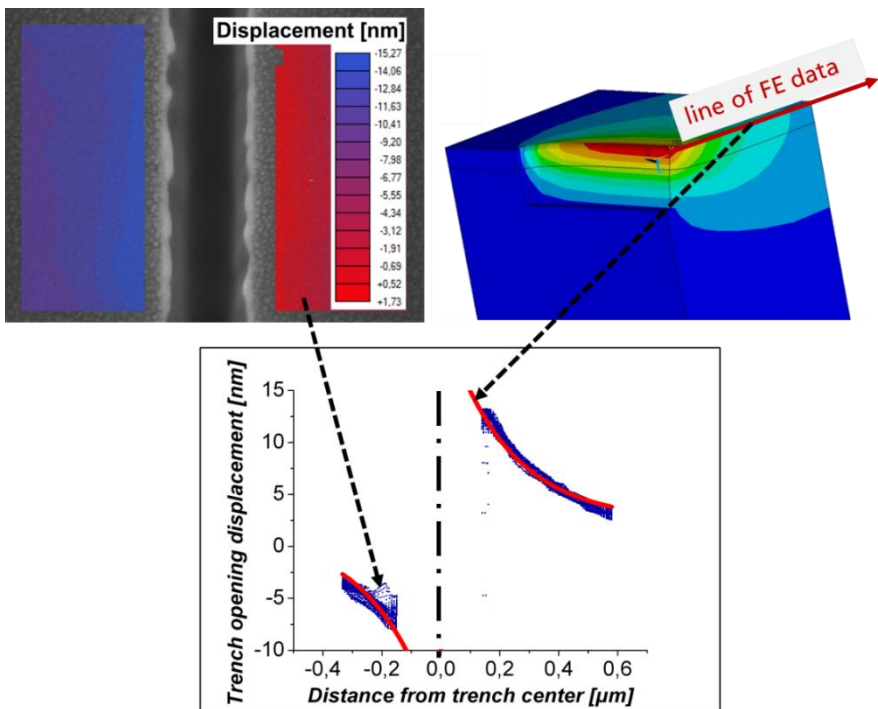


Figure 85. Best fit between DIC (upper left field) and FEA (upper right plot) relief displacements. FEA data is taken along a perpendicular line in the middle of the trench. DIC data originates from the middle area of the trench without distinction on vertical coordinate.

Matching of the DIC and FEA displacement fields are accomplished in the *fibDAC Stress Relief* software. The software needs as prerequisite for this procedure:

- The SEM image captured after trench milling for DIC analysis
- A standard file with the final DIC displacement field on both sides of the trench in pixel units and coordinates
- A standard file with the simulated displacement field in the middle of the trench along a line perpendicular to the trench direction for an arbitrarily chosen stress, in SI units

Matching of the DIC and FEA displacement fields also requires a conformity of the coordinate systems used for FEA and DIC analyses. For the FEA a coordinate system centred in the trench middle with coordinate axes along and perpendicular to the trench line is used. The size and position of the coordinate system in the DIC analysis can be identified with the help of interactive trench marking in the *fibDAC stress relief* software (see Figure 86).

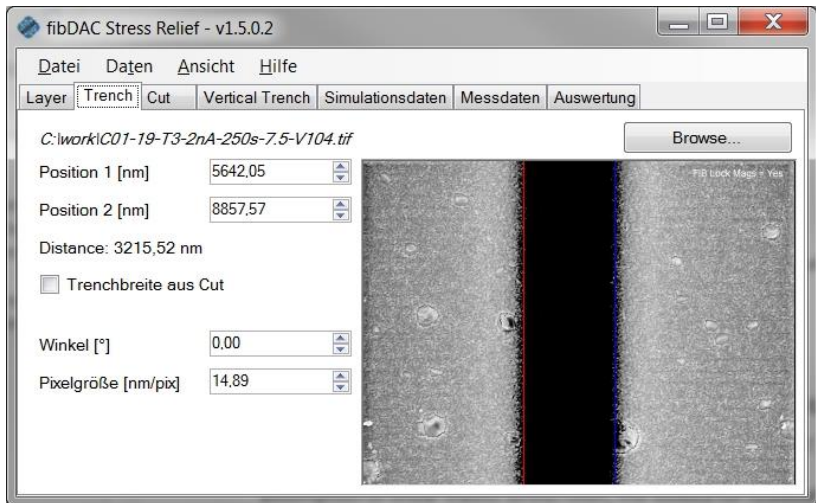


Figure 86. Determination of trench position and orientation in the DIC analysis.

Matching is achieved by scaling the FEA displacement field u_x^{FEA} for the arbitrarily chosen stress σ_{xx}^{FEA} until the best match to the DIC displacement data u_x^{DIC} is reached. Because of the assumption of linear elastic stress relief, the residual stress $\sigma_{xx}^{residual}$ and DIC displacement u_x^{DIC} (both components perpendicular to the trench line) scale with the same factor B , i.e.

$$\sigma_{xx}^{residual} = B \sigma_{xx}^{FEA} \quad (19)$$

$$u_x^{DIC} = B u_x^{FEA} + A \quad (20)$$

The variable A describes the rigid body displacement between the analysed SEM images due to the SEM stage drift. It is part of the unknown parameter set fitted in the matching procedure.

In order to reduce artefacts caused by SEM stage drifts, the SEM line scan direction has to be chosen along the x axis, so that the trench opening/closing manifested by u_x along x is less influenced by stage drifts over time. Using longer times for capturing the image should be avoided as it can lead to artificially induced image shear or strain in the image z direction. Image shear appears as higher spread of the DIC data cloud, but results in nearly the same average amount of trench opening/closing, i.e. the same stress determined from it.

A preliminary estimate of the accuracy of the stress measurement for the Single slot gives a value of ± 40 MPa for a material with a Young's modulus of 190 GPa. This scales in the same way as the Young's modulus of the material being investigated and was derived from in-situ FIB-DIC bending bar experiments with known stress states.

This page was intentionally left blank.

A Good Practice Guide for Measuring Residual Stresses using FIB-DIC

Good Practice Guide No. 143

The aim of this Good Practice Guide (GPG) is to provide recommended procedures for measuring residual stresses using the FIB-DIC technique. It is designed to be a practical guide, with advice, tips and supporting information to illustrate the various process steps and data analysis required to make reliable and repeatable high resolution residual stress measurements using the FIB-DIC approach. With this method, standard geometries are milled using the focused ion beam (FIB) and the surface displacements resulting from relaxation captured from the scanning electron microscope (SEM) images using digital image correlation (DIC) software; these are then used in combination with finite element (FE) modelling to calculate the residual stresses in the material. The GPG is a key output from the iSTRESS project, and aims to provide users with a robust methodology and practical advice for making reliable residual stress measurements on their own systems and materials using this technique.



ISSN: 1368–6550

npl.co.uk/guides